TRƯỜNG ĐẠI HỌC QUY NHƠN
QUY NHON UNIVERSITY

TẠP CHÍ KHOA HỌC
TRƯỜNG ĐẠI HỌC QUY NHƠN

QUY NHON UNIVERSITY
JOURNAL OF SCIENCE

KHOA HỌC TỰ NHIÊN VÀ KỸ THUẬT
NATURAL SCIENCES AND ENGINEERING

17 (3)

2023

JUNE 2023

QUY NHON UNIVERSITY
JOURNAL OF SCIENCE
VOLUME 17, ISSUE 3, JUNE 2023
ISSN: 1859-0357 E-ISSN: 2815-6242

CONTENTS

TẠP CHÍ KHOA HỌC
TRƯỜNG ĐẠI HỌC QUY NHƠN

Mô hình số cho tủ điện trong nhà máy điện hạt nhân: tổng quan

Trần Thanh Tuấn[1,*], Nguyễn Phú Cường[2], Dookie Kim[3,*]

[1]Viện năng lượng gió ngoài khơi, Trường Đại học Quốc gia Kunsan, tỉnh Jeollabuk, Hàn Quốc
[2]Nhóm nghiên cứu kỹ thuật kết cấu nâng cao, Bộ môn Công trình, Trường Đại học Mở Thành phố Hồ Chí Minh, Thành phố Hồ Chí Minh, Việt Nam
[3]Khoa Xây dựng và môi trường, Trường Đại học Quốc gia Kongju, Hàn Quốc

Ngày nhận bài: 21/12/2022; Ngày nhận đăng: 21/02/2023; Ngày xuất bản: 28/06/2023

TÓM TẮT

Xây dựng mô hình số cho tủ điện trong nhà máy điện hạt nhân đóng vai trò quan trọng trong việc đánh giá rủi ro động đất. Mô hình phần tử hữu hạn cho phân tích phi tuyến thường tốn nhiều thời gian do sự phức tạp của nó. Trong khi đó, mô hình đơn giản hóa có thể giảm thiểu đáng kể sự phức tạp, tuy nhiên các đặc điểm động lực học (khối lượng, dạng dao động, hay ứng xử phi tuyến) thường không được đánh giá đầy đủ. Bài báo này trình bày tổng quan cách tiếp cận hiện tại trong việc xây dựng mô hình cho các tủ điện. Kết quả nghiên cứu đóng vai trò là tài liệu tham khảo hữu ích cho các nhà nghiên cứu.

Từ khóa: *Tủ điện, nhà máy điện hạt nhân, mô hình đơn giản, mô hình phần tử hữu hạn.*

**Tác giả liên hệ chính.*
Email: tranthanhtuan@kunsan.ac.kr, kim2kie@kongju.ac.kr

https://doi.org/10.52111/qnjs.2023.17301

QUY NHON UNIVERSITY
JOURNAL OF SCIENCE

Finite element modelling of electric cabinets in nuclear power plants: a review

Thanh-Tuan Tran[1,*], Phu-Cuong Nguyen[2], Dookie Kim[3,*]

[1]Institute of Offshore Wind Energy, Kunsan National University, Jeollabuk-do, Republic of Korea
[2]Advanced Structural Engineering Laboratory, Department of Structural Engineering, Ho Chi Minh City Open University, Ho Chi Minh City, Vietnam
[3]Department of Civil and Environmental Engineering, Kongju National University, Republic of Korea

Received: 21/12/2022; Accepted: 21/02/2023; Published: 28/06/2023

ABSTRACT

The development of numerical modeling for safety-related cabinet facilities plays an essential role in seismic risk assessment. For nonlinear time history analysis, a full finite element model is often time-consuming due to its computational complexity. A simplified model can significantly reduce modeling complexity, however, the dynamic characteristics (such as mass, local mode shapes, or nonlinear behavior) are not fully captured. The current paper presents an overview of the current literature addressing the development of cabinet modeling. The results are expected to serve as a general reference and starting point to new researchers.

Keywords: *Cabinet facility, nuclear power plant, simplified model, finite element modeling.*

1. INTRODUCTION

Electric cabinet is one of the essential facilities in nuclear power plants (NPPs). This equipment is sensitive to acceleration due to carrying relays and switches.[1] During an earthquake, the cabinets can be damaged and they can extend the accident to nearby structures triggering an uncontrolled mechanism known as the Domino Effect (see Figure 1).[2] Besides, the cabinet contains many power distribution systems such as electric switchboard, control transformer, or control circuit fuse, and so on, which is quite sensitive to the performance of the cabinet. The damage to the mechanical and electrical equipment in nuclear power plants causes the large social and economic damage. Therefore, the seismic performance of these non-structural components should be considered carefully.[3-11]

Generally, to assess the structural performance of cabinet facilities, the experiment and finite element methods are popularly used.[12-14] However, these approaches are expensive and the result interpretation may be difficult. As shown in Figure 2, the experimental approach is the most time-consuming compared to the analytical one, and when the equipment complexity increases, the analysis time increases.[15] The large portion of experimental works leads to the cost increase. Additionally, it is noted that finite element analysis can produce serious errors due to inexperience on the part of users.[16] Moreover, due to the complexity of the attached electrical devices, it will take a long time for analysis.

**Corresponding author.*
Email: tranthanhtuan@kunsan.ac.kr, kim2kie@kongju.ac.kr

https://doi.org/10.52111/qnjs.2023.17301

Figure 1. Damage of non-structural components.[19]

to overcome the above limitation, there is a need to develop a simplified approach for practical reasons. In 2016, Lim[18] developed a method for generating simplified finite element models for electrical cabinets, which can capture the buckling behavior or failure of connectors of cabinet structure. Various researchers developed numerical models of cabinets that can capture the buckling of steel plates, failure of connectors, and the local buckling effect and nonlinear behavior support boundary conditions.[16-19]

The present paper focuses on surveying the reported numerical modeling for cabinet facilities in the nuclear industry. Firstly, the important structural features of electrical cabinets are described in Section 2. Secondly, numerical modeling of the electric cabinet using Finite Element Model (FEM) is given in Section 3. Finally, the methodology for generating the numerical modeling of the electric cabinet using the simplified approach is discussed in Section 4.

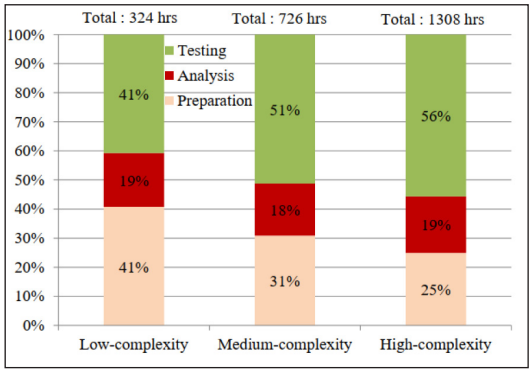

Figure 2. Work content and hours estimation for nonstructural qualification based on the complexity of the electrical equipment.[15]

2. IMPORTANT STRUCTURAL FEATURES OF ELECTRICAL CABINETS

Framing members, steel plates, and the connections between framing members and plates/framing members are the main components of a cabinet. The framing members are usually connected to each other using fasteners (i.e., weld, screw, or bolt). The enclosure steel panels are usually connected to the framing members via screw or bolt fasteners. The base-frame members of the cabinet structure are then anchored to the floor through channel-section frames using bolt connectors (Figure 3).[21]

In a cabinet structure, the frame members work similarly to the framing elements of a steel frame. During seismic loadings, the collapse of an electrical cabinet causes the following reasons: (i) failure of connections at the base or between plates with frame members, (ii) buckling of the plates, and (iii) buckling of the frame members.

Other components including operational, bracing, and isolation systems may contribute to the dynamic performance of the cabinet.[15] Operational attachments are any parts attached to the cabinet to maintain its active operation (Figure 4). The bracing attachments can improve the structural rigidity and reduce relative displacements of the cabinets. And the isolation reduces seismic demand and dynamic amplification in cabinets as well as modifying their dynamic characteristics.

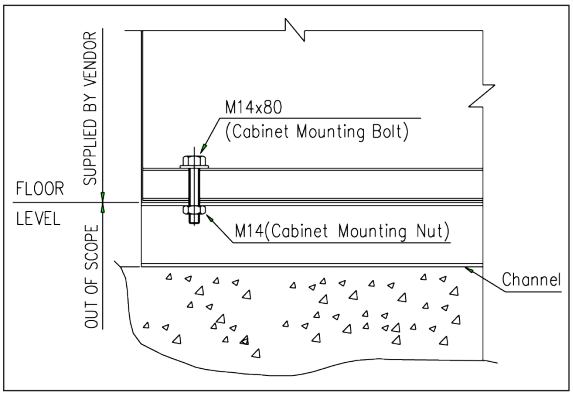

Figure 3. Details of anchor bolt.[20]

(a) Electrical conduilt [18]

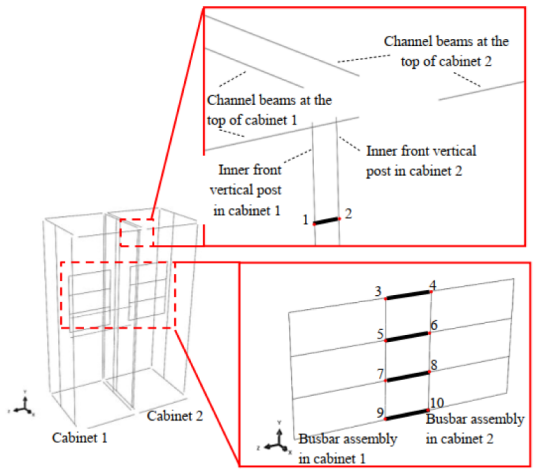

(b) Additonal bracing system [18]

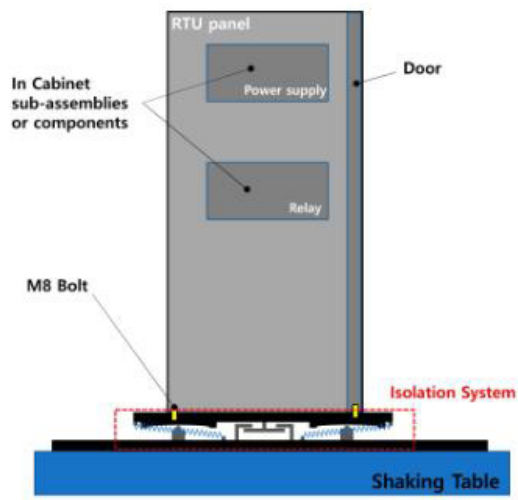

(c) Isolation system [20]

Figure 4. Components in the cabinet.

3. FULL FINITE ELEMENT MODELS

As empirical data has numerous limitations and large numbers of specimens cannot be tested on shake tables, it is more practical to evaluate the seismic vulnerability of electrical equipment using numerical techniques, such as finite element. Using Finite Element Model with the supports of finite element softwares is easy to capture the dynamic behavior of the cabinet under various boundary conditions and loading configurations.

In 1999, Gupta *et al.*[22] developed finite element models of 16 types of electric cabinets. One of them is the DGLSB cabinet (Figure 5) which is an individual unit and instrument mount on the doors and internal frame. This FE model were verified with the results reported by Rustogi and Gupta.[23] The outcomes from the analysis are used to evaluate in-cabinet response spectra needed in the seismic qualification of electric instruments.[24-25] Later, the method was modified by Gupta and Yang[26] to overcome limitations that were encountered during applications to actual cabinets. The results show that the contribution mode, called "significant mode", is a local mode of the cabinet in most cases. However, in some cases, the global cantilever mode of the cabinet may also be significant along with or without the local modes.

Likely, the FEM of the cabinet is generated using SAP2000 by Tran *et al.*,[27–29] as shown in Figure 6. The main-frames and sub-frames are modeled using the frame elements, and the steel plates are modeled using the shell elements. Plates and frames are connected by link elements. The connection between the door and main-frame is simulated as a hinge, which is fixed at five degrees of freedom. Meanwhile, the locks between panels and main-frames are fixed at three translational degrees of freedom. For the support boundary condition, the simplified pressure-cone method as stated by Shigley is adopted to calculate the stiffness of the anchor bolt.[30] Later, using this developed FEM, Cao *et al.*[31] proposed a simplified approach for assessing the seismic risks for cabinets. The method is a combination of fragility analysis and cumulative absolute velocity (CAV) analysis.

In reality, the cabinets will be connected together and how rational is the approach to consider the seismic response of a single electrical cabinet and its integration into the multi-cabinets

https://doi.org/10.52111/qnjs.2023.17301

(as called a "grouping effects") (Figure 7).[32–34] The grouping effect is the inclusion of the structural modification to the idea and it was considered in the form of two entities mainly the mass and stiffness provided by the cabinets. The rigid links are considered for connecting the cabinets, which is not inducing any change in the dynamic characteristic of the structure.

Regarding the impact of boundary conditions on the performance of electric cabinets, various researches are also studied. Rocking behavior of cabinet subjected to Reg. 1.60[35] was carried out by Jeon *et al.*[36] In this research, different models were developed using Abaqus and ANSYS, and verified using the experiment data.

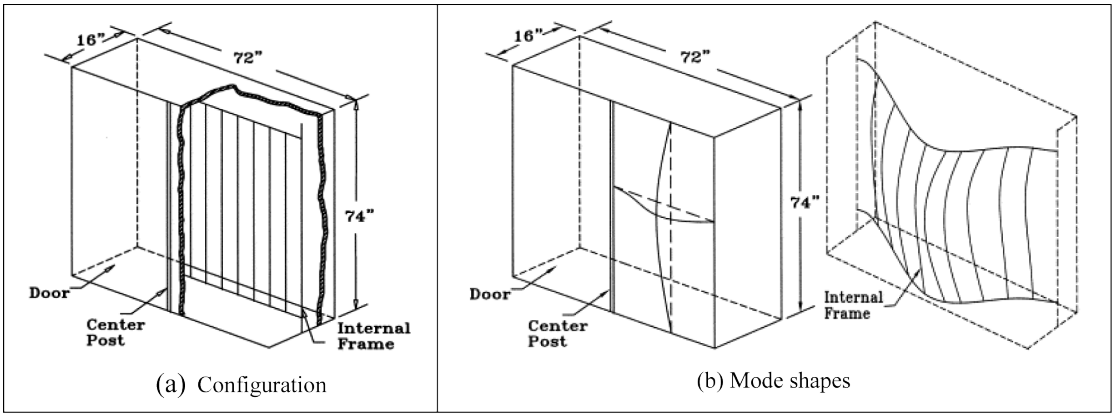

Figure 5. Cabinet models proposed, adapted from Gupta *et al.*[22]

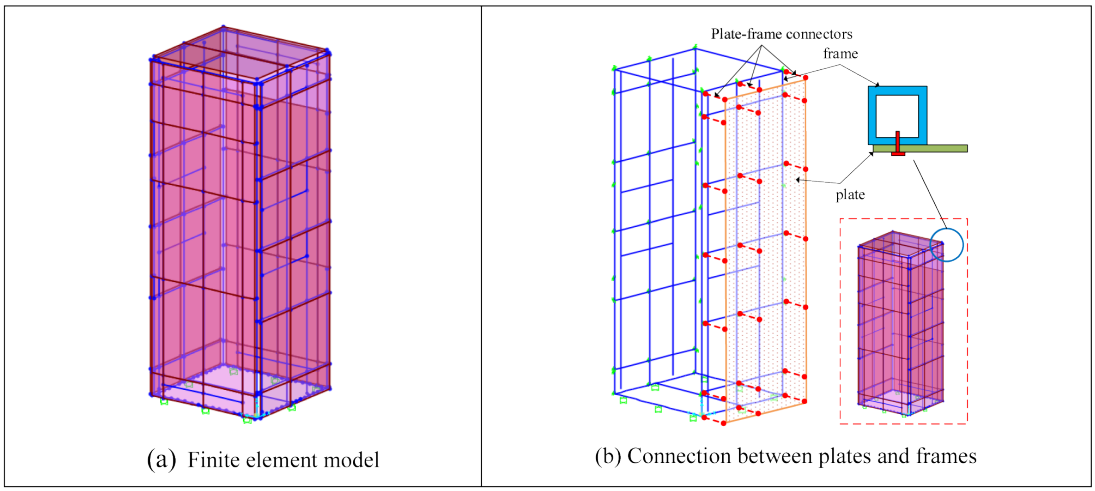

Figure 6. Cabinet models proposed, adapted from Tran *et al.*[27]

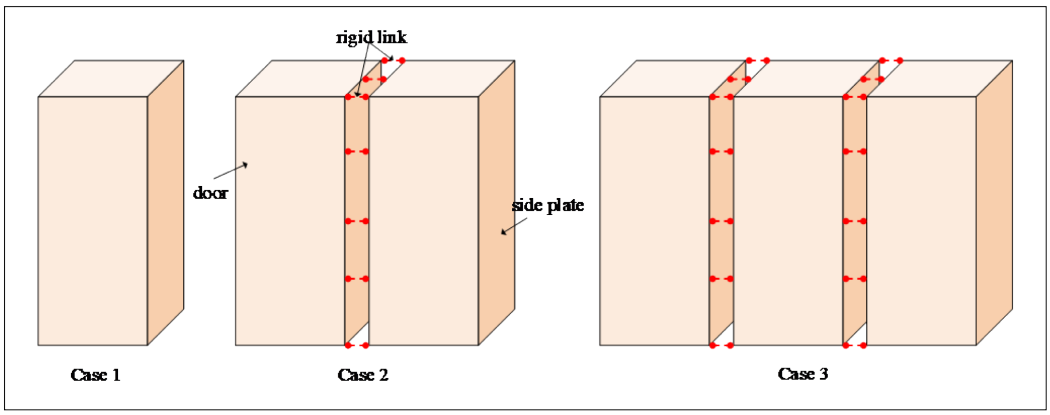

Figure 7. Typical cabinet models, adapted from Salman *et al.* [32,33]

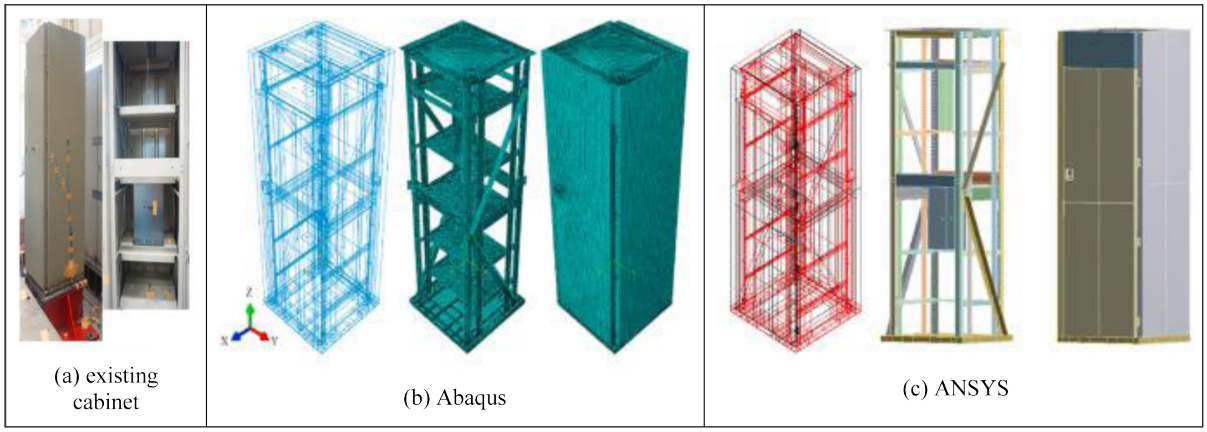

Figure 8. Finite element models of cabinet, adapted from Jeon *et al*. [36]

4. SIMPLIFIED FINITE ELEMENT MODELS

In 2016, Lim[18] developed a method to generate simplified finite element models for electrical cabinets. The model is comprised of beam elements, shell elements, and spring and constraint equations. These models can capture the nonlinear behavior of cabinet structure, such as the buckling of steel plates, failure of connectors, and the local buckling effect near the end of the framing members. In this research, two configurations of cabinet namely Class I and Class II are presented, as shown in Figure 9. Class I is a model of an electrical switchboard cabinet where all structural components are constructed from plain sections. Class II is the model with some applied improvements of the screw connections between plates and framing members. A comparison of the modeling features between Class I and Class II is summarized in Table 1. Besides, the effects of electric devices installed inside the cabinet (i.e., busbar, main circuit breaker, and meter devices) on the nonstructural performance were also studied.

Later, Tran *et al*.[37] also developed bare-frame model to capture the local buckling behavior of frame members. The numerical models are developed using OpenSees.[38] The fiber-based plasticity approach, which can capture the nonlinear behavior, is utilized. In this model, the elements must be discretized into fibers, as shown in Figure 10. Five integration points divide elements into sub-elements. To consider the nonlinear behavior, the relationship of stress-strain of each fiber on the cross-section of the sub-element (i.e., steel01, steel02) is defined.[39-41]

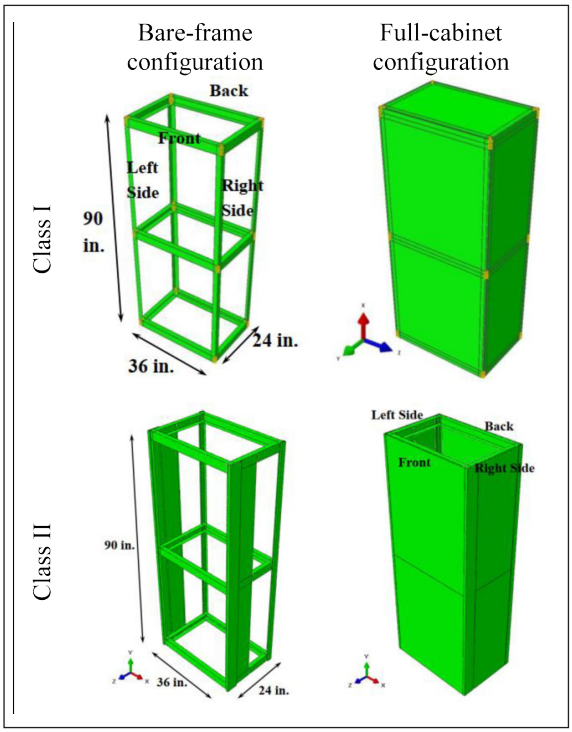

Figure 9. Cabinet models proposed, adapted from Lim.[18]

Table 1. Comparison between Class I and Class II configurations.

Structural components	Class I	Class II
Framing members	Hybrid Timoshenko beam model	Timoshenko beam model
Plates	Shell elements	Shell elements
Connections between framing members	Rotational springs and rigid beam constraints	Rotational springs and rigid beam constraints
Screw connection between plates and framing members	Rigid beam and warping constraints Translational springs	Rigid beam and warping constraints Translational springs Rotational springs

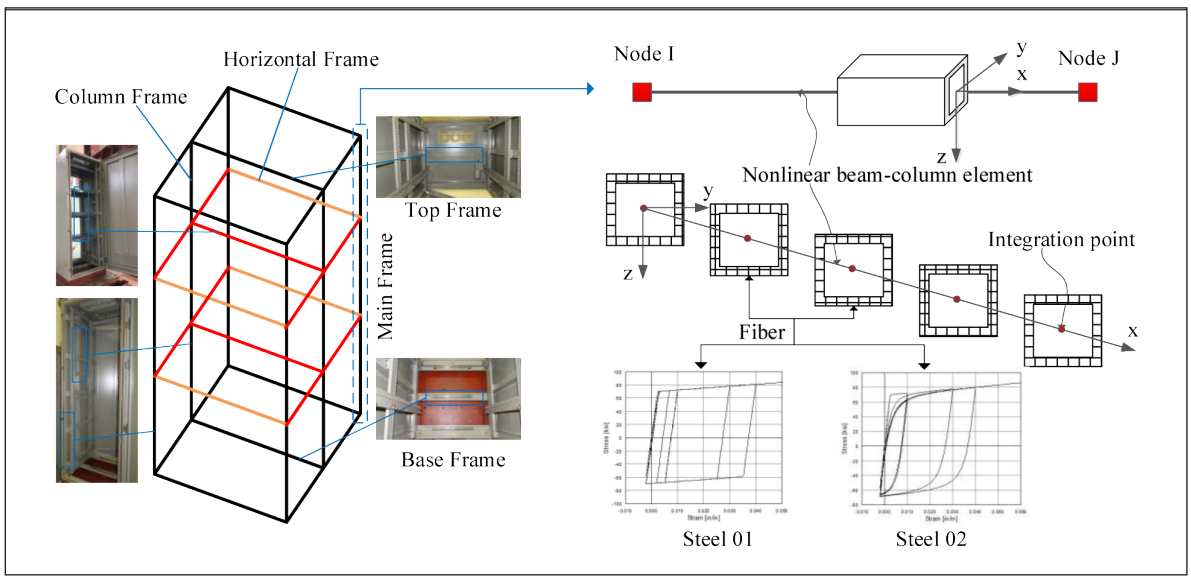

Figure 10. Cabinet models proposed, adapted from Tran *et al.*[37]

4. DISCUSSIONS

The development of the numerical models of the cabinet using different approaches is presented in this paper. The models using finite element approach are accurate to capture both local and global behavior of the cabinet. The global behavior of the frame members can affect the local mode shapes of the plates.

In practice, the simplified models are preferred to depict the global behavior rather than the full model which considers the local modes and requires time-consuming. However, it should be noted that the accuracy of the simplified models depends on the assumptions for idealization.

The application of the simplified models may be limit when considering the effects of local mode shapes or the occurring possibility of the buckling modes of sections.

5. CONCLUSIONS

This paper has collected and reviewed the methodologies used to develop the numerical model of the electric cabinet. A description of the important characteristics is presented first, followed by a description of modeling development. In each of them, the different strategies of structural modeling are discussed. The present paper has attempted to give an overview of the different research directions and it is expected to serve as a general reference and starting point to new researchers.

REFERENCES

1. T. T. Tran, T. H. Nguyen, D. Kim. Seismic incidence on base-isolated nuclear power plants considering uni- and bi-directional ground motions, *Journal of Structural Integrity and Maintenance*, **2018**, *3*, 86-94.

2. B. J. Goodno, N. C. Gould, P. Caldwell, P. L. Gould. Effects of the January 2010 haitian earthquake on selected electrical equipment, *Earthquake Spectra*, **2011**, *27*, 251-276.

3. L. Baccarini, M. Capretta, M. Casirati, A. Castaldi. *Seismic qualification tests of electric equipment for caorso nuclear plant: Comments on adopted test procedure and results*, IASMiRT, 1975.

4. T. T. Tran, A. T. Cao, T. H. X. Nguyen, D. Kim. Fragility assessment for electric cabinet in nuclear power plant using response surface methodology, *Nuclear Engineering and Technology*, **2019**, *51*, 894-903.

5. S. Cho, D. Kim, S. C. Design. A simplified model for nonlinear seismic response analysis of equipment cabinets in nuclear power plants, *Nuclear Engineering and Design*, **2011**, *241*, 2750-2757.

6. D. D. Nguyen, B. Thusa, T. S. Han, T. H. Lee. Identifying significant earthquake intensity measures for evaluating seismic damage and fragility of nuclear power plant structures, *Nuclear Engineering and Technology*, **2019**, *52*, 192-205.

7. M. K. Kim, I. K. Choi. *A failure mode evaluation of a 480V MCC in nuclear power plants at the seismic events*, 20th International Conference on Structural Mechanics in Reactor Technology, Espoo, Finland, 2009.

8. H. Hou, W. Fu, W. Wang, B. Qu, Y. Chen, Y. Chen, C. Qiu. Horizontal seismic force demands on nonstructural components in low-rise steel building frames with tension-only braces, *Engineering Structures*, **2018**, *168*, 852-864.

9. IEEE. *IEEE standard seismic testing of relays*, 1987.

10. K. K. Bancfyopadhyay, C. H. Hofmayer, K. M. Kassir, S. Shteyngart. *Seismic fragility of nuclear power plant components [PHASE II],* 1991.

11. T. T. Tran, D. V. Nguyen, G. -H. Beak, X. Thi, H. Nguyen, D. Kim. *A proposed numerical model for cabinets of nuclear power plants*, Transactions of the Korean Nuclear Society Spring Meeting Jeju, Korea, 2018.

12. B. G. Jeon, H. Y. Son, S. H. Eem, I. K. Choi, B. S. Ju. Dynamic characteristics of single door electrical cabinet under rocking: Source reconciliation of experimental and numerical findings, *Nuclear Engineering and Technology*, **2021**, *53*, 2387-2395.

13. L. D. Sarno, G. Magliulo, D. D'Angela, E. Cosenza. Experimental assessment of the seismic performance of hospital cabinets using shake table testing, *Earthquake Engineering & Structural Dynamics,* **2019**, *48*, 103-123.

14. B. S. Ju, H. Son, S. Lee, S. Kwag. Estimating seismic demands of a single-door electrical cabinet system based on the performance limit-state of concrete shear wall structures, *Sustainability*, **2022**, *14*, 5480.

15. J. A. Gatscher, G. L. McGavin, P. J. Caldwell. *Earthquake protection of building equipment and systems: bridging implementation gap*, ASCE Press, 2012.

16. J. Hur. *Seismic performance evaluation of switchboard cabinets using nonlinear numerical models*, Georgia Institute of Technology, 2012.

17. T. T. Tran, D. Kim. Uncertainty quantification for nonlinear seismic analysis of cabinet facility in nuclear power plants, *Nuclear Engineering and Design*, **2019**, *355,* 110309.

18. E. Lim. *A method for generating simplified finite element models for electrical cabinets*, Georgia Institute of Technology, 2016.

19. W. Jiang. *Direct method of generating floor response spectra*, University of Waterloo, 2016.

20. S. W. Kim, B. G. Jeon, D. W. Yun, W. Y. Jung and B. S. Ju. Seismic experimental assessment of remote terminal unit system with friction pendulum under triaxial shake table tests, *Metals*, **2021**, *11*(9), 1428.

21. T. T. Tran. *Modelling and simualtion of uncertianties for nuclear facilities and soil deposits*, Kunsan National University, 2020.

https://doi.org/10.52111/qnjs.2023.17301

22. A. Gupta, S. Rustogi, A. Gupta. Ritz vector approach for evaluating incabinet response spectra, *Nuclear Engineering and Design*, **1999**, *190*, 255-272.

23. S. Rustogi, and A. Gupta. Modeling the dynamic behavior of electrical cabinets and control panels: Experimental and analytical results, *Journal of Structural Engineering,* **2004**, *130*(3), 511-519.

24. G. N. Geannakakes. Natural frequencies of arbitrarily shaped plates using the Rayleigh-Ritz method together with natural co-ordinate regions and normalized characteristic orthogonal polynomials, *Journal of Sound and Vibration*, **1995**, *182*, 441-478.

24. C. S. Kim, P. G. Young, S. M. Dickinson. On the flexural vibration of rectangular plates approached by using simple polynomials in the Rayleigh-Ritz method, *Journal of Sound and Vibration,* **1990**, *143*, 379-394.

26. A. Gupta, J. Yang. Modified Ritz vector approach for dynamic properties of electrical cabinets and control panels, *Nuclear Engineering and Design,* **2002**, *217*, 49-62.

27. T. T. Tran, A. T. Cao, T. H. X. Nguyen, D. Kim. Fragility assessment for electric cabinet in nuclear power plant using response surface methodology, *Nuclear Engineering and Technology*, **2019**, *51*, 894-903.

28. T. T. Tran, P. C. Nguyen, G. So, D. Kim. Seismic behavior of steel cabinets considering nonlinear connections and site-response effects, *Steel and Composite Structures*, **2020**, *36*, 17-29.

29. T. T. Tran, A. T. Cao, D. Kim, S. Chang. Seismic vulnerability of cabinet facility with tuned mass dampers subjected to high- and low-frequency earthquakes, *Applied Sciences*, **2020**, *10*(14), 4850.

30. R. G. Budynas, J. K. Nisbett. *Shigley's mechanical engineering design*, McGraw-hill, New York, 2011.

31. A. T. Cao, T. T. Tran, T. H. X. Nguyen, D. Kim. Simplified approach for seismic risk assessment of cabinet facility in nuclear power plants based on cumulative absolute velocity, *Nuclear Technology,* **2019**, *206*, 1-15.

32. K. Salman, T. T. Tran, D. Kim. Seismic capacity evaluation of NPP electrical cabinet facility considering grouping effects, *Journal of Nuclear Science and Technology*, **2020**, *57*, 1-13.

33. K. Salman, T. T. Tran, D. Kim. Grouping effect on the seismic response of cabinet facility considering primary-secondary structure interaction*, Nuclear Engineering and Technology*, **2019**, *52*, 1318-1326.

34. S. G. Cho, K. Salman. Seismic demand estimation of electrical cabinet in nuclear power plant considering equipment-anchor-interaction, *Nuclear Engineering and Technology*, **2022**, *54*, 1382-1393.

35. *USNRC RG 1.60. Design response spectra for seismic design of nuclear power plants, Rev. 2. U.S. Nuclear Regulatory Commission,* Washington, DC, USA, July 2014.

36. B. G. Jeon, H. Y. Son, S. H. Eem, I. K. Choi and B. S. Ju. Dynamic characteristics of single door electrical cabinet under rocking: Source reconciliation of experimental and numerical findings, *Nuclear Engineering and Technology*, **2021**, *53*(7)*,* 2387-2395.

37. T. T. Tran, K. Salman, D. Kim. Distributed plasticity approach for nonlinear analysis of nuclear power plant equipment: Experimental and numerical studies, *Nuclear Engineering and Technology*, **2021**, *53*, 3100-3111.

38. F. McKenna. OpenSees: a framework for earthquake engineering simulation, *Computing in Science & Engineering*, **2011**, *13*, 58-66.

39. P. C. Nguyen, S. E. Kim. Distributed plasticity approach for time-history analysis of steel frames including nonlinear connections, *Journal of Constructional Steel Research*, **2014**, *100*, 36-49.

40. P. C. Nguyen, T. T. Nguyen, Q. X. Lieu, T. T. Tran, P. T. Nguyen, T. N. Nguyen. Nonlinear inelastic analysis for steel frames, *Lecture Notes in Civil Engineering,* **2020**, *80*, 311-317.

41. P. C. Nguyen, T. T. Tran, T. N. Nguyen. Nonlinear time-history earthquake analysis for steel frames, *Heliyon*, **2021**, *7*(8), e06832.

TẠP CHÍ KHOA HỌC
TRƯỜNG ĐẠI HỌC QUY NHƠN

Liên kết hydrogen không cổ điển: Tổng quan chính về sự chuyển dời xanh hoặc đỏ của tần số dao động hóa trị liên kết C-H

Nguyễn Trường An, Vũ Thị Ngân*, Nguyễn Tiến Trung*

Phòng thí nghiệm Hóa học tính toán và Mô phỏng (LCCM), Bộ môn Hóa học, Khoa Khoa học Tự nhiên, Trường Đại học Quy Nhơn, Việt Nam

Ngày nhận bài: 19/01/2023; Ngày nhận đăng: 27/03/2023; Ngày xuất bản: 28/06/2023

TÓM TẮT

Tổng quan hiện tại hướng tới một cái nhìn tổng quan về sự chuyển dời xanh hoặc đỏ của tần số dao động hóa trị liên kết C-H với nguyên tử carbon ở các trạng thái lai hóa khác nhau (C_{sp}, C_{sp2}, C_{sp3}). Các đặc điểm của liên kết hydrogen không cổ điển bao gồm sự thay đổi độ dài và tần số dao động hóa trị liên kết C-H khi tạo phức đã được xem xét kỹ lưỡng với C-H có độ phân cực khác nhau đóng vai trò phần tử cho proton và các nguyên tử O, S, Se, Te, N hoặc electron π đóng vai trò phần tử nhận proton. Kết quả cho thấy, so với các nguyên tử S, Se và Te, nguyên tử O đóng vai trò quan trọng đối với sự chuyển dời xanh tần số dao động hóa trị C-H tham gia liên kết hydrogen. Mức độ chuyển dời đỏ hoặc xanh của tần số dao động hóa trị C-H chủ yếu được quyết định bởi độ phân cực (DPE) của liên kết C-H và độ base pha khí (PA) của phần tử nhận proton trong monomer ban đầu, bên cạnh tương tác yếu có liên quan và dạng cấu trúc hình học của phức tạo thành. Hơn nữa, tỉ số DPE/PA có thể được đề xuất để phân loại liên kết hydrogen cổ điển và không cổ điển.

Từ khóa: *Chuyển dời xanh, trạng thái lai hóa của carbon, độ phân cực, độ base pha khí, tỉ lệ DPE/PA.*

**Tác giả liên hệ chính.*
Email: nguyentientrung@qnu.edu.vn; vuthingan@qnu.edu.vn

QUY NHON UNIVERSITY
JOURNAL OF SCIENCE

Non-conventional hydrogen bonds: A brief review of blue shift or red shift of C-H stretching frequency

Nguyen Truong An, Vu Thi Ngan*, Nguyen Tien Trung*

Laboratory of Computational Chemistry and Modelling (LCCM), Department of Chemistry, Faculty of Natural Sciences, Quy Nhon University, Vietnam

Received: 19/01/2023; Accepted: 27/03/2023; Published: 28/06/2023

ABSTRACT

The present work is geared towards having an overview of the blue shift or red shift of C-H stretching vibration with various hybridized carbon atoms (C_{sp}, C_{sp2}, C_{sp3}). The features of the non-conventional hydrogen bond, including changes in length and stretching frequency of the C-H bond upon complexation, were thoroughly reviewed based on C-H proton donors with different polarity and various proton acceptors such as O, S, Se, Te, N atoms or π electrons. The results show that the O atom, as compared to the S, Se, and Te ones acting as proton acceptors, plays a peculiar role in the C-H blue shift of stretching frequencies involving hydrogen bonds. It is found that the magnitude of red- or blue-shift of the C-H stretching frequency in the hydrogen bond is mainly determined by the C-H polarity (DPE) and gas phase basicity (PA) of the proton acceptor in the isolated isomer, besides relevant weak interactions and the geometrical structure of the formed complex. Furthermore, for the categorization of conventional and non-conventional hydrogen bonding, an intriguing DPE/PA index should be suggested.

Keywords: *Blue shift, hybridization of carbon, polarity, gas-phase basicity, DPE/PA ratio*.

1. INTRODUCTION

Understanding non-covalent interactions is critical for unraveling the mysteries of cellular processes in health concerns and developing novel treatment protocols/methods, medicines, and materials.[1] Among them, a hydrogen bond A–H···B is a unique interaction that is important in many fields of research, including molecular recognition, protein folding, structural organization of nucleic acids, crystal and polymer packing, self-assembly, supramolecular chemistry, solvation, and even organic synthesis.[2-5] In a conventional hydrogen bond, A and B are highly electronegative elements, and the hydrogen atom which is strongly electropositive, plays a bridging.[4,6] For example, the conventional hydrogen bonds including N-H···O, N-H···N, O-H···O, and O-H···N, which play the most important role in supramolecular chemistry and structural biology, are strong and mostly driven by the electronegativity differences between the proton donor and acceptor atoms.[7-13] The characteristics of a conventional hydrogen bond are the A–H bond elongation along with a decrease in stretching frequency, which is called a red-shifting

**Corresponding author.*
Email: nguyentientrung@qnu.edu.vn; vuthingan@qnu.edu.vn

https://doi.org/10.52111/qnjs.2023.17302

hydrogen bond (abbreviated as RSHB). It is well known that a lower strength of the A-H bond in the hydrogen bond in comparison with that in the isolated monomer results from a primarily electrostatic force of attraction between the H atom and B atom in the complex.[14] For the non-conventional hydrogen bond, an A-H elongation, and its stretching frequency red shift are suggested by a n(B)→σ*(A–H) intermolecular hyperconjugation overcoming an increase in the s-character and polarization of the A–H bond.[15]

Since the 1980s, however, the non-conventional hydrogen bond with the opposing features including of a shortening in the A-H bond length and a concomitant increase in stretching vibration following complexation has been found, and named the blue-shifting hydrogen bond (abbreviated hereafter as BSHB).[16] Nowadays, the BSHB's characteristics are well observed and have been studied by both accurate quantum calculations and high-resolution experiments. Although the characteristics of the blue shift phenomenon in hydrogen bonds are known clearly, the nature of this new hydrogen bond type is still questionable.

Numerous hypotheses/theorems have been proposed to explain the physical origin of the blue-shifting or red-shifting of non-conventional hydrogen bonds, however, no general explanation has been effectively applied. Among the available rationalizations for the BSHB, some schemes have attracted the most attention, including (*i*) The first explanation proposes a two-step mechanism in which electron density is mainly transferred from B to the remote atoms related to A rather than to the σ*(A–H) orbital, and therefore the A–H bond is shortened as a result of structural re-organization of the proton donor framework.[17-19] (*ii*) The second theorem attributes the short-range repulsive forces encountered by the complex's H atom as the complex attempts to stabilize itself, which would be the reason for the contraction of the A–H bond length.[20,21] (*iii*) The third scheme is that the observed contraction is due in part to the impact of the electric field around B, because an electric field is detected after the A–H bond length is reduced.[22,23] (*iv*) The fourth theory is based on two opposite factors: the A atom's *s*-character percentage and the polarity of the A–H bond on one side, and the intermolecular hyperconjugative interaction on the other, which transfers electron density from the *n*(B) lone pair to the σ*(A–H) orbital on the other side. The A–H bond is shortened when the former prevails. When the latter surpasses the former, the A–H bond is lengthened.[15,24] (*v*) The fifth scheme of the A–H bond contraction along with the increase in stretching frequency proposes that an electron density transfer comes from the presence of B on the right-hand side of the H atom to the A–H bond in the A–H···B hydrogen bond.[25]

Other explanations of BSHB in the non-conventional complexes have been continuously presented. For instance, according to Wei Wu *et al.*, the rivalry between the long-range electrostatic interaction between the A-H bond and the B atom and the short-range hyperconjugative interaction causes the direction of shift in the A-H stretching frequency.[26] Based on the Valance Bond Self-Consistent Field (VBSCF) approach, the authors proposed that the covalent state of the A-H bond tends to shift to blue, whereas its ionic state causes a red shift of stretching frequency.[27] The competition between the two properties induces changes in the A-H stretching frequency. Very recently, the Head-Gordon group from UC Berkeley suggested that Pauli repulsion leads to a contraction of the A-H bond accompanied by an increase in its stretching frequency, whereas electrostatic and dispersion forces cause the A-H bond to lengthen and decrease its stretching frequency.[28] Long-range electrostatic and Pauli exchange interactions overcome the overall impact of polarization and charge transfer interactions, causing the A-H bond to shorten and its stretching frequency to increase.[29] In general, each scheme has benefits

and disadvantages, but they all explain the BSHB phenomenon using the features of the hydrogen-bonded complex.

Among conventional and non-conventional hydrogen bonds, the hydrogen bond involving the C-H bond as the proton donor is extremely important because of its prevalence and diversity in nature. Although their binding energies are typically less than 5÷6 kcal mol^{-1} (~21÷25 kJ mol^{-1}), their cumulative contributions prove to be considerable in many cases. Weak hydrogen bonds are a decisive factor in the structure, conformation, and tautomeric preferences of many organic compounds in their crystalline phases, as well as the functional structures of biological macromolecules in living systems.[5,30-33] For instance, the presence of hydrogen bonds C-H···O/S, C-H···N, C-H···π, C-H···X (X = F, Cl, Br) has been observed in molecular clusters, enzymatic mechanisms, proteins, DNA, RNA, crystal packing, etc.[34-38] Every protein contains a huge number of C–H···O/N hydrogen bonds which can occur in thousands of large proteins. Experimentally and theoretically, a wide range of non-conventional hydrogen bonds involving the C-H bond in C-H···O/N/halogen/π hydrogen bonds were found, in which the C-H···O/N hydrogen bonds are most frequently seen utilizing IR and Raman spectroscopy.[36,39-53,57,61] Trudeau *et al.* established the first experimental proof for the blue shift of C-H stretching frequency by investigating complexes of fluoroparaffins and several proton acceptors.[16] Since the 1980s, evidence of an increase in the C-H stretching frequency in hydrogen bonds has been detected in several complexes.[54-56] Due to the vast quantity and rich diversity of C-H bonds in organic chemistry, the organic synthesis approach based on activation and functionalization of C-H bonds is the primary strategy at the moment.[57-59] The existence of hydrogen bonds comprising C-H bonds as proton donors in the intermediates is seen in this approach, which helps the creation of desirable products.[2,60] Remarkably, the vibrational spectral parameters of the hydrogen bond (blue-shift or red-shift) have been recently applied as direct spectroscopy evidence for addressing several matters of concern such as environmental problems[126-128] or the shortage of valuable materials.[129-130]

Nowadays, characteristics of red or blue shifting stretching frequencies in non-conventional hydrogen bonds, particularly the participation of the C_{sp3}-H covalent bond as a proton donor, have received a lot of theoretical and experimental attention. A variety of hydrogen-bonded binary complexes of various haloforms were studied in a variety of physical environments, including supersonic jet expansion, inert gas matrix, cryoliquid, and gas phase at room temperature.[61-69,86] In most situations, the C_{sp3}-H covalent bond exhibits a red-shift of stretching frequency in addition to a blue-shift in certain cases, implying its weakening, similar to the characteristics of conventional hydrogen bonds. However, the underlying reason for the C_{sp3}-H bond shortening or lengthening and its corresponding frequency change remains a subject of debate. Apart from the initial results which are derived primarily from the physicochemical properties of hydrogen bonds with the C_{sp3}-H moiety and numerous proton acceptors, many investigations into various polarizations of the C_{sp3}-H bond were conducted to unravel the origin of BSHB and the classification of the hydrogen bond. The medium polarity of the C_{sp2}-H covalent bond between C_{sp3}-H and C_{sp}-H bonds makes its stretching frequency shift more sensitive when interacting with different proton acceptors. As a result, the significant stretching frequency blue shifts have recently been found in the C_{sp2}-H bond upon the formation of hydrogen-bonded complexes.[70-71] Our recent findings indicate that it is more appropriate to consider the C-H blue or red shift of non-conventional hydrogen bonds from a different perspective, which is based on inherent properties such as the polarity of the C-H bond by deprotonation enthalpy (DPE) and gas phase

https://doi.org/10.52111/qnjs.2023.17302

basicity of the B counterpart by proton affinity (PA) in the isolated monomers acting as proton donors and acceptors.[72,73,108] We also propose that the DPE/PA ratio in an isolated monomer be used to predict the type of hydrogen bond that would be found upon complexation.[100,108]

The primary purpose of the present review is to give insight into the characteristics of non-conventional hydrogen bonds involving the different hybridized C-H covalent bonds, which include changes in length and stretching frequency of the C-H bond, as well as give a clearer explanation for the formation of blue or red shifting hydrogen bonds. The effect of the gas phase basicity of the proton acceptor on the characteristics of non-conventional hydrogen bonds is also another purpose of this overview. It is noted worthy that our recent results about hydrogen bonds are also used for discussion and comparison with several authors in this work.

2. THEORETICAL METHODS

The quantum chemical methods available in the packages GAUSSIAN (09), AIMALL, GenNBO 5.G, Psi4, SAPT2012.2, NCIPlot, VMD 1.9.3, Gnuplot, Multiwfn… were used for relevant calculations.[74-82] Methods with high accuracy such as perturbation theory method (MP2), coupled cluster method (CCSD(T)) and density functional theory (DFT) including ωB97XD, M06-2X, B3LYP-D3… in combination with suitable basis sets depending on investigated systems were employed. The MP2 method, in conjunction with the basis sets aug-cc-pVDZ, aug-cc-pVDZ-pp, aug-cc-pVTZ, aug-cc-pVTZ-pp, 6-311++G(3df,2pd), def2-TZVPD… was utilized to optimize the geometries of monomers and complexes. Geometries of the monomer and complex are optimized without symmetry constraints at the chosen suitable level of theory. The infrared spectrum is subsequently calculated for stable structures on the potential energy surfaces in order to determine the stretching vibration modes of the monomer and complex. Deprotonation enthalpies (DPE) and proton affinity (PA) of monomers in investigated systems were calculated at the coupled cluster level CCSD(T) with large basis sets such as 6-311++G(3df,2pd), aug-cc-pVTZ, aug-cc-pVQZ… to obtain more accurate energetic values.

3. DISCUSSION

With a strong electron donor (B) like O, S, Se, Te atoms or others such as N or even π electrons, the question arises whether the influence of different hybridization from the C atom to the magnitude of changes in length and stretching frequency of the C-H bond. To answer this question, several complexes with C-H···chalcogen (O, S, Se, Te)/N/π hydrogen bonds were investigated, and relevant discussion is mentioned as follows.

3.1. C-H···O/S/Se/Te hydrogen bonds

A large blue shift of 30 cm^{-1} upon complexation was first found for C_{sp3}-H···O contacts in fluoroform···oxirane complex.[46] Chung *et al*. reported a C_{sp3}-H blue shift by 7 cm^{-1} and 5 cm^{-1} for the C_{sp3}-H···O non-conventional hydrogen bonds in the gas phase for the complexes between $CHCl_3$/$CDCl_3$ and SO_2. The C_{sp3}-H···O interactions between CF_nH_{4-n} (n= 1,2,3) and H_2O, CH_3OH, or H_2CO were studied at several levels of theory, which show a C_{sp3}-H contraction and a blue shift of its stretching vibration (5-47 cm^{-1}).[21] Similarly, a blue shift of 47 cm^{-1} was theoretically predicted for the F_3CH···$OHCH_3$ complex at the MP2/6-311+G(d,p) level.[83] In a computational study, the complex between triformylmethane and $CHCl_3$ was considered at the MP2/SDD level with the blue shift of C_{sp3}-H stretching frequency in $CHCl_3$ by 19 cm^{-1}.[17] The experimental blue shift of C_{sp3}-H stretching frequency in triformylmethane in liquid $CHCl_3$ is 7 cm^{-1}.[54] In the gas phase at room temperature, the C-D blue-shifted stretching frequency of $CDCl_3$ was detected at 7.1, 4.0, and 3.2 cm^{-1} in complexation with CH_3HCO, $(CH_3)_2CO$, and $C_2H_5(CH_3)CO$, respectively.[69] Through ab initio calculation, the blue shift for C_{sp3}-H bond is also found for the C_{sp3}-H···O hydrogen bonds in complexes formed from the interaction of CHX_3

(X = F, Cl, Br) with HNO. Notably, the low polarity of the C_{sp3}-H bond causes the shortening of the C_{sp3}-H bond and the blue shift of its stretching frequency (Δr_{CH} = -0.0009÷-0.0025 Å and $\Delta\nu_{CH}$ = 18÷41 cm^{-1}). The C_{sp3}-H red-shifting stretching frequency of C_{sp3}-H···Se hydrogen bond was observed for Q_3C-H···SeH_2 (Q = Cl, F, and H) at the MP2/aug-cc-pVTZ level, while the small blue shift was proposed in F_3CH···SeH_2 at a nonlinear structure ($\Delta\nu$ = -15 cm^{-1}).[84] In general, for the same proton donor of C_{sp3}-H, the magnitude of C_{sp3}-H stretching frequency blue shift in C_{sp3}-H···O hydrogen bond is much larger than that in C_{sp3}-H···Se bond.

Besides, some reports indicate that the medium is important in determining the category as well as the magnitude of the C_{sp3}-H stretching frequency shift.[85,86] Indeed, in solution, blue-shifted complexes of $CHCl_3$ and small cyclic ketones were suggested ($\Delta\nu_{CH}$ = 1÷5 cm^{-1}), and as the size of the ketone decreased, the C-H blue shift was enhanced.[87] In complexes of $HCClF_2$ and $HCCl_2F$ with $(CH_3)_2O$ in liquid krypton and liquid argon, a blue-shifted C_{sp3}-H···O bond was reported.[66] The C-H bond in the F_3CH···OH_2 complex is blue-shifted by 20.3 and 32.3 cm^{-1} in argon and neon matrix, respectively.[88] The C-H stretching frequency decreases by 38 and 14 cm^{-1} in the binary complexes of $CHCl_3$ with acetone-d_6 and H_2O prepared in a matrix.[46] Ito *et al*. reported a C-H red shift of 14 cm^{-1} in the $CHCl_3$···H_2O complex in argon matrix at 20 K.[85] Very recently, a C_{sp3}-H red shift of 21.9 cm^{-1} in C_{sp3}-H···O hydrogen bond was reported for the $CHCl_3$···CH_3OH complex in N_2 matrix using experimental IR spectra.[89] In general, the theoretical calculations are in good accordance with the observed IR data.[61,90,91] Moreover, using ab initio calculations and Monte Carlo simulations, the formation of the C_{sp3}-H···S hydrogen bond upon complexation of halothane ($CHBrClCF_3$) with dimethyl sulfide was investigated in solutions of liquid krypton using IR and Raman spectroscopy. In the dimethyl sulfide complex, the halothane C_{sp3}-H stretching mode was found to be red-shifted by 43 cm^{-1}.[92] It can be found that a decrease of C_{sp3}-H stretching frequency blue shift as well as an increase in its stretching frequency red shift detected in the medium were proposed, especially in a noble gas matrix (N_2, Ar, Ne, Kr,…), within which the noble gas is used as an unreactive host material to trap guest particles (atoms, molecules, ions, etc) being diluted in the gas phase.

Considering C_{sp2}-H stretching vibration, the hydrogen-bonded interaction of formic acid-, formaldehyde-, formylfluoride-nitrosyl hydride complexes were studied at 6-311++G(2d,2p) basis set. In which, C_{sp2}-H···O blue-shifted hydrogen bonds were found in the complexes by 19÷27 cm^{-1}.[93] The blue-shifted C_{sp2}-H···O interactions of benzene, phenol, and indole with water were calculated at the MP2/6-31+G(d,p) theory of level ($\Delta r(C_{sp2}\text{-H})$ = -0.1÷-0.8 mÅ; $\Delta\nu(C_{sp2}\text{-H})$ = 17÷33 cm^{-1}).[94] Notably, the very small red-shifted C_{sp3}-H···O hydrogen bonds (Δr_{CH} = 0.0003÷0.0011 Å; $\Delta\nu_{CH}$ = -2÷-8 cm^{-1}) and large blue-shifted C_{sp2}-H···O hydrogen bonds (Δr_{CH} = -0.0041÷-0.0069 Å; $\Delta\nu_{CH}$ = 55÷85 cm^{-1}) were observed in complexes of CH_3CHO with HNO at different levels of theory.[95]

Tri *et al.* conducted a high-level theoretical investigation of the stable structures of interactions between aldehydes RCHO (R = CH_3, NH_2, F, Cl, Br) and cyanides XCN (X = H, F).[73] The result shows that the C_{sp2}-H···O hydrogen bond plays an important role in the stabilization of RCHO···HCN complexes. Furthermore, the results suggest that the blue shift is affected by both the polarity of the C_{sp2}-H bond in the proton donor and the gas-phase basicity of the proton acceptor. The blue shift of the C_{sp2}-H bond in the C_{sp2}-H···O hydrogen bond is also observed in interactions of ethylene and its 1,2-dihalogenated form with CO_2, in which the magnitude of C_{sp2}-H distance contraction depends on the polarization of the C_{sp2}-H bond. Notably, a contraction of C-H bond length and a blue shift of its stretching frequency were obtained at a high theoretical

https://doi.org/10.52111/qnjs.2023.17302

level for gas phase complexes between XCHZ and CO_2 (X = H, F, Cl, Br, CH_3; Z = O, S) (with Δr_{C-H} = -0.4÷-1.8 mÅ and $\Delta\nu_{C-H}$ = 10÷27 cm^{-1}).[96]

Remarkably, at the B3LYP/6-311++G(d,p) level, the findings revealed that when a CH_3CHO molecule interacts with two H_2O molecules, the stretching frequency of the C_{sp2}-H bond increases by around 93 cm^{-1}.[70] The blue shifts of $\nu(C_{sp2}$-H) stretching vibration were found to be 45 and 66 cm^{-1} as HCHO complexed with one and two waters, respectively.[97] A considerable C_{sp2}-H blue shift, up to 81÷96 cm^{-1} was seen in the C_{sp2}-H···O hydrogen bond formed by the interactions of RCHZ (R = H, F, Cl, Br, CH_3, NH_2; Z = O, S) with HCOOH.[71] A study using ab initio calculations by Cuc *et al*. shows a large C_{sp2}-H blue shift in the C_{sp2}-H···O hydrogen bonds (92 cm^{-1} in $CH_3CHO\cdots 2H_2O$), which is compared to smaller blue shifts in C_{sp2}-H···S/Se/Te ones detected for the first time.[98] This result implies a predominant role of water in enhancing the significant C_{sp2}-H blue shift of stretching vibration upon complexation, which is also reported by Trung *et al*. of the significance of water and intramolecular interaction with a significant blue shift of C_{sp2}-H stretching frequency in binary complexes between the chalcogenoaldehydes and water ($\Delta\nu_{CH}$ = 109 cm^{-1}).[99] Recently, a significant C_{sp2}-H blue shift up to 104.5 cm^{-1} was reported by An *et al*. in binary complexes between CH_3CHO and CH_3CHS with substituted carboxylic and thiocarboxylic acids.[100] These suggested that the large magnitude of C_{sp2}-H blue shift in C_{sp2}-H···O bond is mainly supported by the presence of a strong O-H···O hydrogen bond. Remarkably, the C_{sp2}-H blue shifts in the C_{sp2}-H···O hydrogen bonds are substantially larger than those in the C_{sp2}-H···S/Se/Te ones, while electronegativity of O atom is higher than that of S, Se, and Te one.

The C_{sp}-H···O red-shifted hydrogen bond in $HNO\cdots C_2H_2$ binary complex was studied by Ying *et al*. through ab initio MO and DFT with different basis sets ($\Delta\nu_{CH}$ = -6 ÷ -22 cm^{-1} with the standard method and $\Delta\nu_{CH}$ = -6 ÷ -19 cm^{-1} with the counterpoise-corrected method).[101] Ying *et al*. suggested that the red-shifted vibrational frequencies for C_{sp}-H stretch in C_{sp}-H···O hydrogen bonds. The red shift of C_{sp}-H stretching vibration was also reported by Andersen *et al*. in the complexes formed by hydrogen-bonded interaction between C_2H_2 and H_2O ($\Delta\nu_{CH}$ = -7.7 cm^{-1}).[102]

It can be seen that in most cases when the proton donor is a sp^2/sp^3-hybridized C atom, its interaction with a proton acceptor results in the blue- or red-shift of C-H stretching frequency, while the red shift is a feature of hydrogen bond with sp-hybridized C atom. The red or blue shift in C_{sp}-H/C_{sp2}-H/C_{sp3}-H···O hydrogen bonds is strongly associated with the different polarity of the C-H bond in the isolated monomer, which is caused by the difference of the electronegativity of C atom based on hybridization state. In short, it is found that the blue shift is larger for the C_{sp2}-H/C_{sp3}-H···O non-conventional hydrogen bonds than for the C_{sp2}-H/C_{sp3}-H···S/S/Te ones in spite of the larger electronegativity of the O atom relative to S, Se and Te one. Besides, it is noted worthy that a remarkable role of water and O-H···O bond generates a considerable blue shift in C_{sp2}-H stretching frequency in the binary or ternary complexes.

3.2. C-H···N hydrogen bond

The C_{sp3}-H···N BSHB with a calculated blue shift of the C-H stretching frequency of 30 cm^{-1} in the $CHF_3\cdots NH_2C_6H_5$ complex was reported first by Fan *et al*. [103] Herrebout *et al*. [51] observed a C_{sp3}-H blue shift of 7.6 cm^{-1} or 3 cm^{-1} in the complexes of CHF_3 with NH_3 or pyridine at low temperature (188 K).[51] The C_{sp3}-H blue shift in the C_{sp3}-H···N hydrogen bond between proton donors of FH_2CH, F_2HCH and proton acceptors of CH_3NH_2, CH_2NH (with N acceptor) was found at MP2/6-31+G(d,p) level ($\Delta\nu_{CH}$ = 6÷25 cm^{-1}).[104] A modest blue shift of around 3 cm^{-1} was reported by Rutkowski *et al*. when $CHCl_3$ was introduced to CD_3CN in liquefied Kr at ~120 K.[65] In 2019, the slight C_{sp3}-H blue shifts of 8.7 cm^{-1}

and 8.6 cm^{-1} for the C_{sp3}-H···N hydrogen bonds in the $Cl_3CH···NCCH_3$ and $Cl_3CH···NCCD_3$ were observed by Fourier transform infrared spectroscopy, while the C_{sp3}-H red shift was reported for both complexes in the Ar matrix.[86] The C_{sp3}-H blue shift was observed for the C_{sp3}-H···N hydrogen bond in complexes formed by the interaction of trihalomethanes CHX_3 (X = F, Cl, Br) with HNO (nitrosyl hydride) at MP2/6-311++G(d,p).[105] Furthermore, Behra *et al*. reported a C_{sp3}-H blue shift of 9 cm^{-1} in the vapor phase at room temperature for the binary complex of $CHCl_3$ and CH_3CN, although Ito suggested a red shift of 25 cm^{-1} in an argon matrix earlier.[85-86]

Hippler reported a C_{sp3}-H···N hydrogen-bonded binary complex of $CHCl_3$ with NH_3 in the gas phase at room temperature with a C_{sp3}-H red shift of 17.5 cm^{-1}.[61] However, the magnitude of its red shift was risen to 38 cm^{-1} in a supersonic jet expansion,[61] and in an argon matrix, the red shift was still larger, *ca.* 45 cm^{-1}.[61,106] The complex of halothane with NH_3 exhibited similar shifting behavior of C_{sp3}-H spectra.[107] The observed red shift of C_{sp3}-H stretching frequency in the gas phase was found to be substantially less at room temperature (30.5 cm^{-1}) than in cryoliquids (55 cm^{-1} in liquid argon at 128 K, 49 cm^{-1} in liquid krypton at 173 K, and 42 cm^{-1} in liquid xenon at 228 K). The red shift of C_{sp3}-H stretching vibration by 4÷11 cm^{-1} in the $CH_3CHO···NH_3$ complex was determined at the high theory of level.[110]

Man *et al*. indicated that there are distinct tendencies toward a blue or red shift of the C_{sp3}-H stretching frequency in the C_{sp3}-H···N hydrogen bond in complexes formed by haloforms with NH_3 and its monohaloge nated derivatives (blue-shift: $\Delta\nu_{CH}$ = 7.0 ÷ 36.3 cm^{-1}; red-shift: $\Delta\nu_{CH}$ = -2.0 ÷ -92.6 cm^{-1}). In this work, Man's research reports that blue- or red shift tendency depends on the polarity of the C_{sp3}-H covalent bond and the proton affinity of the N site in the isolated monomers.[108] Significantly, Man *et al*. proposed using the DPE/PA ratio to predict the type of hydrogen bond following complexation. Accordingly, these authors suggested that the C-H···N hydrogen bonded interaction between a C-H bond and a proton acceptor at N atom with DPE/PA of over 2.0 is expected to form a blue-shifting hydrogen bonding, and a red-shifting hydrogen bond will be formed if this ratio is lower than 2.0. In many cases, for the same proton donor (methane and its derivatives), the gas phase basicity at the N site of the proton acceptor is proportional to an elongation of C_{sp3}-H bond length accompanied by a decrease of its stretching frequency upon binary complexation.

While the hydrogen-bonded complexes with the participation of C_{sp3}-H covalent bond show the blue-shift or in some above cases, a red shift of stretching vibration, the complexes with the C_{sp2}-H bond acting as a proton donor present the blue shift to a much larger extent although the polarity is lower for the C_{sp3}-H than for C_{sp2}-H covalent bond.[109] Indeed, the blue-shifted C_{sp2}-H···N hydrogen bonds were observed in the $CH_3CHO···NH_3$ complexes at the MP2/6-31G(d), MP2/6-311+G(d,p) and MP2/6-311++G(2d,2p) levels ($\Delta\nu_{CH}$ = 46÷71 cm^{-1}).[110] In the complexes of HCN with RCHO (R = H, Cl, Br, NH_2, CH_3), the C_{sp2}-H···N blue-shifting hydrogen bonds were detected, which were inversely proportional to its polarity in the RCHO monomer.[111] Similarly, a theoretical study at high level for stable structures of aldehydes RCHO (R = CH_3, NH_2, F, Cl, Br) and cyanides XCN (X = H, F) was investigated by Tri *et al*., which indicated the blue shift of C_{sp2}–H stretching frequency in the C_{sp2}–H···N hydrogen bond ($\Delta\nu_{CH}$ = 6.2÷41.9 cm^{-1}).[73] Tri *et al*. proposed that replacing one H atom in HCHO with an electron-donating group (CH_3, NH_2) enhances the C_{sp2}-H blue shift in the C_{sp2}-H···N bond, while having a slight effect on the blue shift of the C_{sp2}-H stretching vibration in the case of the halogenated complexes, as compared to that in HCHO···HCN complex and HCHO···FCN complex. This result was considered to depend on the polarity of C_{sp2}-H

https://doi.org/10.52111/qnjs.2023.17302

bond. It is also remarkable that the blue shift of C_{sp2}-H stretching vibration involved in the C_{sp2}-H···N hydrogen bond is generally weaker for RCHO···HCN complex than for RCHO···FCN complex, owing to the larger gas-phase Lewis basicity at the N site of HCN compared to FCN.

The weakly red shift in stretching vibration of C_{sp}-H bond was observed for C_{sp}-H···N hydrogen bond in the complex of acetylene and HSN at MP2/6-311++G(2d,2p) and MP2/aug-cc-pVTZ levels (Δr_{CH} = 1.7 Å; $\Delta\nu_{CH}$ = -12 cm^{-1}).[112] The obtained results at various levels of theory show the red shift of C_{sp}-H stretching frequency in C_{sp}-H···N hydrogen bond in the complex between acetylene (C_2H_2) and NH_3 ($\Delta\nu_{CH}$ = -170 cm^{-1}), which agrees well with experimental measurements ($\Delta\nu_{CH}$ = -97.3 cm^{-1}).[113] Additionally, the C_{sp}-H···N hydrogen-bonded complexes of NH_3 and CH_3NH_2 with several fluorine-substituted phenylacetylenes investigated by Dey *et al*. were characterized by a red shift in acetylenic C_{sp}-H stretching vibration ($\Delta\nu_{Csp\text{-}H}$ = -103 ÷ -157 cm^{-1}).[114] The obtained results in complexes of 3-fluorophenylacetylene and 2,6-difluorophenylacetylene with some Lewis bases such as ammonia, methylamine, dimethylamine and trimethylamine designate that the red-shifts of the acetylenic C–H stretching vibration in the C_{sp}-H···N hydrogen-bonded complexes rise as the Lewis gas phase basicity increases ($\Delta\nu_{CH}$ = -49 ÷ -219 cm^{-1}).[115] It can be seen that all C_{sp}-H covalent bonds as proton donors in the hydrogen bonds in the above-mentioned complexes are the typical red-shifted irrespective of proton acceptor.

3.3. C-H···π hydrogen bond

In 1999, Hobza *et al*. revealed the first experimental evidence for the blue-shifted hydrogen bond in the $CHCl_3$···C_6H_5F complexes using double-resonance IR ion-depletion spectroscopy ($\Delta\nu_{CH}$ = 14 cm^{-1}), which agrees with the ab initio calculation ($\Delta\nu_{CH}$ = 12 cm^{-1}).[90] The agreement of blue shift for both experimental result and theoretical investigation was later also detected in the complex of CHF_3 and fluorobenzene ($\Delta\nu$ = 12 cm^{-1}).[44] Some theoretical investigations into the complexes between proton donors (CH_4, CHF_3, $CHCl_3$, $CHBr_3$, CHI_3) and π-systems acting as proton acceptors (benzene, fluorobenzene, acetylene, and ethylene) proposed a contraction of the C_{sp3}-H bond length and an increase in its stretching frequency.[116-118] Weak C_{sp3}-H···π blue shifting hydrogen bond in C_2H_2···$CHCl_3$ ($\Delta\nu_{CH}$ = 20 cm^{-1}) and C_2H_2···CHF_3 ($\Delta\nu_{CH}$ = 23 cm^{-1}) complexes using matrix-isolation IR spectroscopy and ab initio computations were reported.[119,120] Ab initio investigations on the 1:1 and 1:2 complexes of C_2H_2 with CH_3Cl, CH_2Cl_2 and $CHCl_3$ also predicted a blue shift of the C_{sp3}-H stretching frequency.[121] Some complexes of benzene with proton donors (CH_4, $CHCl_3$) were studied with the contraction of the C_{sp3}-H bond (-0.0009÷-0.0023 Å) and the blue shift of its stretching frequency (15÷52 cm^{-1}).[17] The blue shifting hydrogen bond was detected in the complexes of 3-methylindole and $CHCl_3$/CHF_3 by 2 and 16 cm^{-1} in the cases of $CHCl_3$ and CHF_3, respectively.[49] Similarly, Shirhatti *et al*. suggested that for the complexes between p-cresol/p-cyanophenyl and CHX_3 (X = F, Cl) at MP2/aug-cc-pVDZ, the C_{sp3}-H stretching frequency in the C_{sp3}–H···π hydrogen bond was blue-shifted by 17.2÷65 cm^{-1}.[122] Reimann *et al*. observed the blue shift of the C_{sp3}-H stretching vibration in C_6H_5F···CHF_3 (21 cm^{-1}).[44] While all complexes of CHX_3 (X = H, F, Cl, Br) with benzene have the C_{sp3}-H blue-shifting stretching frequency of *ca.* 9÷50 cm^{-1}), it was observed that the CHX_3···C_6F_6 complexes all have small C_{sp3}-H···π blue-shifts of C_{sp3}-H stretching frequency and a slight contraction of C_{sp3}-H bond in CHX_3 ($\Delta\nu$ = 2÷27 cm^{-1}) at MP2/6-31G(d) level.[123] Notably, matrix isolation IR spectroscopy and ab initio computations were used to examine the blue-shifted hydrogen-bonded complexes of CHF_3 with benzene (C_6H_6) and acetylene (C_2H_2).[64] The red shift of supersonic jet expansion was found to be 55 cm^{-1}. When benzene was utilized as an acceptor, a slight blue shift of

https://doi.org/10.52111/qnjs.2023.17302

7.7 cm^{-1} and an insignificant red shift of 1.1 cm^{-1} were detected under supersonic jet expansion and liquid krypton at 119 K, respectively.[64] It can be seen that, the C_{sp3}-H···π hydrogen bond is weak and moderately blue-shifted.

For the C_{sp2}-H···π hydrogen bond, the blue-shifting intramolecular C_{sp2}-H···π bonds in conformer of 1,3-hexadien-5-yne and its halogen-substituted derivatives were observed at MP2/6-31G(d,p) level. In which, the polarization of the C_{sp2}-H bond is considered as one of the reasons for the stretching frequency blue shifting in the hydrogen bonds.[124] The complex of benzene with a strong proton donor (HCN) was examined with the elongation of the C_{sp}-H bond and the red shift of its stretching frequency (Δr_{CH} = 0.0017Å and $\Delta\nu_{CH}$ = -18 cm^{-1}).[17] Hydrogen-bonded complexes of acetylene and benzene with HCN, acetylene and trihalomethanes HCX_3 (X = F, Cl, Br) were investigated at MP2/6-311+G(2d,2p) and MP2/aug-cc-pVTZ levels.[112] The red-shift of C_{sp}-H stretching frequency was observed in complexes between acetylene/benzene with proton donors like HCN or acetylene, while with the C_{sp3}-H bond, HCF_3 is a weakly blue-shifting donor, $HCCl_3$ is much weaker, and $HCBr_3$ has no discernible red or blue shift. Our theoretical calculations at the MP2/aug-cc-pVDZ level suggested the C_{sp}–H red shift of 5.7÷24.9 cm^{-1} in the C_{sp}–H···π hydrogen bond for binary complexes of C_2HX (X = H, F, Cl, Br, CH_3, NH_2) with C_6H_6 and $B_3N_3H_6$.[125] As discussed above, from the computational and experimental results in the complexes, it is found that the C–H···π hydrogen bond with a sp3-hybridized C atom shows a larger magnitude of stretching frequency blue shift as compared to that of C_{sp2} atom, and the hydrogen bond involving the C_{sp2}-H bond tends to the red shifting.

4. CONCLUSION

Results on the characteristics of non-conventional hydrogen bonds involving the C-H covalent bond as a proton donor are summarized in this work. This review is hoped to contribute to a more thorough understanding of hydrogen bonding features, including changes in bond length and its corresponding stretching frequencies upon complexation, from a theoretical viewpoint. The non-conventional hydrogen bonds involving the $C_{sp3/sp2}$–H covalent bond in the $C_{sp3/sp2}$–H···O/S/Se/Te/N/π hydrogen bond show both red-shifting and blue-shifting of stretching frequency, however, the C_{sp}–H red shift is observed in most hydrogen-bonded complexes. It is proposed that the polarity of the proton donor and the gas phase basicity of the proton acceptor play a key role in the red- or blue-shift of the C-H stretching vibration. The results also demonstrate that the ratio of deprotonation enthalpy to proton affinity (DPE/PA) might be used to classify non-conventional hydrogen bonds as an indicator. For a clearer understanding on the nature of non-conventional hydrogen bonds, it should be suggested that we need focus on energetic components such as dispersion, induction, electrostatics, etc… to find out the trend of their different contributions for each kind of non-conventional hydrogen bond.

REFERENCES

1. J.-M. Lehn. *Supramolecular chemistry*, Weinheim: Verlag-Chemie, 1995.
2. R. E. Plata, D. E. Hill, B. E. Haines, D. G. Musaev, L. Chu, D. P. Hickey, M. S. Sigman, J-Q. Yu, D. G. Blackmond. A role for Pd(IV) in catalytic enantioselective C–H functionalization with monoprotected amino acid ligands under mild conditions, *Journal of the American Chemical Society*, **2017**, *139*, 9238-9245.
3. I. Kaplan. *Intermolecular interactions: Physical picture, computational methods and model potentials* (Wiley Series in Theoretical Chemistry), John Wiley, Chichester, 2006.
4. G. R. Desiraju, T. Steiner. *The weak hydrogen bond in structural chemistry and biology*, Oxford University Press Inc, New York, 1999.
5. S. J. Grabowski. *Hydrogen bonding – New insights*, Springer, New York, 2006.

https://doi.org/10.52111/qnjs.2023.17302

6. G. A. Jeffrey. *An introduction to hydrogen bonding*, Oxford University Press, New York, 1997.

7. S. Scheiner. The hydrogen bond: A hundred years and counting, *Journal of the Indian Institute of Science*, **2020**, *100*, 61-76.

8. E. D. Glowacki. M. Irimia-Vladu, S. Bauer, N. S. Sariciftci. Hydrogen-bonds in molecular solids – from biological systems to organic electronics, *Journal of Materials Chemistry B*, **2013**, *1*, 3742-3753.

9. G. R. Desiraju. Reflections on the hydrogen bond in crystal engineering, *Crystal Growth & Design*, **2011**, *11*, 896-898.

10. N. T. Bui, H. Kang, S. J. Teat, G. M. Su, C.-W. Pao, Y.-S. Liu, E.W. Zaia, J. Guo, J.-L. Chen, K. R. Meihaus, C. Dun, T. M. Mattox, J. R. Long, P. Fiske, R. Kostecki, J. J. Urban. A nature-inspired hydrogen-bonded supramolecular complex for selective copper ion removal from water, *Nature Communications*, **2020**, *11*, 1-12.

11. J. Dutta, A. K. Sahu, A. S. Bhadauria, H. S. Biswal. Carbon-centered hydrogen bonds in proteins, *Journal of Chemical Information and Modeling*, **2022**, *62*, 1998-2008.

12. J. Perlstein. The weak hydrogen bond in structural chemistry and biology, *Journal of the American Chemical Society*, **2001**, *123*, 191-192.

13. J. Dutta, D. K. Sahoo, S. Jena, K. D. Tulsiyan, H. S. Biswal. Non-covalent interactions with inverted carbon: a carbo-hydrogen bond or a new type of hydrogen bond?, *Physical Chemistry Chemical Physics*, **2020**, *22*, 8988-8997.

14. L. Pauling. The nature of the chemical bond. application of results obtained from the quantum mechanics and from a theory of paramagnetic susceptibility to the structure of molecules, *Journal of the American Chemical Society*, **1931**, *53*, 1367-1400.

15. I. V. Alabugin, M. Manoharan, S. Peabody, F. Weinhold. Electronic basis of improper hydrogen bonding: a subtle balance of hyperconjugation and rehybridization, *Journal of the American Chemical Society*, **2003**, *125*, 5973-5987.

16. G. Trudeau, J. M. Dumas, P. Dupuis, M. Guerin, C. Sandorfy. Intermolecular interactions and anesthesia: infrared spectroscopic studies, *Topics in Current Chemistry*, **1980**, *93*, 91-125.

17. P. Hobza, Z. Havlas. Blue-shifting hydrogen bonds, *Chemical Reviews*, **2000**, *100*, 4253-4264.

18. P. Hobza, V. Spirko. Why is the N1–H stretch vibration frequency of guanine shifted upon dimerization to the red and the amino N–H stretch vibration frequency to the blue?, *Physical Chemistry Chemical Physics*, **2003**, *5*, 1290-1294.

19. P. Hobza. The H-index unambiguously discriminates between hydrogen bonding and improper blue-shifting hydrogen bonding, *Physical Chemistry Chemical Physics*, **2001**, *3*, 2555-2556.

20. X. Li, L. Liu, H. B. Schlegel. On the physical origin of blue-shifted hydrogen bonds, *Journal of the American Chemical Society*, **2002**, *124*, 9639-9647.

21. Y. Gu, S. Scheiner. Fundamental properties of the CH···O interaction: Is it a true hydrogen bond?, *Journal of the American Chemical Society,* **1999**, *121*, 9411-9422.

22. A. Masunov, J. J. Dannenberg. C-H Bond-Shortening upon hydrogen bond formation: Influence of an electric field, *The Journal of Physical Chemistry A*, **2001**, *105*, 4737-4740.

23. W. Hermansson. Blue-shifting hydrogen bonds, *The Journal of Physical Chemistry A*, **2002**, *106*, 4695-4702.

24. A. K. Chandra, S. Parveen, T. Zeegers-Huyskens. Anomeric effects in the symmetrical and asymmetrical structures of triethylamine. Blue-shifts of the C−H stretching vibrations in complexed and protonated triethylamine, *The Journal of Physical Chemistry A*, **2007**, *111*, 8884-8891.

25. J. Joseph, E. D. Jemmis. Red-, Blue-, or No-shift in hydrogen bonds: A unified explanation, *Journal of the American Chemical Society*, **2007**, *129*, 4620-4632.

26. Y. Mo, C. Wang, L. Guan, B. Braıda, P. C. Hiberty, W. Wu. On the nature of blueshifting

hydrogen bonds, *Chemistry - A European Journal*, **2014**, *20*, 8444-8452.

27. X. Chang, Y. Zhang, X. Weng, P. Su, W. Wu, Y. Mo. Red-shifting versus blue-shifting hydrogen bonds: Perspective from Ab initio valence bond theory, *The Journal of Physical Chemistry A*, **2016**, *120*, 2749-2756.

28. Y. Mao, M. Head-Gordon. Probing blue-shifting hydrogen bonds with adiabatic energy decomposition analysis, *The Journal of Physical Chemistry Letters*, **2019**, *10*, 3899-3905.

29. C. Wang, D. Danovich, S. Shaik, Y. Mo. A unified theory for the blue- and red-shifting phenomena in hydrogen and halogen bonds, *Journal of Chemical Theory and Computation*, **2017**, *13*, 1626-1637.

30. H. Lodish, A. Berk, S. L. Zipursky, P. Matsudaira, D. Baltimore, J. Darnell. *Noncovalent bonds - molecular cell biology* (4th ed.), W.H. Freeman, New York, 2000.

31. G. A. Jeffrey, W. Saenger. *Hydrogen bonding in biological structures*, Springer-Verlag, Berlin, Germany, 1991.

32. P. Chakrabarti, U. Samanta. CH/pi interaction in the packing of the adenine ring in protein structures, *Journal of Molecular Biology*, **1995**, *251*, 9-14.

33. P. Gilli, G. Gilli. *The nature of the hydrogen bond*, Oxford University Press Inc, New York, 2009.

34. Y. Mandel-Gutfreund, H. Margalit, R. L. Jernigan, V. B. Zhurkin. A role for CH...O interactions in protein-DNA recognition, *Journal of Molecular Biology*, **1998**, *277*, 1129-1140.

35. J. D. Olivier, F. Marc, C. Enric. Activation of C−H···Halogen (Cl, Br, and I) Hydrogen bonds at the organic/inorganic interface in fluorinated tetrathiafulvalenes salts, *Chemistry - A European Journal*, **2001**, *7*, 2635-2643.

36. J. J. J. Dom, B. Michielsen, B. U. W. Maes, W. A. Herrebout, B. J. van der Veken. The C–H···π interaction in the halothane/ethene complex: A cryosolution infrared and Raman study, *Chemical Physics Letters*, **2009**, *469*, 85-89.

37. J. M. Hermida-Ramon, A. M. Grana. Blue-shifting hydrogen bond in the benzene–benzene and benzene–naphthalene complexes, *Journal of Computational Chemistry*, **2007**, *28*, 540-546.

38. C. D. Keefe, M. Isenor. Ab initio study of the interaction of CHX_3 (X = H, F, Cl, or Br) with benzene and hexafluorobenzene, *The Journal of Physical Chemistry A*, **2008**, *112*, 3127-3132.

39. B. J. van der Veken, W. A. Herrebout, R. Szostak, D. N. Shchepkin, Z. Havlas, P. Hobza. The nature of improper, blue-shifting hydrogen bonding verified experimentally, *Journal of the American Chemical Society*, **2001**, *123*, 12290-12293.

40. N. T. Trung, T. T. Hue. Blue- and red-shifting hydrogen bond in the complexes of $CHCl_3$ and NH_2X (X: H, F, Cl, Br, CH_3): An ab-initio quantum chemical study, *Quy Nhon University Journal of Science*, **2007**, *1*, 41-50.

41. T. T. Trung, P. D. C. Tu, H. Q. Dai, N. P. Hung, N. T. Trung. A theoretical study on interaction and stability of complexes between dimethyl sulfide and carbon dioxide, *Quy Nhon University Journal of Science*, **2019**, *13*, 95-105.

42. P. D. H. Nhung, H. T. Nam, N. T. Trung. An insight into improper hydrogen bond of C-H···N type in complexes of chloroform with hydrogen cyanide and its flouro derivative, *Quy Nhon University Journal of Science*, **2020**, *14*, 15-24.

43. P. T. Hoa, P. D. Cam-Tu, N. T. Trung. Effects of substitution on intermolecular interaction and stability of complexes of CO_2 and CH_3OCHX_2 (X = H, F, Cl, Br, CH_3), *Quy Nhon University Journal of Science*, **2019**, *13*, 75-83.

44. B. Reimann, K. Buchhold, S. Vaupel, B. Brutschy, Z. Havlas, V. Sÿpirko, P. Hobza. Improper, blue-shifting hydrogen bond between fluorobenzene and fluoroform, *The Journal of Physical Chemistry A*, **2001**, *105*, 5560-5566.

45. B. Reimann, K. Buchhold, S. Vaupel, B. Z. Brutschy. Blue-shift in the frequencies of the CH stretches of chloro- and fluoroform induced by C–H...π hydrogen bonding with benzene derivatives: the influence of electron donating and withdrawing substituents, *Journal of Physical Chemistry*, **2001**, *215*, 777-793.

https://doi.org/10.52111/qnjs.2023.17302

46. S. N. Delanoye, W. A. Herrebout, B. J. Van der Veken. Blue shifting hydrogen bonding in the complexes of chlorofluoro haloforms with Acetone-d6 and Oxirane-d4, *Journal of the American Chemical Society*, **2002**, *124*, 11854-11855.

47. W. A. Herrebout, S. N. Delanoye, B. U. W. Maes, B. J. Van der Veken. Infrared spectra of the complexes of trifluoroethene with dimethyl ether, acetone, and oxirane: A cryosolution study, *The Journal of Physical Chemistry A*, **2006**, *110*, 13759-13768.

48. B. Michielsen, W. A. Herrebout, B. Van der Veken. C-H bonds with a positive dipole gradient can form blue-shifting hydrogen bonds: The complex of halothane with methyl fluoride, *ChemPhysChem*, **2008**, *9*, 1693-1701.

49. P. R. Shirhatti, S. Wategaonkar. Blue shifted hydrogen bond in 3-methylindole·CHX_3 complexes (X = Cl, F), *Physical Chemistry Chemical Physics*, **2010**, *12*, 6650-6659.

50. P. R. Shirhatti, D. K. Maity, S. Wategaonkar. C–H···Y hydrogen bonds in the complexes of p-cresol and p-cyanophenol with fluoroform and chloroform, *The Journal of Physical Chemistry A*, **2013**, *117*, 2307-2316.

51. W. A. Herrebout, S. M. Melikova, S. N. Delanoye, K. S. Rutkowski, D. N. Shchepkin, B. J. van der Veken. A cryosolution infrared study of the complexes of fluoroform with ammonia and pyridine: Evidence for a C−H···N pseudo blue-shifting hydrogen bond, *The Journal of Physical Chemistry A*, **2005**, *109*, 3038-3044.

52. K. S. Rutkowski, S. M. Melikova, M. Rospenk, A. Koll. Strong and weak effects caused by non covalent interactions between chloroform and selected electron donor molecules, *Physical Chemistry Chemical Physics*, **2011**, *13*, 14223-14234.

53. R. Gopi, N. Ramanathan, K. Sundarajan. Experimental evidence for blue-shifted hydrogen bonding in the fluoroform–hydrogen chloride complex: A matrix-isolation infrared and ab initio study, *The Journal of Physical Chemistry A*, **2014**, *118*, 5529-5539.

54. M. Budesınsky, P. Fiedler, Z. Arnold. Triformylmethane: An efficient preparation, some derivatives and spectra, *Synthesis*, **1989**, *11*, 858-860.

55. R. Taylor, O. Kennard. Crystallographic evidence for the existence of C-H···O, C-H···N, and C-H···Cl hydrogen bonds, *Journal of the American Chemical Society*, **1982**, *104*, 5063-5070.

56. I. E. Boldeskul, I. F. Tsymbal, E. V. Ryltsev, Z. Larajka, A. J. Barnes. Reversal of the usual ν(C-H/D) spectral shift of haloforms in some hydrogen-bonded complexes, *Journal of Molecular Structure*, **1997**, *436*, 167-171.

57. R. H. Craptree, A. Lei. Introduction: CH activation, *Chemical Reviews*, **2017**, *117*, 8481-8482.

58. V. C. C. Wang, S. Maji, P. P. Y. Chen, H. K. Lee, S. S. F. Yu, S. Y. Chan. Alkane oxidation: methane monooxygenases, related enzymes, and their biomimetics, *Chemical Reviews*, **2017**, *117*, 8574-8621.

59. B. Yang, J. F. Cui, M. K. Wong. Selective C–H bond hydroxylation of cyclohexanes in water by supramolecular control, *RSC Advances*, **2017**, *7*, 30886-30893.

60. L. S. Sremaniak, J. L. Whitten, M. J. Truitt, J. L. White. Weak hydrogen bonding can initiate alkane C−H bond activation in acidic zeolites, *The Journal of Physical Chemistry B*, **2006**, *110*, 20762-20764.

61. M. Hippler, S. Hesse, M. A. Suhm. Quantum-chemical study and FTIR jet spectroscopy of $CHCl_3$–NH_3 association in the gas phase, *Physical Chemistry Chemical Physics*, **2010**, *12*, 13555-13565.

62. P. R. Shirhatti, D. K. Maity, S. Bhattacharyya, S. Wategaonkar. C-H···N hydrogen-bonding interaction in 7-azaindole: CHX_3 (X = F, Cl) complexes, *ChemPhysChem*, **2014**, *15*, 109-117.

63. M. W. Hnat, H. Ratajczak. Matrix isolation infrared studies of trichloromethane-base complexes, *Journal of Molecular Structure*, **1988**, *177*, 487-493.

64. R. Gopi, N. Ramanathan, K. Sundararajan. Experimental evidence for the blue-shifted

hydrogen-bonded complexes of CHF_3 with π-electron donors, *Spectrochimica Acta Part A*, **2017**, *181*, 137-147.

65. K. S. Rutkowski, A. Karpfen, S. M. Melikova, W. A. Herrebout, A. Koll, P. Wolschann, B. J. van der Veken. Cryospectroscopic and ab initio studies of haloform–trimethylamine H-bonded complexes, *Physical Chemistry Chemical Physics*, **2009**, *11*, 1551-1563.

66. S. N. Delanoye, W. A. Herrebout, B. J. van der Veken. Stabilities of the C−H···O bonded complexes of the haloforms $HCCl_nF_{3-n}$ (n = 0−3) with dimethyl ether, oxirane, and acetone: An experimental and theoretical study, *The Journal of Physical Chemistry A*, **2005**, *109*, 9836-9843.

67. M. Hippler. Quantum chemical study and infrared spectroscopy of hydrogen-bonded $CHCl_3$–NH_3 in the gas phase, *The Journal of Chemical Physics*, **2007**, *127*, 084306(1-10).

68. K. S. Rutkowski, S. M. Melikova, R. E. Asfin, B. CzarnikMatusewicz, M. Rospenk. The gas phase FTIR studies of chloroform + B and halothane + B (B = TMA, FCD3) mixtures, *Journal of Molecular Structure*, **2014**, *1072*, 32-37.

69. B. Behera, P. K. Das. Blue- and red-shifting hydrogen bonding: A gas phase FTIR and Ab initio study of RR′CO···$DCCl_3$ and RR′S···$DCCl_3$ complexes, *The Journal of Physical Chemistry A*, **2018**, *122*, 4481-4489.

70. A. K. Chandra, T. Zeegers-Huyskens. Theoretical investigation of the cooperativity in $CH_3CHO{\cdot}2H_2O$, $CH_2FCHO{\cdot}2H_2O$, and $CH_3CFO{\cdot}2H_2O$ systems, *Journal of Atomic and Molecular Physics*, **2012**, *2*, 1-8.

71. N. T. Trung, N. P. Khanh, A. J. P. Carvalho, M. T. Nguyen. Remarkable shifts of C_{sp2}-H and O-H stretching frequencies and stability of complexes of formic acid with formaldehydes and thioformaldehydes, *Journal of Computational Chemistry*, **2019**, *40*, 1387-1400.

72. N. T. Trung, N. T. T. Trang, V. T. Ngan, D. T. Quang, M. T. Nguyen. Complexes of carbon dioxide with dihalogenated ethylenes: Structure, stability and interaction, *RSC Advances*, **2016**, *6*, 31401-31409.

73. N. N. Tri, N. T. H. Man, N. L. Tuan, N. T. T. Trang, D. T. Quang, N. T. Trung. Structure, stability and interactions in the complexes of carbonyls with cyanides, *Theoretical Chemistry Accounts*, **2017**, *136*, 1-12.

74. M. J. Frisch, G. W. Trucks, H. B. Schlegel, G. E. Scuseria, M. A. Robb, J. R. Cheeseman, J. A. Pople. *Gaussian 09 (Revision B.01)*, Gaussian Inc, Wallingford, 2009.

75. T. A. Keith, T. K. Gristmill. *AIMAll (Version 19.10.12) Software*, Overland Park KS, USA, 2019.

76. E. D. Glendening, J. Badenhoop, K. A. E. Reed, J. E. Carpenter, J. A. Bohmann, C. M. Morales, F. Weinhold. *GenNBO 5.G*, Theoretical Chemistry Institute, University of Wisconsin, Madison, 2001.

77. J. M. Turney, A. C. Simmonett, R. M. Parrish, E. G. Hohenstein, F. A. Evangelista, J. T. Fermann, B. J. Mintz, L. A. Burns, J. J. Wilke, M. L. Abrams, N. J. Russ, M. L. Leininger, C. L. Janssen, E. T. Seidl, Q. D. Allen, H. F. Schaefer, R. A. King, E. F. Valeev, C. D. Sherrill, T. D. Crawford. WIREs, *Computational Molecular Science*, **2012**, *2*, 556-565.

78. R. Bukowski, W. Cencek, M. Jeziorska, B. Jeziorski, V. F. Lotrich, A. J. Misquitta, R. Moszyński, K. Patkowski, R. Podeszwa, F. Rob, S. Rybak, K. Szalewicz, R. J. Wheatley, E.S. Paul, P. E. S. Wormer, P. S. Żuchowski. *SAPT2012.2,* Warsaw, Poland, 2013.

79. J. Contreras-García, E. R. Johnson, S. Keinan, R. Chaudret, J.-P. Piquemal, D. N. Beratan, W. Yang. NCIPLOT: a program for plotting noncovalent interaction regions, *Journal of Chemical Theory and Computation*, **2011**, *7*, 625-632.

80. W. Humphrey, A. Dalke, K. Schulten. VMD: visual molecular dynamics, *Journal of Molecular Graphics*, **1996**, *14*, 33-38.

81. T. Williams, C. Kelley, H.-B. Broeker, J. Campbell, R. Cunningham, D. Denholm, G. Elber, R. Fearick, C. Grammes, L. Hart, L. Hecking, P. Juhász, T. Koenig, D. Kotz, E. Kubaitis, R. Lang, T. Lecomte,

https://doi.org/10.52111/qnjs.2023.17302

A. Lehmann, A. Mai, B. Märkisch, T. Matsuoka, E. A. Merritt, P. Mikulík, C. Steger, S. Takeno, T. Tkacik, J. Van der Woude, J. R. V. Zandt, A. Woo, J. Zellner. *Gnuplot 5.5: An interactive plotting program*, 2021.

82. T. Lu, F. Chen. Multiwfn: A multifunctional wavefunction analyzer, *Journal of Computational Chemistry*, **2012**, *33*, 580-592.

83. G. R. Desiraju. The C-H···O hydrogen bond in crystals: what is it?, *Accounts of Chemical Research*, **1991**, *24*, 290-296.

84. P. Chopra, & S. Chakraborty. Computational study of red- and blue-shifted C-H···Se hydrogen bond in Q_3C-H···SeH_2 (Q = Cl, F, H) complexes, *Chemical Physics*, **2018**, *500*, 54-61.

85. F. Ito. Matrix-isolation infrared studies of 1:1 molecular complexes containing chloroform ($CHCl_3$) and Lewis bases: Seamless transition from blue-shifted to red-shifted hydrogen bonds, *The Journal of Chemical Physics*, **2012**, *137*, 014505(1-8).

86. B. Behera, P. K. Das. Blue-shifted hydrogen bonding in the gas phase CH/D_3CN···$HCCl_3$ complexes, *The Journal of Physical Chemistry A*, **2019**, *123*, 1830-1839.

87. A. Mukhopadhyay, M. Mukherjee, P. Pandey, A. K. Samanta, B. Bandyopadhyay, T. Chakraborty. Blue shifting C−H···O hydrogen bonded complexes between chloroform and small cyclic ketones: Ring-size effects on stability and spectral shifts, *The Journal of Physical Chemistry A*, **2009**, *113*, 3078-3087.

88. R. Gopi, N. Ramanathan, N. Sundararajan. Blue-shift of the C-H stretching vibration in CHF_3-H_2O complex: Matrix isolation infrared spectroscopy and ab initio computations, *Chemical Physics*, **2016**, *476*, 36-45.

89. D. Pal, A. Chakraborty, S. Chakraborty. Investigation of [$CHCl_3$-CH_3OH] complex using matrix-isolation IR spectroscopy and quantum chemical calculation: Evidence of hydrogen- and halogen-bonding interaction, *Chemical Physics*, **2022**, *555*, 1114510-1114519.

90. P. Hobza, V. Spirko, Z. Havlas, K. Buchhold, B. Reimann, H. D. Barth, B. Krutschy. Anti-hydrogen bond between chloroform and fluorobenzene, *Chemical Physics Letters*, **1999**, *299*, 180-186.

91. A. Masunov, J. J. Dannenberg, R. H. Contreras. C-H Bond-shortening upon hydrogen bond formation: Influence of an electric field, *The Journal of Physical Chemistry A*, **2001**, *105*, 4737-4740.

92. B. Michielsen, C. Verlackt, B. J. van der Veken, & W. A. Herrebout. C–H···X (X = S, P) hydrogen bonding: The complexes of halothane with dimethyl sulfide and trimethylphosphine, *Journal of Molecular Structure*, **2012**, *1023*, 90-95.

93. Y. Liu, W.-Q. Liu, H.-Y. Li, Y. Yang, & S. Cheng. Hydrogen bonding interaction of formic acid-, formaldehyde-, formylfluoride-nitrosyl hydride: Theoretical study on the geometries, interaction energies and blue- or red-shifted hydrogen bonds, *Chinese Journal of Chemistry*, **2007**, *25*, 44-52.

94. S. Scheiner, T. Kar, & J. Pattanayak. Comparison of various types of hydrogen bonds involving aromatic amino acids, *Journal of the American Chemical Society*, **2002**, *124*, 13257-13264.

95. Y. Yang, W. Zhang, & X. Gao. Blue-shifted and red-shifted hydrogen bonds: Theoretical study of the CH_3CHO···HNO complexes, *International Journal of Quantum Chemistry*, **2006**, *106*, 1199-1207.

96. N. T. Trung, N. P. Hung, T. T. Hue, & M. T. Nguyen. Existence of both blue-shifting hydrogen bond and Lewis acid–base interaction in the complexes of carbonyls and thiocarbonyls with carbon dioxide, *Physical Chemistry Chemical Physics*, **2011**, *13*, 14033-14042.

97. A. Karpfen, & E. S. Kryachko. Blue-shifted A−H stretching modes and cooperative hydrogen bonding. 1. complexes of substituted formaldehyde with cyclic hydrogen fluoride and water clusters, *The Journal of Physical Chemistry A*, **2007**, *111*, 8177-8187.

98. N. T. T. Cuc, P. D. Cam-Tu, N. T. A. Nhung, N. M. Tho, N. T. Trung, V. T. Ngan. Theoretical aspects of nonconventional hydrogen bonds

in the complexes of aldehydes and hydrogen chalcogenides, *The Journal of Physical Chemistry A*, **2021**, *125*, 10291-10302.

99. N. T. T. Cuc, N. T. An, V. T. Ngan, A. K. Chandra, N. T. Trung. Importance of water and intramolecular interaction governs substantial blue shift of C_{sp^2}–H stretching frequency in complexes between chalcogenoaldehydes and water, *RSC Advances*, **2022**, *12*, 1998-2008.

100. N.T. An, N.T. Duong, N.N. Tri, N.T. Trung. Role of O–H···O/S conventional hydrogen bonds in considerable C_{sp^2}–H blue-shift in the binary systems of acetaldehyde and thioacetaldehyde with substituted carboxylic and thiocarboxylic acids, *RSC Advances*, **2022**, *12*, 35309-35319.

101. Y. Liu, W. Liu, Y. Yang, & J. Liu. Theoretical study of the red- and blue-shifted hydrogen bonds of nitroxyl and acetylene dimers, *International Journal of Quantum Chemistry*, **2006**, *106*, 2122-2128.

102. J. Andersen, J. Heimdal, B. Nelander, & R. Wugt Larsen. Competition between weak OH···π and CH···O hydrogen bonds: THz spectroscopy of the C_2H_2-H_2O and C_2H_4-H_2O complexes, *The Journal of Chemical Physics*, **2017**, 146, 194302(1-10).

103. J. M. Fan, L. Liu, Q. X. Guo. Substituent effects on the blue-shifted hydrogen bonds, *Chemical Physics Letters*, **2002**, 365, 464-472.

104. Y. Gu, T. Kar, & S. Scheiner. Comparison of the CH···N and CH···O interactions involving substituted alkanes, *Journal of Molecular Structure*, **2000**, *552*, 17-31.

105. N. T. Trung, T. T. Hue, & M. T. Nguyen. Interaction of CHX_3 (X = F, Cl, Br) with HNO induces remarkable blue shifts of both C–H and N–H bonds, *Physical Chemistry Chemical Physics*, **2009**, *11*, 926-933.

106. S. L. Paulson, A. J. Barnes. Trihalogenomethane - base complexes studied by vibrational spectroscopy in low-temperature matrices, *Journal of Molecular Structure*, **1982**, *80*, 151-158.

107. B. Michielsen, J. J. J. Dom, B. J. van der Veken, S. Hesse, M. A. Suhm, W. A. Herrebout. Solute–solvent interactions in cryosolutions: a study of halothane–ammonia complexes, *Physical Chemistry Chemical Physics*, **2012**, *14*, 6469-6478.

108. N. T. H. Man, P. L. Nhan, V. Vien, D. T. Quang, N. T. Trung. An insight into C-H···N hydrogen bond and stability of the complexes formed by trihalomethanes with ammonia and its monohalogenated derivatives, *International Journal of Quantum Chemistry*, **2017**, *117*, 1-8.

109. M. Domagała, & S. J. Grabowski. CH···N and CH···S hydrogen bonds influence of hybridization on their strength, *The Journal of Physical Chemistry A*, **2005**, *109*, 5683-5688.

110. Y. Yang, W. Zhang, S. Pei, J. Shao, W. Huang, & X. Gao. Blue-shifted and red-shifted hydrogen bonds: Theoretical study of the CH_3CHO···NH_3 complexes, *Journal of Molecular Structure: THEOCHEM*, **2005**, *732*, 33-37.

111. N. N. Tri, P. T. Minh Tam, N. T. Hong Man, H. Q. Dai, N. P. Hung, & N. T. Trung. Interactions of formaldehyde and its substituted derivatives with HCN: Structure, stability and interaction, *Vietnam Journal of Chemistry*, **2016**, *54*, 448-453.

112. P. Jantimapornkij, P. Jundee, N. Uttamapinant, S. Pianwanit, & A. Karpfen. A single bond H···π hydrogen bonding to acetylene and benzene: The role of intramolecular coupling, *Computational and Theoretical Chemistry*, **2012**, *999*, 231-238.

113. A. C. Thakur, R. C. Remsing. Molecular structure, dynamics, and vibrational spectroscopy of the acetylene: ammonia (1:1) plastic co-crystal at titan conditions, *Chemical Physics*, **2022**.

114. A. Dey, S. I. Mondal, S. Sen, & G. N. Patwari. Spectroscopic and Ab initio investigation of C−H···N hydrogen-bonded complexes of fluorophenylacetylenes: Frequency shifts and correlations, *ChemPhysChem*, **2016**, *17*, 2509-2515.

115. A. Dey, S. I. Mondal, S. Sen, D. Ghosh, & G. N. Patwari. Electrostatics determine vibrational frequency shifts in hydrogen bonded complexes, *Physical Chemistry Chemical Physics*, **2014**, *16*, 25247-25250.

https://doi.org/10.52111/qnjs.2023.17302

116. B. G. Oliveira, R. C. M. U. de Araújo, M. N. Ramos. A theoretical study of blue-shifting hydrogen bonds in π weakly bound complexes, *Journal of Molecular Structure: THEOCHEM*, **2009**, *908*, 79-83.

117. B. Reimann, K. Buchfold, S. Vaupel, B. Brutschy, Z. Havlas, V. Spirko, P. Hobza. Improper, blue-shifting hydrogen bond between fluorobenzene and fluoroform, *The Journal of Physical Chemistry A*, **2001**, *105*, 5560-5566.

118. P. Hobza, Z. Havlas. The fluoroform···ethylene oxide complex exhibits a C–H···O anti-hydrogen bond, *Chemical Physics Letters*, **1999**, *303*, 447-452.

119. E. Jemmis, K. Giju, K. Sundararajan, K. Sankaran, V. Vidya, K. Viswanathan, & J. J. Leszczynski. An ab initio and matrix isolation infrared study of the 1:1 C_2H_2–$CHCl_3$ adduct, *Journal of Molecular Structure*, **1999**, *510*, 59-68.

120. K. Sundararajan, N. Ramanathan, K. S. Viswanathan, K. Vidya, E. D. Jemmis. Complexes of acetylene–fluoroform: A matrix isolation and computational study, *Journal of Molecular Structure*, **2013**, *1049*, 69-77.

121. E. D. Jemmis, G. Subramanian, A. Nowek, R. W. Gora, R. H. Sullivan, J. Leszczynski. C–H···π interactions involving acetylene: An ab initio MO study, *Journal of Molecular Structure*, **2000**, *556*, 315-320.

122. P. R. Shirhatti, & S. Wategaonkar. C–H···p interactions involving acetylene: An ab initio MO study, *Physical Chemistry Chemical Physics*, **2010**, *12*, 6650-6659.

123. C. D. Keefe, M. Isenor. Ab Initio study of the interaction of CHX_3 (X = H, F, Cl, or Br) with benzene and hexafluorobenzene, *The Journal of Physical Chemistry A*, **2008**, *112*, 3127-3132.

124. L. Zhang, & D. Li. An insight into intramolecular blue-shifting C-H···π hydrogen bonds in 1,3-hexadien-5-yne and its halogen-substituted derivatives, *Chemical Physics*, **2018**, *518*, 58-68.

125. P. N. Khanh, V. T. Ngan, N. T. H. Man, N. T. A. Nhung, A. K. Chandra, N. T. Trung. An insight into C_{sp}–H···π hydrogen bonds and stability of complexes formed by acetylene and its substituted derivatives with benzene and borazine, *RSC Advances*, **2016**, *6*, 106662-106670.

126. Y. Liu, N. Li, C. Du, Y, Wang, K. He, H. Zheng, Z. Xue, Q. Chen, X. Li. Various hydrogen bonds make different fates of pharmaceutical contaminants on oxygen-rich nanomaterials, *Environmental Pollution*, **2023**, *316*, 120572.

127. J. Zhang, H. Zheng, X. Li, N. Li, Y. Liu, T. Li, Y. Wang, B. Xing. Direct spectroscopic evidence for charge-assisted hydrogen-bond formation between ionizable organic chemicals and carbonaceous materials, *Environmental Science & Technology*, **2022**, *56*, 9356-9366.

128. P. Wang, D. Zhang, H. Tang, H. Li, B. Pan. New insights on the understanding of the high adsorption of bisphenol compounds on reduced graphene oxide at high pH values via charge assisted hydrogen bond, *Journal of Hazardous Materials*, **2019**, *371*, 513-520.

129. P. Saranya, S. Kulik, B. Rehl, S. Roke. Charge transfer across C–H···O hydrogen bonds stabilizes oil droplets in water, *Science*, **2021**, *374*, 1366-1370.

130. B. Yang, L. Xing, S. Wang, C. Sun, Z. Men. Roles of hydrogen bonding interactions and hydrophobic effects on enhanced water structure strength in aqueous alcohol solutions, *Physics of Fluids*, **2023**, *35*, 034701.

TẠP CHÍ KHOA HỌC
TRƯỜNG ĐẠI HỌC QUY NHƠN

Hoạt tính xúc tác quang phân hủy methylene blue bằng vật liệu nano bán dẫn ZnO pha tạp Eu và Mn: Một nghiên cứu so sánh

Nguyễn Thị Khả Vân[1], Imee Saladaga Padillo[2], Đinh Kha Lil[3,*]

[1]Trung tâm GDNN – GDTX quận Ninh Kiều, Việt Nam
[2]Khoa Công Nghệ, Đại học bang Eastern Visayas, Phi-líp-pin
[3]Khoa Khoa học Tự nhiên, Trường Đại học Cần Thơ, Việt Nam

Ngày nhận bài: 14/11/2022; Ngày nhận đăng: 31/01/2023; Ngày xuất bản: 28/06/2023

TÓM TẮT

Nghiên cứu này được thực hiện nhằm tổng hợp vật liệu nano ZnO pha tạp Eu và Mn có tính chất quang học thích hợp cho ứng dụng quang xúc tác. Vật liệu nano ZnO với 1%, 5% và 10% mol kim loại pha tạp được điều chế bằng phương pháp thủy nhiệt. Các đặc tính cấu trúc, hình thái, quang học và từ tính của các hạt nano chuẩn bị được nghiên cứu bằng cách sử dụng nhiễu xạ tia X (X-ray diffraction - XRD), kính hiển vi điện tử quét (scanning electron microscope - SEM) và quang phổ phân tán năng lượng tia X (energy dispersion spectroscopy - EDS). Kết quả cho thấy các hạt nano ZnO pha tạp Eu và ZnO pha tạp Mn có cấu trúc wurtzite lục giác. Hoạt tính của các chất xúc tác quang đã tổng hợp được đánh giá dựa trên sự phân hủy quang của methylene blue (MB) dưới sự chiếu xạ tia UV. Vật liệu ZnO pha tạp 5% mol Eu và vật liệu ZnO pha tạp 1% mol Mn cho thấy hoạt tính quang xúc tác tốt nhất. Phản ứng phân hủy MB tuân theo quy luật động học của phản ứng bậc nhất. Vật liệu ZnO pha tạp kim loại tổng hợp rất dễ phục hồi và có khả năng tái sử dụng cao.

Từ khóa: *Tổng hợp ZnO cấu trúc nano, ZnO pha tạp kim loại, phương pháp thủy luyện, tính chất quang.*

**Tác giả liên hệ chính.*
Email: lildk93@gmail.com

QUY NHON UNIVERSITY
JOURNAL OF SCIENCE

Photocatalytic decomposition of methylene blue using Eu- and Mn-doped ZnO semiconductor nanomaterials: A comparative study

Kha-Van Nguyen-Thi[1], Padillo Imee Saladaga[2], Kha Lil Dinh[3,*]

[1]Center for Vocational Education - Secondary Education, Ninh Kieu District, Vietnam
[2]College of Engineering, Eastern Visayas State University, Philippines
[3]College of Natural Sciences, Can Tho University, Vietnam

Received: 14/11/2023; Accepted: 31/01/2023; Published: 28/06/2023

ABSTRACT

This study was carried out to synthesize Eu- and Mn-doped ZnO nanomaterials with optical properties suitable for catalytic applications. ZnO nanomaterials with 1%, 5%, and 10% mol of dopant were prepared using hydrothermal method. The structural, morphological, optical, and magnetic properties of the as-prepared nanoparticles were investigated using X-ray diffraction (XRD), scanning electron microscope (SEM), and X-ray energy dispersion spectroscopy (EDS). The results showed that the Eu-doped ZnO and Mn-doped ZnO nanoparticles exhibited a hexagonal wurtzite structure. The activity of the prepared photocatalysts was evaluated based on the photodegradation of methylene blue (MB) under ultraviolet light UV. ZnO materials doped with 5% mol Eu and ZnO materials doped with 1% mol Mn showed the best photocatalytic activity. Furthermore, the MB photodegradation reaction was observed to follow a first-order reaction. Finally, synthesized metal-doped ZnO materials are easy to recover and highly reusable.

Keywords: *Synthesis ZnO nanostructures, Metal-doped ZnO, hydrothermal method, optical properties.*

1. INTRODUCTION

In recent years, surface water and groundwater pollution has increased due to population growth and industrial development.[1] The primary sources of environmental pollution are organic dyes used in the food and textile industries due to their high toxicity and non-biodegradability, which has a carcinogenic effect on humans.[2,3] Methylene blue (MB) dyes are used by various industries, for example, as dyes in silk; as a food additive; and as dyeing of wool, leather, cotton, jute, and paper.[4,5] Methylene blue dyes have potent effects on the immune and reproductive systems and have potential carcinogenic and genotoxic effects.[6,7] Therefore, these harmful dyes must be removed from industrial wastewater. Several methods, such as biological treatment,[8,9] adsorption,[10] and photocatalysis,[11,12] have been used to remove these dyes from industrial wastewater. The use of photocatalysts to reduce organic compounds or convert them into harmless chemicals has been extensively studied to reduce the damage caused by organic dye pollution to the environment and to humans.[13] Semiconductor oxides, such as TiO_2, ZnO,

**Corresponding author.*
Email: lildk93@gmail.com

https://doi.org/10.52111/qnjs.2023.17303

SnO_2, WO_2, and CeO_2, are abundant in nature and widely used as a photochemical catalysts, especially for heterogeneous processes.[14,15] Among them, ZnO oxide is considered to be a promising catalyst in the decomposition of organic pigments as well as water disinfection. The most significant advantage of ZnO over TiO_2 is that it absorbs a larger range of the ultraviolet (UV) spectrum and has a corresponding threshold of 425 nm. Upon illumination, valence band electrons are promoted to the conduction band leaving a hole behind. These electron–hole pairs can either recombine or interact separately with other molecules. The holes at the ZnO valence band can oxidize the adsorbed water molecules or hydroxide ions to produce hydroxyl radicals. Electrons in the conduction band on the catalyst surface can reduce molecular oxygen to superoxide anion. This radical may form organic peroxides or hydrogen peroxide in the presence of organic scavengers.[16] ZnO is also one of the dominant materials used for nanotechnology. With controlled and material-dependent properties such as chemical, structural, electrical, thermal, and surface properties that can be varied depending on shape size, it has a wide range of applications.[17-18] ZnO's structure, a sizeable band gap energy (3.37 eV), the large exciton binding energy (60 meV), size, and thermal stability make it suitable for a broader range of devices.[19,20] To expand the application scope of ZnO, it is necessary to change the nanostructures' electron properties, narrow the band gap energy, and reduce the rate of photogenerated electrons and holes recombination. Metal or nonmetal doping into ZnO network is one of the effective methods to increase the activity of ZnO,[21,22] In recent years, much effort has been made to prepare metal doped ZnO materials, and various methods such as sol–gel, micro-emulsion, hydrothermal, spray pyrolysis, solid-reaction, radio frequency reactive magnetron sputtering, and electrodeposition have been employed. It is reported that the surface defects, serving as energy traps, may play a key role in the process of energy transfer. Compared with other approaches, hydrothermal method is regarded as an attractive candidate for the synthesis of metal doped ZnO due to its simplicity, easy-control, low-cost, and especially the presence of a large amount of surface defects. In this paper, Mn- and Eu-doped ZnO nanopowders were prepared with different metal concentration (1, 5 and 10% wt.) using solid state reaction. The obtained product was investigated by various advanced analytical techniques. The obtained composite was tested for photocatalytic applications on in water under UV light.

2. MATERIALS AND METHODS

2.1. Nanostructures synthesis

The Mn- and Eu-doped ZnO photocatalysts were synthesized using the hydrothermal method. $ZnCl_2$ was dissolved in deionized water and stirred using a magnetic stirrer for 30 minutes. With constant stirring, the doped metal ion solution was added to the solution, and stirring was continued for 30 minutes. The mixture's pH was adjusted to pH = 10 using 1M NaOH, and the stirring was continued for one more hour. The entire mixture was transferred to a thermos Teflon flask and allowed to stabilize in the oven at 190°C for 20 hours. After the reaction time, the resulting solution was centrifuged at 5500 rpm, and the solids were washed three times with deionized water and three times with alcohol to separate them from the solution. The desired product was obtained after drying the solids at 100°C for 20 hours.

2.2. Characterization techniques

X-ray diffraction (XRD) measurements were obtained using a diffractometer X-ray on the Bruker D8 Advance device (Germany) with a wavelength of λ = 1.5406Å. The extension of the diffraction test peak can provide information about the average crystal size through Scherrer's equation (1):[23]

$$D = \frac{0,9\lambda}{\Delta(2\theta)\cos\theta} \quad (1)$$

Where D is the average crystal size and Δ(2θ) is the full width at half maximum (FWHM).

The metal distribution in the materials was characterized using a scanning electron microscope field emission scanning (SEM, Hitachi X650) equipped with an energy dispersion X-ray system (EDS).

2.3. Photocatalysis experiments

The photocatalytic activities of synthetic materials were assessed based on the photocatalytic degradation reaction of MB. The remaining MB concentration over time of the photocatalytic reaction was determined on the UV-VIS Spectrophotometer Optima SP-3000 (Japan). A 20 W UV lamp was used as the light source for the photochemical reaction.

2.3.1. Establishment of a standard curve to investigate the linear range of the MB solution

MB solutions with a concentration of 100 mg/L were prepared and then diluted into the corresponding concentrations: 0.1, 0.5, 1.0, 1.5, 2.0, 4.0, 6.0, 8.0, 10.0, 12.0, 14.0, 16.0, 18.0, 20.0, 22.0, and 24.0 mg/L. UV-VIS spectroscopy was conducted with wavelengths ranging from 200 to 800 nm. Finally, the maximum absorption wavelength and linear range were determined, and the standard line of the MB solution was plotted.

2.3.2. Photocatalytic experiments

The adsorption of the dye to the surface of the catalyst is well known depending on the pH of the solution used.[24] Faouzi Achouri et al. showed that the catalytic activity was high for the doped ZnO materials at pH = 9.[25] A certain amount of synthetic material was added to 100 mL of the MB solution of pre-determined concentration, and then the pH was adjusted to pH = 9 using a 1M NaOH solution. The reaction mixture was stirred in the dark using a magnetic stirrer until the adsorption equilibrium was reached. 5 mL of the reaction mixture was centrifuged to separate the solids, and the optical density was measured (time t = 0, optical density A_o). Then the solution was stirred constantly and irradiated using a 20W UV bulb placed about 20 cm from the solution's surface. Every 30 minutes, 5 mL of the sample solution was taken and centrifuged to obtain the catalytic powder, and the optical density (A_t) was measured. This investigation was carried out for 270 minutes.

The decomposition efficiency of MB was calculated using equation (2):

$$H = \frac{C_o - C_t}{C_o} \times 100 = \frac{A_o - A_t}{A_o} \times 100 \quad (2)$$

Where C_o is the initial concentration of MB and C_t is the concentration of MB at different irradiation times.

3. RESULTS AND DISCUSSION

3.1. The Eu-doped ZnO characteristics

3.1.1. Effect of the amount of Eu dopant

The XRD results (Figure 1a) show that the high-intensity diffraction peaks correspond to the network plane families (100), (002), (101), and diffraction peaks with lower intensity, respectively. Lattice plane (102), (110), (103), (200), (112), (201), this result is consistent with JCPDS Card No. 77-0452 of the characteristic of the ZnO lattice has a Wurtzite hexagonal structure.[26] The position of the (100) peak was slightly shifted toward the lower angles, indicating the substitution of Eu^{3+} in the ZnO lattice (Figure 1b).[27] As shown, the weakness of their full width at half maximum may indicate an improvement in the crystallinity of ZnO. Thus, the peak is shifted towards the lower angle side.[28]

Figure 1a shows that when the molar ratio of doped Eu is less than 5%, the resulting XRD pattern has a monophasic hexagonal ZnO structure. However, when the molar ratio of Eu is doped more than 5%, in addition to the hexagonal phase of ZnO, there is also a cubic Eu_2O_3 phase corresponding to the JCPDS Card No. 43-1008 tag of Eu_2O_3. The formation of the Eu_2O_3 phase when increasing the content of doped Eu can be explained because zinc ions and Eu ions have different charges, and their difference in radius is quite large (Eu^{3+}: 0.95 Å; Zn^{2+}: 0.74 Å).[29]

https://doi.org/10.52111/qnjs.2023.17303

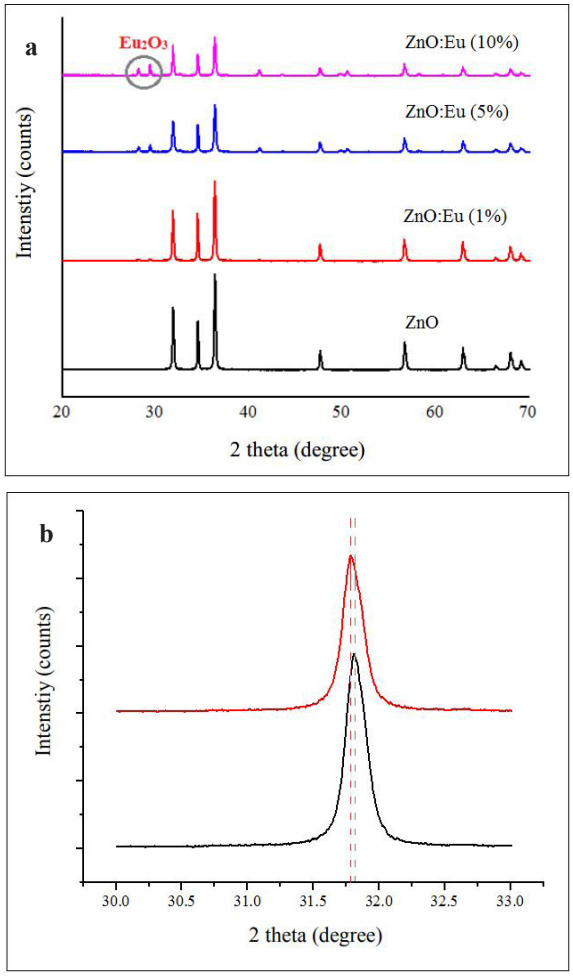

Figure 1. (a) The XRD patterns for Eu-doped ZnO with different doped Eu molar ratios; **(b)** Comparison of XRD diffraction peak positions of Eu-doped ZnO (red) and undoped ZnO (black).

Table 1. The crystal size of ZnO nanoparticles according to Eu^{3+} dopant concentration.

The concentration of doped Eu^{3+}	Δ (2θ) (radian)	2θ (degree)	D (nm)
1%	0.217	36.287	38.60
5%	**0.239**	**36.305**	**34.92**
10%	0.219	36.294	38.17

Table 1 shows that the material Eu-doped ZnO synthesized with a 5% mol doped manganese content has the smallest crystal size. Therefore, the 5% mol Mn-doped ZnO was selected to examine the characteristic properties and photo-oxidation capabilities through the photo-catalytic reaction.

3.1.2. Characteristic properties of Eu-doped ZnO material

Figure 2 shows the presence of Eu in the Eu-doped ZnO material over the EDS spectrum. This result shows the presence of elements such as Zn, O, and Eu in the sample. In addition, there was no foreign element present. These data again demonstrate the existence of europium in high-purity samples and prepared materials.

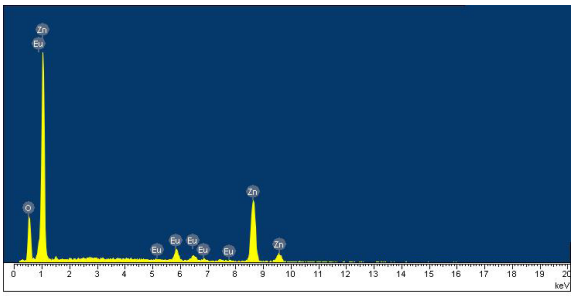

Figure 2. EDS spectra of (5%) Eu-doped ZnO nanoparticles.

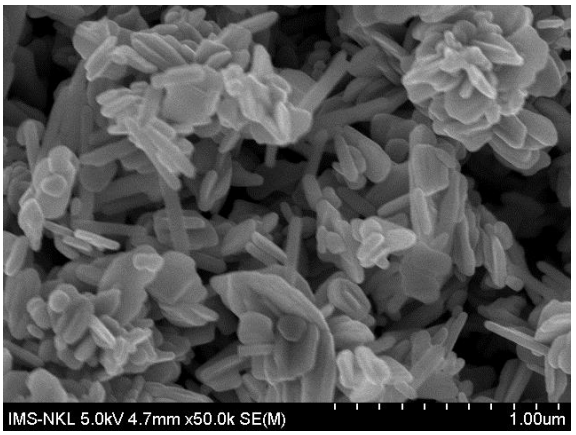

Figure 3. SEM images of (5%) Eu-doped ZnO nanoparticles.

The shape and size of Eu-doped ZnO are shown in the SEM image (Figure 3). The results of the SEM analysis show that Eu – ZnO particles are hexagonal in shape, with particle widths ranging from 32 to 72 nm and lengths from 127 nm to 367 nm.

3.2. The Mn-doped ZnO characteristics

3.2.1. Effect of the amount of Mn dopant

After synthesis, the Mn-doped ZnO materials were studied by using the XRD method. The results show that the concentration of Mn^{2+} ions does not affect the crystal phase composition.

No presence of diffraction peaks of manganese metal or manganese oxides was observed. Diffraction peaks correspond to the network plane families (100), (002), (101), (102), (110), (103) in accordance with the XRD scheme of the block ZnO - JCPDS Card No-00-036-145 (Figure 4). The XRD results also showed that the Mn^{2+} ions systematically replaced the Zn^{2+} ions in the sample without changing the wurtzite structure.[30]

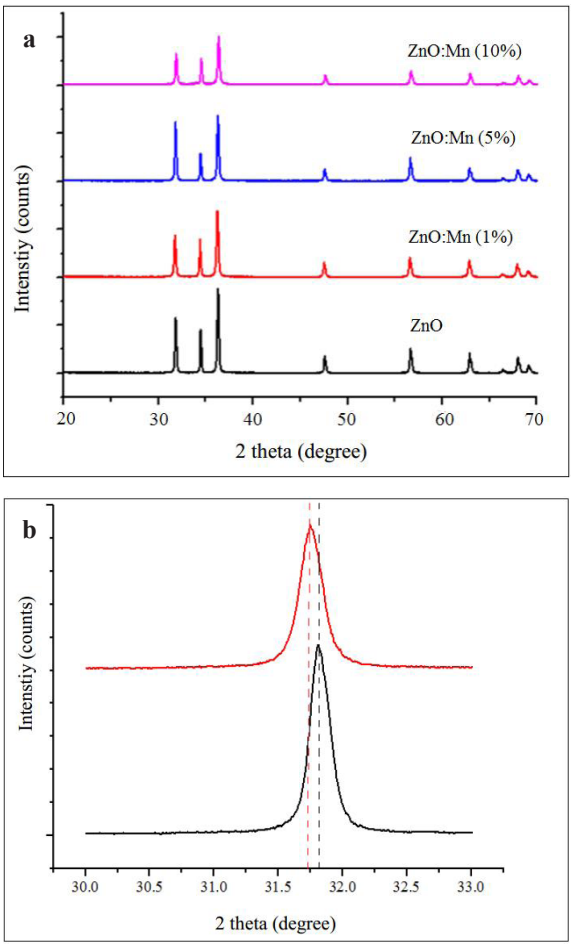

Figure 4. The XRD patterns for Mn-doped ZnO with different Mn dopant molar ratios, (b) Comparison of XRD diffraction peak positions of Mn-doped ZnO (red) and undoped ZnO (black).

The XRD results also show that the effect of the Mn dopant is related to the displacement of diffraction peaks towards a smaller 2 theta angle and a decrease in peak intensity compared to diffraction peaks of undoped ZnO. This fact (Figure 4a) shows that manganese was successfully doped into the ZnO network,[31] where the Mn^{2+} ions have replaced the Zn^{2+} ions. Mn^{2+} and Zn^{2+} ions have the same charge, and their ionic radius is not much different, so Mn^{2+} ions can easily enter the ZnO crystal lattice by partially replacing the Zn^{2+} ion's position or entering the lattice holes of ZnO.

Table 2 shows that the 1% (mol) Mn-doped ZnO material has the smallest crystal size. Therefore, the 1% mol Mn dopant concentration was chosen to examine its characteristic properties and photocatalytic.

Table 2. Effect of Mn doping on structural parameters of ZnO.

The concentration of doped Mn^{2+}	Δ (2θ) (radian)	2θ (degree)	D (nm)
1%	**0.222**	**36.240**	**37.65**
5%	0.205	36.291	40.78
10%	0.218	36.368	38.36

3.2.2. Characteristic properties of Mn-doped ZnO material

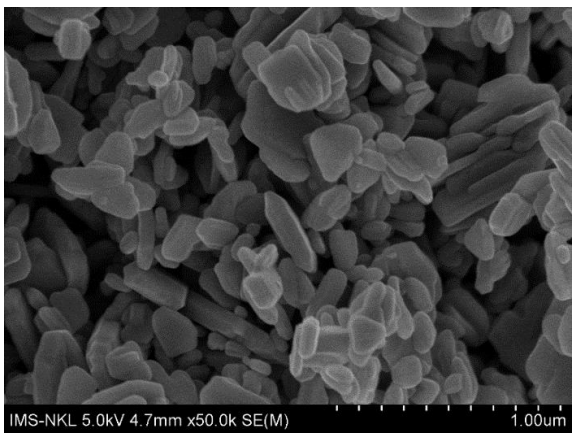

Figure 5. SEM images of Mn-doped (1% mol) ZnO nanoparticles.

The material's surface morphology can be seen from the SEM image of Mn-doped ZnO (Figure 5). This shows that Mn – ZnO materials are short rod-shaped particles with a slightly uniform arrangement, width size of about 19 nm to 56 nm, and length size of about 127 nm to 219 nm.

The synthetic Mn-doped ZnO material is of high purity. This result is proved by the EDS

https://doi.org/10.52111/qnjs.2023.17303

spectra of Mn-doped ZnO (Figure 6). It shows the presence of elements Zn, O, and Mn in the sample. In addition, the presence of foreign elements was not observed.

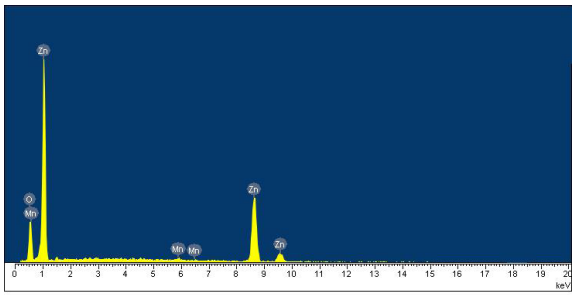

Figure 6. EDS spectra of Mn-doped (1% mol) ZnO nanoparticles.

3.3. Optical activity of metal ion-doped ZnO nanostructures

Photocatalytic activity of representative materials Eu, Mn-doped ZnO was investigated based on MB degradation reaction under UV light. The results of Figure 7 show that the relationship between the optical density and concentration of MB solution has a good linear range at low concentrations. This relationship has relatively good linearity in the MB concentration range from 0.1 to 24 mg/L (correlation coefficient $R^2 = 0.9927$).

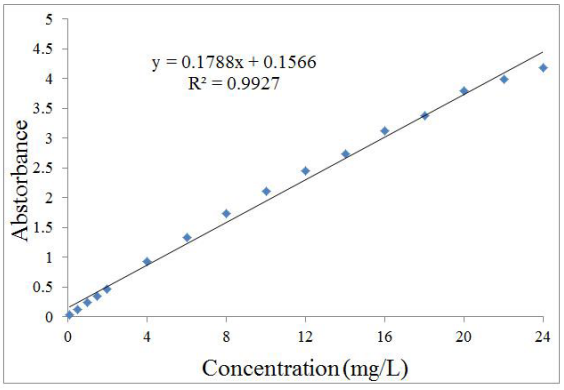

Figure 7. Calibration curve of MB solutions at λ_{max} = 664.4 nm.

However, the best linearity (correlation coefficient $R^2 = 0.9975$) was obtained in the MB concentration range of 4.0 to 16 mg/L. Therefore, the MB concentration of 10 mg/L was chosen for the photocatalytic reaction.

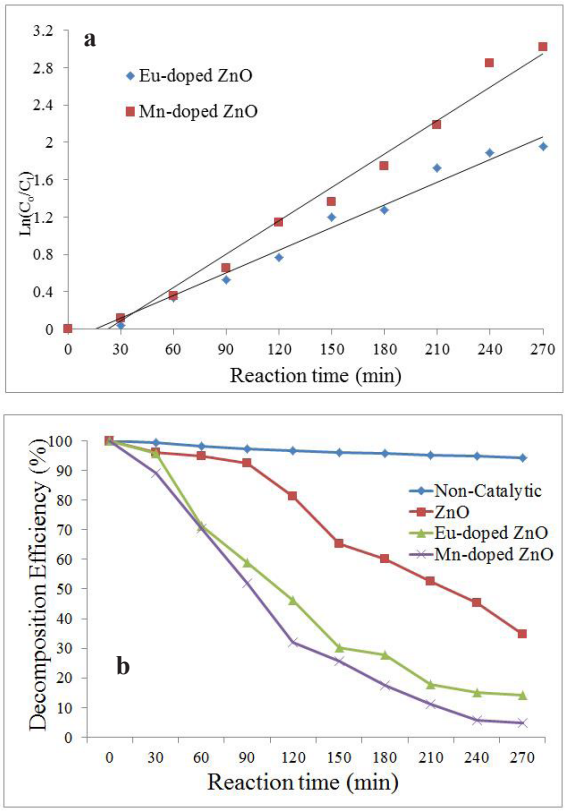

Figure 8. (a) Pseudo first-order rate kinetics for photocatalytic degradation of methylene blue dye; (b) Photodegradation efficiencies of Eu-, Mn-doped ZnO with ZnO.

The lines showing the relationship between $Ln(C_o/C_t)$ and MB decay time were almost linear (Figure 8a). It shows that the MB decomposition reaction kinetics of the materials investigated under the visible light follow the Langmuir – Hinshelwood model and simple 1st-order reaction kinetics. k - the reaction rate constant for Eu-doped ZnO material is 0.008 min^{-1}, and for Mn-doped ZnO material is 0.012 min^{-1}. The reaction rate constant of the Mn-doped ZnO catalyst is higher, which is consistent with the MB decomposition rate of the Mn-doped ZnO catalyst faster than the Eu-doped ZnO.

Figure 8b shows that the degradation efficiency of MB under UV light with Eu- and Mn-doped ZnO is higher than that of undoped ZnO. This result confirmed that europium and manganese doping changed the optical properties of ZnO. Thus, the doping of europium or manganese metal into ZnO increases the

photocatalytic activity of ZnO under UV light. Metal doping into ZnO leads to the formation of a new band gap energy state within the ZnO band gap. On the other hand, the doping of europium or manganese into ZnO increases defects. Both the new band gap energy states and lattice defects are intermediate factors that induce the excitation of electrons from the valence band to the gravitational zone when absorbing visible light.[32] One of the noteworthy effects of manganese doping into ZnO was the increase in defect concentration.[32,33]

3.4. Material reusability

Reusability is one of the essential factors when deciding on a material for the purpose of economic efficiency and environmental protection.[25] After the photocatalytic reaction, the Eu- and Mn-doped ZnO materials were rinsed several times with deionized water, dried at 90 °C for 12 hours, and reused to assess the photocatalytic ability at repeated use. The structure and composition of the crystal phase were examined.

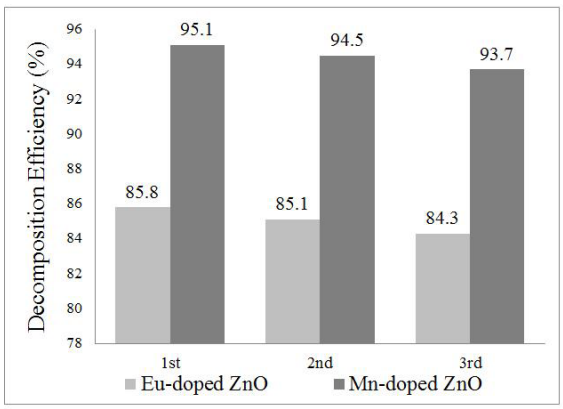

Figure 9. The MB decomposition efficiency of Eu - and Mn-doped ZnO materials after three reuse.

Figure 9 shows the results of the reusability of the two materials Eu- and Mn-doped ZnO. The results show that MB degradation efficiency decreased slightly after each reuse. After reusing them three times, the MB degradation efficiency still reached 84.34% with Eu-doped ZnO and 93.7% with Mn-doped ZnO.

4. CONCLUSION

This study was an attempt to synthesize Eu- and Mn-doped ZnO materials using the hydrothermal method. Data showed high crystallization and photocatalytic activity. In addition, all the materials tested demonstrated reusability. Furthermore, high substrate concentration was shown to inhibit biofilm systems' formation and growth, suggesting that there is an optimal substrate concentration. These findings will provide useful and progressive insights into the future applications of photocatalytic treatment on dye wastes.

REFERENCES

1. A. Boretti, L. Rosa. Reassessing the projections of the world water development report, *NPJ Clean Water,* **2019**, *2*(1), 1-6.
2. K. Vikrant, B. S. Giri, N. Raza, K. Roy, K.-H. Kim, B. N. Rai, R. S. Singh. Recent advancements in bioremediation of dye: current status and challenges, *Bioresource Technology,* **2018**, *253*, 355-367.
3. T. Ito, Y. Adachi, Y. Yamanashi, Y. Shimada. Long–term natural remediation process in textile dye–polluted river sediment driven by bacterial community changes, *Water Research,* **2016**, *100*, 458-465.
4. S. Srivastava, R. Sinha, D. Roy. Toxicological effects of malachite green, *Aquatic Toxicology,* **2004**, *66*(3), 319-329.
5. S. Sarmah, A. Kumar. Photocatalytic activity of polyaniline-TiO_2 nanocomposites, *Indian Journal of Physics,* **2011**, *85*(5), 713-726.
6. K. Rao. Inhibition of DNA synthesis in primary rat hepatocyte cultures by malachite green: a new liver tumor promoter, *Toxicology Letters,* **1995**, *81*(2-3), 107-113.
7. D. Alderman, R. Clifton-Hadley. Malachite green: a pharmacokinetic study in rainbow trout, Oncorhynchus mykiss (Walbaum), *Journal of Fish Diseases,* **1993**, *16*(4), 297-311.

8. L. Saikia, D. Bhuyan, M. Saikia, B. Malakar, D. K. Dutta, P. Sengupta. Photocatalytic performance of ZnO nanomaterials for self sensitized degradation of malachite green dye under solar light, *Applied Catalysis A: General,* **2015**, *490*, 42-49.

9. M. Qiao, K. Wei, J. Ding, Z. Liu, K.-Q. Zhang, X. Huang. Decolorizing activity of malachite green and its mechanisms involved in dye biodegradation by Achromobacter xylosoxidans MG1, *Microbial Physiology,* **2011**, *20*(4), 220-227.

10. A. Mittal. Adsorption kinetics of removal of a toxic dye, Malachite Green, from wastewater by using hen feathers, *Journal of Hazardous Materials,* **2006**, *133*(1-3), 196-202.

11. B. Pare, B. Sarwan, S. Jonnalagadda. Photocatalytic mineralization study of malachite green on the surface of Mn-doped BiOCl activated by visible light under ambient condition, *Applied Surface Science,* **2011**, *258*(1), 247-253.

12. Y. Liu, Y. Ohko, R. Zhang, Y. Yang, Z. Zhang. Degradation of malachite green on Pd/WO_3 photocatalysts under simulated solar light, *Journal of Hazardous Materials,* **2010**, *184* (1-3), 386-391.

13. J.-M. Herrmann, J. Disdier, P. Pichat. Effect of chromium doping on the electrical and catalytic properties of powder titania under UV and visible illumination, *Chemical Physics Letters,* **1984**, *108*(6), 618-622.

14. M. M. Khan, S. A. Ansari, D. Pradhan, D. H. Han, J. Lee, M. H. Cho. Defect-induced band gap narrowed CeO_2 nanostructures for visible light activities, *Industrial & Engineering Chemistry Research,* **2014**, *53*(23), 9754-9763.

15. C. Chen, T. Liu, L. Lin, X. Xie, X. Chen, Q. Liu, B. Liang, W. Yu, C. Qiu. Multi-walled carbon nanotube-supported metal-doped ZnO nanoparticles and their photocatalytic property, *Journal of Nanoparticle Research,* **2013**, *15*(1), 1-9.

16. S. Shinde, P. Shinde, C. Bhosale, K. Rajpure. Zinc oxide mediated heterogeneous photocatalytic degradation of organic species under solar radiation, *Journal of Photochemistry and Photobiology B: Biology,* **2011**, *104*(3), 425-433.

17. L. Li, T. Zhai, Y. Bando, D. Golberg. Recent progress of one-dimensional ZnO nanostructured solar cells, *Nano Energy,* **2012**, *1*(1), 91-106.

18. H. Zhang, B. Chen, H. Jiang, C. Wang, H. Wang, X. Wang. A strategy for ZnO nanorod mediated multi-mode cancer treatment, *Biomaterials,* **2011**, *32*(7), 1906-1914.

19. G. Wu, Y. Zhuang, Z. Lin, X. Yuan, T. Xie, L. Zhang. Synthesis and photoluminescence of Dy-doped ZnO nanowires, *Physica E: Low-Dimensional Systems and Nanostructures,* **2006**, *31*(1), 5-8.

20. H. Liu, X. Cheng, H. Liu, J. Yang, Y. Liu, X. Liu, M. Gao, M. Wei, X. Zhang, Y. Jiang. Structural, optical and magnetic properties of Cu and V co-doped ZnO nanoparticles, *Physica E: Low-dimensional Systems and Nanostructures,* **2013**, *47*, 1-5.

21. J. Li, N. Wu. Semiconductor-based photocatalysts and photoelectrochemical cells for solar fuel generation: a review, *Catalysis Science & Technology,* **2015**, *5*(3), 1360-1384.

22. Z. Wang, Y. Liu, B. Huang, Y. Dai, Z. Lou, G. Wang, X. Zhang, X. Qin. Progress on extending the light absorption spectra of photocatalysts, *Physical Chemistry Chemical Physics,* **2014**, *16*(7), 2758-2774.

23. J. I. Langford, A. Wilson. Scherrer after sixty years: a survey and some new results in the determination of crystallite size, *Journal of Applied Crystallography,* **1978**, *11*(2), 102-113.

24. R. Velmurugan, M. Swaminathan. An efficient nanostructured ZnO for dye sensitized degradation of Reactive Red 120 dye under solar light, *Solar Energy Materials and Solar Cells,* **2011**, *95*(3), 942-950.

25. F. Achouri, S. Corbel, L. Balan, K. Mozet, E. Girot, G. Medjahdi, M. B. Said, A. Ghrabi, R. Schneider. Porous Mn-doped ZnO nanoparticles for enhanced solar and visible light photocatalysis, *Materials & Design,* **2016**, *101*, 309-316.

26. R. Mohammed, M. E. M. Ali, E. Gomaa, M. Mohsen. Green ZnO nanorod material for dye degradation and detoxification of pharmaceutical wastes in water, *Journal of Environmental Chemical Engineering,* **2020**, *8*(5), 104295.

27. T. Ghrib, A. L. Al-Otaibi, I. Massoudi, A. M. Alsagry, A. S. Aljaber, E. A. Alhussain, W. S. Alrubian, S. Brini, M. A. Gondal, K. A. Elsayed. Effect of europium doping on the microstructural, optical and photocatalytic properties of ZnO nanopowders, *Arab Journal of Basic and Applied Sciences,* **2022**, *29*(1), 138-149.

28. M. Wang, C. Huang, Z. Huang, W. Guo, J. Huang, H. He, H. Wang, Y. Cao, Q. Liu, J. Liang. Synthesis and photoluminescence of Eu-doped ZnO microrods prepared by hydrothermal method, *Optical Materials,* **2009**, *31*(10), 1502-1505.

29. H. Shahroosvand, M. Ghorbani-asl. Solution-based synthetic strategies for Eu doped ZnO nanoparticle with enhanced red photoluminescence, *Journal of Luminescence,* **2013**, *144*, 223-229.

30. J. El Ghoul, C. Barthou, M. Saadoun, L. E. Mir. Synthesis and optical characterization of SiO_2/Zn_2SiO_4: Mn nanocomposite, *Physica B: Condensed Matter,* **2010**, *405*(2), 597-601.

31. Y. M. Hao, S. Y. Lou, S. M. Zhou, R. J. Yuan, G. Y. Zhu, N. Li. Structural, optical, and magnetic studies of manganese-doped zinc oxide hierarchical microspheres by self-assembly of nanoparticles, *Nanoscale Research Letters,* **2012**, *7*(1), 1-9.

32. M. A. Mahmood, S. Baruah, J. Dutta. Enhanced visible light photocatalysis by manganese doping or rapid crystallization with ZnO nanoparticles, *Materials Chemistry and Physics,* **2011**, *130*(1-2), 531-535.

33. Q. Xiao, L. Ouyang. Photocatalytic photodegradation of xanthate over $Zn_{1-x}Mn_xO$ under visible light irradiation, *Journal of Alloys and Compounds,* **2009**, *479*(1-2), L4-L7.

https://doi.org/10.52111/qnjs.2023.17303

TẠP CHÍ KHOA HỌC
TRƯỜNG ĐẠI HỌC QUY NHƠN

Nghiên cứu ứng dụng hệ thống giám sát môi trường nuôi tôm theo thời gian thực dựa trên công nghệ IoT

Đỗ Văn Cần*, Bùi Văn Vũ, Lương Ngọc Toàn, Nguyễn Quốc Bảo, Nguyễn Văn Quang

Khoa Kỹ thuật và Công nghệ, Trường Đại học Quy Nhơn, Việt Nam

Ngày nhận bài: 12/12/2022; Ngày nhận đăng: 27/03/2023; Ngày xuất bản: 28/06/2023

TÓM TẮT

Việc ứng dụng công nghệ IoT vào cuộc sống đã được triển khai trong những năm qua mang lại nhiều kết quả khả quan trong các lĩnh vực nông nghiệp, công nghiệp, thương mại. Lĩnh vực nông nghiệp được ứng dụng công nghệ IoT trong việc giám sát, chăm sóc, thu hoạch… đã mang lại nhiều lợi ích to lớn. Tuy nhiên việc giám sát các tham số cần kịp thời và chính xác trong một số lĩnh vực quan trọng như nuôi tôm là rất cần thiết, bên cạnh đó nền tảng IoT vẫn còn một số hạn chế như thiếu khả năng quan sát, cơ chế sửa lỗi không đầy đủ. Nhóm tác giả đã nghiên cứu ứng dụng công nghệ IoT vào giám sát môi trường nuôi tôm theo thời gian thực nhằm phát hiện xử lý kịp thời những biến đổi bất lợi đối với tôm, giảm thiểu thiệt hại cho hộ nuôi tôm. Kết quả thực nghiệm cho thấy tính hiệu quả của hệ thống này trong việc giám sát theo thời gian thực, mang lại lợi ích to lớn cho các hộ nuôi tôm ở địa phương.

Từ khóa: *Công nghệ IoT, giám sát môi trường, nuôi tôm, thời gian thực, đo lường xa.*

**Tác giả liên hệ chính.*
Email: dovancan@qnu.edu.vn

QUY NHON UNIVERSITY
JOURNAL OF SCIENCE

Research and application of Real-time monitoring system for shrimp farming environment based on IoT technology

Do Van Can*, Bui Van Vu, Luong Ngoc Toan, Nguyen Quoc Bao, Nguyen Van Quang

Faculty of Technology and Engineering, Quy Nhon University, Vietnam

Received: 12/12/2022; Accepted: 27/03/2023; Published: 28/06/2023

ABSTRACT

The application of IoT technology to life has been implemented over the years, it has brought many positive results to the fields of agriculture, industry and commerce. The agricultural field is applying IoT in the use of technology to observe, surveillance, and harvest, etc. that has brought many great benefits. However, the monitoring of parameters needs to be timely and accurate in some important areas such as shrimp farming. Besides, the IoT system still has several limitations such as lack of observability and inappropriate debugging mechanisms. The authors have researched and applied real-time monitoring system for shrimp farming environment based on IoT technology to detect and promptly handle adverse changes for shrimp, minimizing great damage to shrimp farmers. Experimental results show the effectiveness of this system in real-time monitoring, thereby bringing great benefits to local shrimp farmers.

Keywords: *IoT technology, environmental monitoring, shrimp farming, real-time, distance measurement.*

1. INTRODUCTION

The damage that occurs to shrimp farmers will negatively affect their economic life. In addition, dead shrimp in the ponds will lead to water pollution and ecological imbalance.[1]

In recent years, many shrimp farming households on Thi Nai lagoon have lost hundreds of millions of dong per crop which leads to their difficult economic life.[2] Besides, there are also some cases where shrimp farming households earn billions of dong per crop.

Currently, shrimp diseases occur frequently in many shrimp farming areas in the country, causing great economic losses to shrimp farming households. The main reasons are that environmental quality monitoring in shrimp ponds (shrimp) is not done regularly and there is a lack of control technologies to be able to react promptly to water quality problems.[3]

There are many studies on the application of IoT (Internet of Things) technology to shrimp farming,[4] but it has not been able to be implemented commercially. This is because the research cannot be done in a real environment and the commercial potential of the devices is not available yet (just for testing or teaching materials).[5,6] The general monitoring system for the whole area[7] cannot meet the specific needs of each specific shrimp farm.

*Corresponding author.
Email: dovancan@qnu.edu.vn

https://doi.org/10.52111/qnjs.2023.17304

Figure 1. Manual parameter monitoring.

When actually deployed, IoT research for shrimp farming has some disadvantages such as unstability,[5] communication inadequacies,[4] and disatisfation with real-time calculation (accuracy, low latency) for customers.[7] Therefore, IoT commercial products cannot bring great benefits to aquaculture in general and shrimp farming in particular.

Therefore, the authors study the application of a real-time monitoring system for shrimp farming environment parameters based on IoT technology to monitor these parameters accurately, with low latency, and can overcome limitations in communication. Furthermore, this system can work in harsh environments and has a high commercial orientation.

2. IMPLEMENTATION

2.1. Technological solutions in measuring shrimp farming environmental parameters

To successfully raise shrimp, it is necessary to ensure a series of water quality parameters such as dissolved oxygen concentration (DO), pH, salinity, temperature, ammonium nitrogen, NH_3, nitrite, H_2S, alkalinity, mineral concentration, nitrate concentration, phosphorus concentration, bacteria density, algae density[4] and so on. These parameters must be within the allowable range. As long as one of the above criteria exceeds the threshold, the growth of shrimp will be affected such as growth retardation, reduced resistance, infection or death. Therefore, it is very important to control water quality indicators for timely treatment to ensure that they are within the allowable threshold. The national technical regulation stipulates the threshold of parameters in shrimp ponds in Table 1.

Table 1. Appropriate water quality parameters in vannamei ponds.

No.	Parameter	Unit	Permissible limit
1	Dissolved Oxygen (DO)	mg/l	≥ 3.5
2	pH		7 ÷ 9 (±0.5)
3	Salinity	‰	5 ÷ 35
4	Alkalinity	mg/l	60 ÷ 180
5	Water clarity	cm	20 ÷ 50
6	NH_3	mg/l	< 0,3
7	H_2S	mg/l	< 0.05
8	Temperature	°C	20 ÷ 25

Many solutions that apply IoT technology to replace manual measurements have been deployed to monitor and control some parameters in the pond environment applying IoT technology to replace manual measurements[3,4,7] and so on. This system can help monitor the temperature and water level in the pond, control the heating device according to the actual temperature in the pond, send a warning signal to the manager and so on.

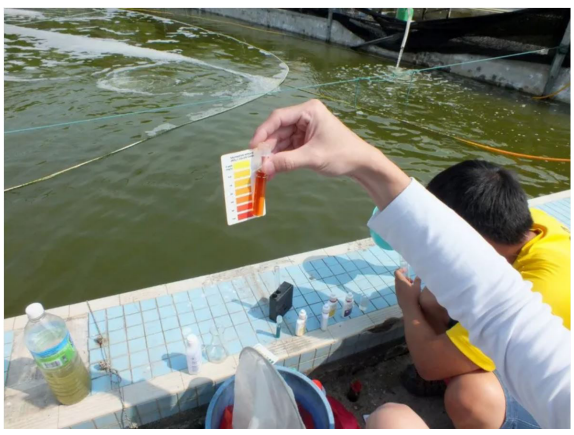

Figure 2. Manual measurement of environmental parameters.

To measure parameters at measurement points (called nodes) on shrimp ponds, the above parameters are sent to the control center thanks

to technologies such as Bluetooth, ZigBee, Wifi, LoRa. Each solution has its own advantages and disadvantages.

LoRa is a form of wireless technology with low energy consumption. It provides long range low power wireless connectivity for devices used in smart meter.[8] This solution is well suited for applications where direct mains power supply poses a hazard for ponds. It allows long distance communication and connection with intermediate nodes to increase the distance to collect measurement parameters.[7] Due to the low power consumption, RoLa technology is selected for application in monitoring the measurement nodes using Battery without power supply.[9]

2.2. Researching and proposing system solutions

Based on the advantages of LoRa such as long transmission distance and low energy consumption as shown in the research results in documents.[8,10,11] and based on the above literature analysis, the authors will use the sensor nodes including an Arduino UNO R3 to collect parameters, and water quality indicators and send these data to the data control station by LoRa wireless network at 433 MHz through the module LoRa Ra-02 SX1278.

Table 2. Communication protocol of the nodes in the measurement and data acquisition system.

LoRa SX1278 Module	Arduino UNO Board
Gnd	Gnd
3.3 V	3.3 V
En/Nss	D10
G0/DIO0	D2
SCK	D13
MISO	D12
MOSI	D11
RST	D9

Figure 3. Proposed measuring node model in shrimp ponds (experimental result).

Gateway (Control Station) is responsible for collecting data at all measuring nodes, then it analyzes, processes data, displays and communicates data accurately to ensure real-time to the user. Because of the important role of the center, the authors propose the Node-Red technology solution for the central control station to replace the previous basic programming methods[9,12,13] for real-time response in processing and displaying the results to the user.[14] The Node-Red technology has been covered in several references.[15-17]

There are four main components in the Node-Red editor namely:

1. The title is at the top, containing the Deploy button and the Main Menu.

2. The palette on the left-hand side contains the node libraries available to use.

3. The main workspace Workspace in the middle, where the Flows are created.

4. Right Sidebar

When accessing the Node-Red editor, the interface is described as displayed in Figure 4.

https://doi.org/10.52111/qnjs.2023.17304

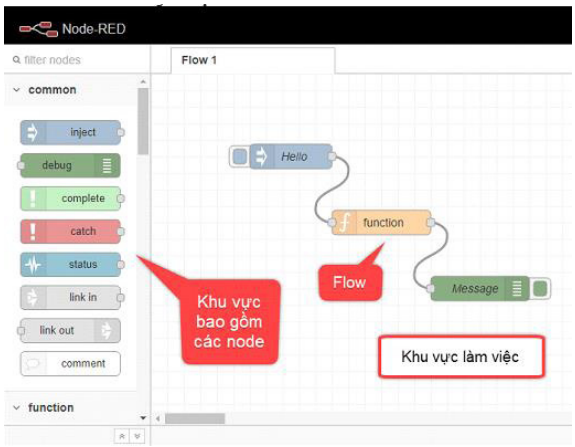

Figure 4. The interface of the tool Node-Red.[18]

After completing the design and running the Node-Red command, an IP address as shown below appears. We copy and paste the path http://127.0.0.1:1880/ into the web browser to access them. Node-Red with new features helps to overcome the disadvantages of previous IoT systems. Program development and debugging tasks help users easily understand the graphical programming structure, ensuring data processing bandwidth speed.

2.3. Designing the monitoring interface

The advantage of LoRa technology when transmitting data to the gateway is that it does not consume too much power. It allows data transmission over long distances. At the same time, the cost of sending will also be much lower than when sending using a regular mobile network.

The authors design a user interface on the Android platform (Figure 7) to access Server data through a central station that provides an IP address. In addition, to make it more convenient to monitor shrimp ponds anytime, anywhere, the system is also designed with a user interface on the Website platform. In this article, the JavaScript programming language is used to take advantage of the available open-source codes to build alarm systems, and control behavior when there is an abnormal change of parameters in the pond environment. In addition to the website, a data storage support tool called Firebase is used. In addition to supporting data storage, Google Firebase can also host and have a free name available so that we can minimize the cost of a system (Figure 6).

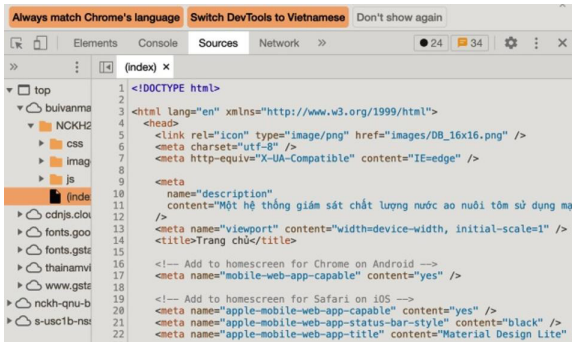

Figure 5. Programming user interface on Website platform using Javascript.

Data storage in the cloud is an important part of IoT projects in general and in wireless sensor networks (WSN) in particular. In this article, the authors use Google Firebase to store real-time data (Realtime Database) and help communication between hardware (sensor nodes and data collection nodes) and software (user interface).

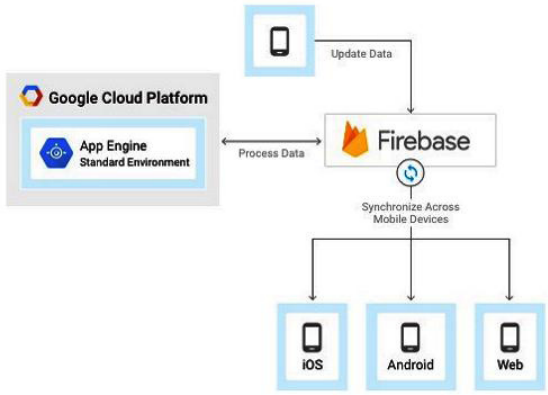

Figure 6. Diagram of data storage model through Firebase and signaling to iOS, Android and Web platforms.

Firebase is a backend system service provided by Google for mobile applications and websites. With Firebase, we can shorten the development, deployment, and scaling times of the mobile app or website we're developing. It supports both Android and IOS mobile platforms and website platforms. Firebase is a powerful, versatile, secure, and useful service for building apps. Google Firebase has a lot of tools to

assist users in building mobile or web-based applications.

Figure 7 shows sensor node data placed directly at the shrimp pond (unlimited number of nodes). The sensor nodes will measure the water quality parameters of the lake such as temperature, pH, oxygen concentration, salinity, etc. Then, the sensor node will send data to the gateway to help shrimp farmers monitor the parameters of water in the lagoon continuously and in real time.

Figure 7. Programming the user interface through the integrated web application development environment (MIT App Inventor).

2.4. Communication solutions for the system

The system monitors the environmental parameters of shrimp ponds using LoRa technology. In a WSN system, there must always be a gateway to collect data from sensor nodes and bring these data to a data processing center for different purposes or to be sent to the cloud via the internet.

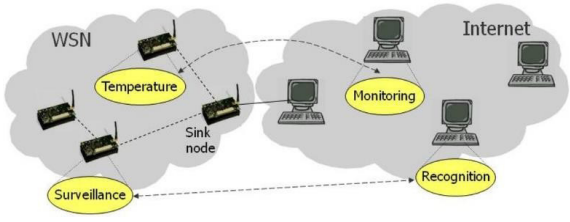

Figure 8. Communication and data acquisition solution of Central Control Station.[16]

The central system is designed by the authors using Node-RED technology. It allows users to combine web services and hardware by replacing common low-level encryption tasks (like a simple service that communicates with a serial port). This can be done with an intuitive drag-and-drop interface.[14] The different com-ponents in Node-RED are linked together to create a flow. Most of the necessary code is automatically generated to avoid data flow congestion, thereby providing a real-time response for systems.[14,18]

From the proposed model above, we can see that the sensor nodes are located at the water surface in the ponds. When receiving data from the sensor nodes, the data collection center will process and bring the data directly to the screen (temperature, pH, oxygen concentration, salinity,...) to give shrimp farmers observation directly at the center. At the same time, the data is updated on the website and App on the phone. At this time, it is easier for shrimp farmers to capture water parameters to manage their ponds when they are not present in the lagoon. This helps shrimp farmers manage the quality of the pond anytime, anywhere, which is convenient for capture and timely handling.

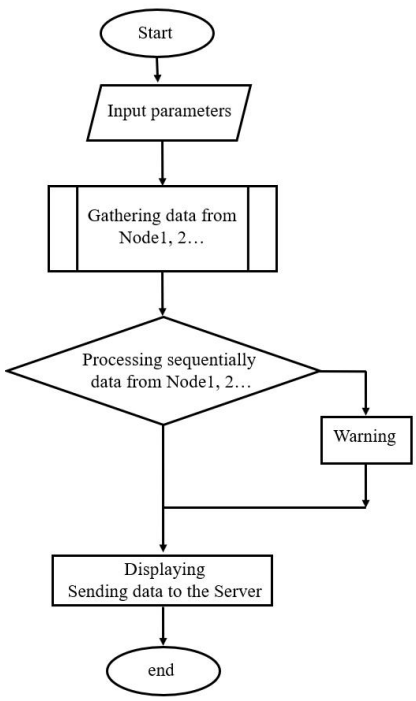

Figure 9. Algorithm flowchart built for Control Center.

https://doi.org/10.52111/qnjs.2023.17304

For the central controller, a stable internet connection (LAN, Wifi, 4G, GPRS) Node-Red is required. This allows real-time Modbus data exchange, which previous IoT systems could not do.[14,17]

2.5. Experimental results

Figure 10 shows that the authors have also designed a central controller using Raspberry (can be replaced by a PLC with communication module) and using Node-Red technology to build data exchange solutions with the nodes and send to the Server ensuring real-time requests.

Experimental results at shrimp ponds in Lac Dien village, Tuy Phuoc district, Binh Dinh province show that the control system has successfully sent remote data to Firebase via the link: https://nckh-qnu-bc114-default-rtdb.firebaseio.com.

Figure 10. Experimental model of control center.

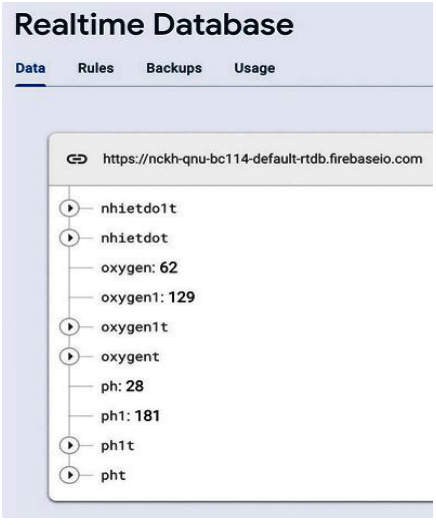

Figure 11. Experimental results are displayed on the calculator.

Parameters are within allowable limits and are updated continuously every 1s, ensuring real-time calculation for shrimp pond monitoring systems. In addition, the above system can provide a common database for scientists, shrimp hatcheries, fishery extension centers and so on.

In addition, the above data is also daily, monthly and yearly graphed to store historical parameters Figure 12.

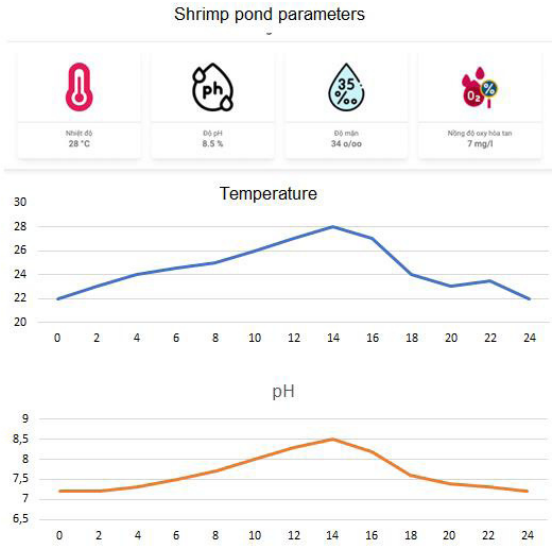

Figure 12. Experimental results are displayed on the computer.

In addition, the author has also designed the user interface to monitor the parameters of the second node with similar functions as the first node and evaluate the ability to communicate between nodes. Similarly, if people raise many shrimp ponds, the group can also develop Web interfaces to monitor water parameters of each pond, meeting the practical needs of the people.

In order for shrimp farmers to monitor environmental changes anytime and anywhere, the author has built a monitoring interface on iOS and Android platforms. The data is always updated on the manager's mobile device (Figure 13). In addition to the measured values displayed, the reference parameters are also given to the shrimp farmer. Because some sensors on the market are quite expensive, the authors only made experimental measurements for 4 main parameters: pH, salinity, temperature,

and dissolved oxygen. Figure 13 is the normal operating state of the first measuring node with pH = 8.1, salinity = 17.0‰, water temperature = 27.1 °C, and dissolved oxygen = 7.2 mg/l. Thus, the values are within the allowed range and are updated every 1 s (the Arduino board allows updates every 0.1 ms). Data is sent simultaneously to the common database and the user's mobile devices.

Figure 14 shows the same content as Figure 13, but the measured parameters are now assumed to have large fluctuations and exceed the allowable values set by the user. Specifically, the pH index is equal to 9.9, the temperature is equal to 34.0 °C. These two parameters will significantly affect the growth of shrimp and can cause shrimp to die in mass. In addition to the monitoring function, the system also has a warning function and an automatic message sending function to the user's device for timely handling.

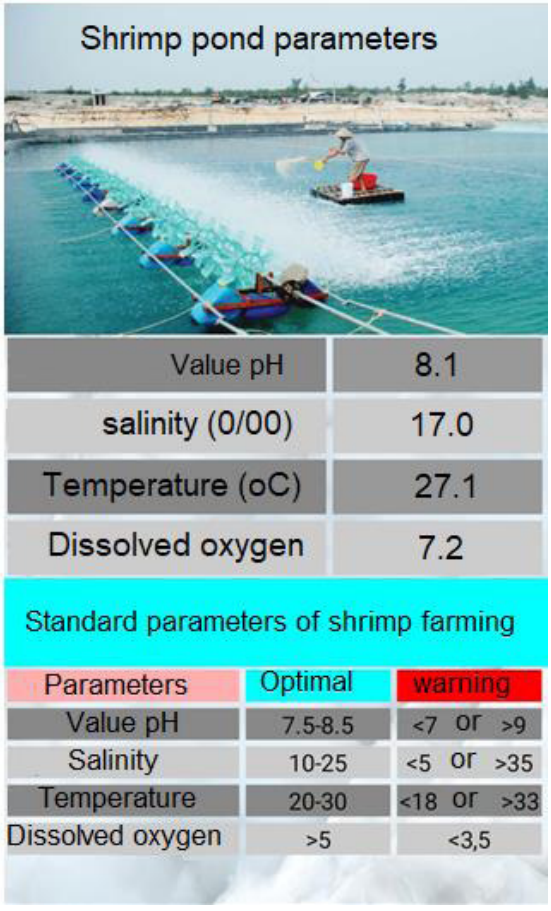

Figure 13. Monitoring interface when the measured parameters are at the allowable level.

Signal transmission by LoRa technology helps to increase the number of measured parameters at a node and the number of nodes in a farm thanks to low installation costs, relatively wide bandwidth, and easy communication between nodes. The authors have also developed nodes with an open structure, allowing users to connect more sensors, or replace sensors from measuring water environments to measuring other environments such as soil and air in plant care, smart greenhouses, etc.

The above research results have won consolation prizes in the contest of Student Scientific Research Prize – Euréka in Ho Chi Minh City 2022. (Proceeding of the Euréka Scientific Research Student Award 2022, http://eureka.khoahoctre.com.vn/)

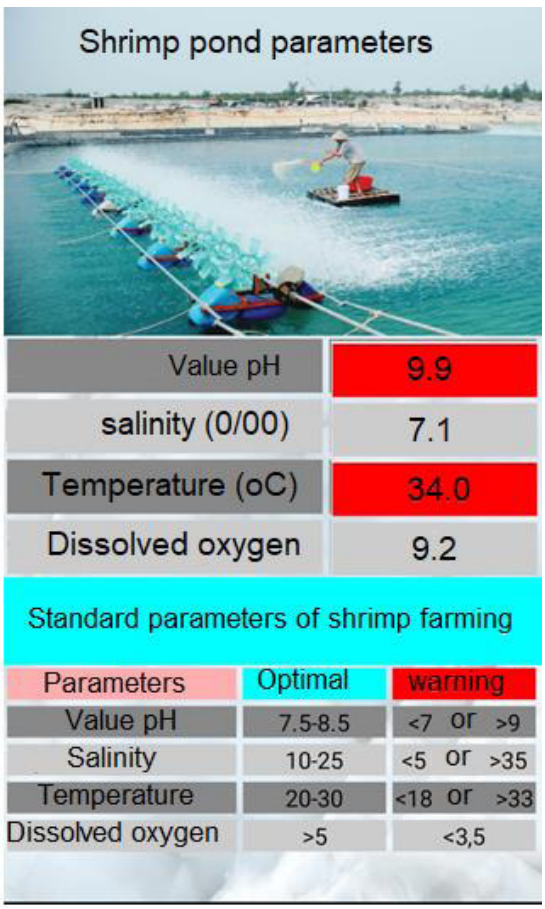

Figure 14. The warning interface in case the parameters exceed the allowable threshold.

3. CONCLUSION

The authors have successfully built a shrimp pond monitoring system using wireless sensor

https://doi.org/10.52111/qnjs.2023.17304

network (WSN) with 4 main monitoring parameters of water quality namely temperature, pH, dissolved oxygen concentration and salinity. Successfully configured communication to connect measuring point with control center by LoRa technology, data retrieval and data display on user's mobile device and on web based on platform of "Realtime Database" with Node-Red technology.

The system uses Node-Red technology to ensure real-time communication, increase reliability in measurement, allowing connection of LAN, Wifi, 4G, GPRS, etc.

The experimental results show that the designed system can monitor and display measured parameters continuously, ensuring real-time on users' mobile devices. The system can give warning signals to users when there are environmental parameters out of the set range and can output digital signals to control actuators such as: pump, beating fan, aeration and so on.

Measurement parameters are sent to a common database for various purposes and stored on the system in a time series.

Acknowledgment

This research is conducted within the framework of science and technology projects at institutional level of Quy Nhon University under the project code T2022.759.15.

REFERENCES

1. T. V. Dan, L. C. Tuan, N. Q. Lich, V. T. P. Anh. Study on treatment of total ammonium nitrogen (soluble) in white leg shrimp farming wastewater at Truong Son Joint Stock Company, Thua Thien Hue province, *Hue University Journal of Science,* **2012**, *2*(71).
2. D. Thung. Fishermen along Thi Nai lagoon lost the jellyfish season, *<https://nongnghiep.vn/ngu-dan-ven-dam-thi-nai-that-thu-mua-sua-d287312.html>,* retrieved on 06/06/2021.
3. N. M. Ha. *Applying IoT in the recirculation culture of vannamei shrimp,* The 4th industrial revolution with agriculture, Science and Technology Service and Application Center, 2018.
4. D. T. T. Huyen, N. K. Dung. Research design manufacture automatic monitoring and warning system for some environmental parameters in shrimp ponds, *Journal of Agricultural Science Vietnam,* **2021**, *19*(9), 1180-1189.
5. N. D. Tai, N. T. H. Quyen, N. V. Huong, D. D. Minh, N. T. H. Giang, V. H. Hai, T. T. Anh. Current status of IoT application in whiteleg shrimp farming in the Mekong Delta, *Vietnam Journal of Science and Technology*, **2020**, *12*, 32-34.
6. P. Q. Tri, N. N. Son, C. V. Kien. Designing experimental models of IoT applied in university teaching, *Journal of Science and Technology,* **2020**, *45A*.
7. P. X. Tuan, L. T. H. Nga, T. Q. Vinh, H. V. Hung, D. V. Hung. Application of advanced technology in monitoring and forecasting lobster farming environment in Phu Yen, *Engineering and Technology for Sustainable Development,* **2021**, *31*(3), 20-25.
8. Nur-A-Alam, M. Ahsan, M. A. Based, J. Haider, E. M. G. Rodrigues. Smart monitoring and controlling of appliances using lora based iot system, *Journal of Designs*, **2021**, *5*(1), 1-22.
9. B. A. Homssi, K. Dakic, S. Maselli, H. Wolf, S. Kandeepan, A. Al-Hourani. IoT network design using open-source lora coverage emulator, *IEEE open Access Journal,* **2021**, *9*, 53636-53646.
10. S. A. H. Almetwally, M. K. Hassan, M. H. Mourad. Real time internet of things (IoT) based water quality management system*, Procedia CIRP*, **2020**, *91*, 478-485.
11. R. S. Sinha, Y. Wei, S. H. Hwang. A survey on LPWA technology: LoRa and NB-IoT, *ICT Express,* **2017**, *3*(1), 14-21.
12. R. Islam, M. W. Rahman, R. Rubaiat, M. M. Hasan, M. M. Reza, M. M. Rahman. LoRa and server-based home automation using the internet

of things (IoT), *Journal of King Saud University - Computer and Information Sciences*, **2021**, *34*(5), 3703-3712.

13. K. Yasumoto, H. Yamaguchi, H. Shigeno. Survey of real time processing technologies of IoT data streams, *Journal of Information Processing,* **2016**, *24*(2), 195-202.

14. B. R. L. Michael. *Toward a distributed data flow platform for the Web of Things (Distributed Node-RED)*, WoT'14: 5th International Workshop on the Web of Things, 08 October, 2014, 34-39.

15. A. S. Mascarell, *Home automation platform based on node RED,* MA thesis in telecommunications technologies and services Engineering, Barcelona, June 2021.

16. M. Tabaa, B. Chouri, S. Saadaoui, K. Alami. *Industrial communication based on modbus and node-RED,* The 9th International Conference on Ambient Systems, Networks and Technologies (ANT 2018), Procedia Computer Science, Casablanca Morocco, 2018.

17. D. Torres, J. P. Dias, A. Restivo, H. S. Ferreira. *Real-time feedback in node-RED for IoT development: An empirical study,* The 24th International Symposium on Distributed Simulation and Real Time Applications, Prague, Czech Republic, 14-16 September 2020.

18. D. L. R. Torres. *Increasing the feedback on IoT development in node-RED,* MA thesis, Faculty of Engineering University of Porto, 13 July 2020.

https://doi.org/10.52111/qnjs.2023.17304

TẠP CHÍ KHOA HỌC
TRƯỜNG ĐẠI HỌC QUY NHƠN

Đánh giá tính kháng nảy mầm trước thu hoạch và bước đầu phân tích đa dạng di truyền của một số giống lúa trồng phổ biến trên địa bàn tỉnh Bình Định dựa vào đặc điểm hình thái

Trần Quang Tiến, Huỳnh Ngọc Thái, Nguyễn Đức Thắng, Võ Minh Thứ, Hồ Tân, Ngô Hồng Đức, Nguyễn Thanh Liêm*

Khoa Khoa học Tự nhiên, Trường Đại học Quy Nhơn, Việt Nam

Ngày nhận bài: 14/02/2023; Ngày nhận đăng: 05/05/2023; Ngày xuất bản: 28/06/2023

TÓM TẮT

Nghiên cứu đặc điểm hình thái, nông học, tính kháng nảy mầm trước thu hoạch và đa dạng di truyền của một số giống lúa trồng phổ biến trên địa bàn tỉnh Bình Định có ý nghĩa quan trọng trong việc đánh giá nguồn vật liệu khởi đầu phục vụ công tác chọn, tạo giống lúa mới thích ứng biến đổi khí hậu. Kết quả nghiên cứu trên 09 giống lúa cho thấy, có 1 giống cực ngắn ngày, 5 giống ngắn ngày và 3 giống trung ngày; 3 giống có tỷ lệ nảy mầm trung bình trước thu hoạch > 50% và 3 giống < 15%; các giống lúa nghiên cứu có chiều cao cây dao động từ 94,98 - 110,80 cm, số nhánh hữu hiệu từ 5,48 - 8,07 nhánh, chiều dài lá đòng từ 25,93 - 32,05 cm, chiều rộng lá đòng từ 1,17 - 1,51 cm, chiều dài bông từ 26,53 - 31,98 cm, chiều dài hạt gạo từ 5,91 - 8,41 mm, chiều rộng hạt gạo từ 2,31 - 3,60 mm, tỷ lệ D/R từ 2,15 - 3,32, khối lượng 1.000 hạt từ 19,85 - 24,23 g, số bông hữu hiệu/m^2 từ 279,83 - 351,66 bông, số hạt chắc/bông từ 108,50 - 154,33 hạt/bông, năng suất lý thuyết và năng suất thực thu của các giống dao động lần lượt từ 76,76 - 109,02 và 54,74 - 77,55 tạ/ha. Dựa trên 13 tính trạng kiểu hình, với hệ số tương đồng 0,03 các giống lúa nghiên cứu được phân thành 4 nhóm khác nhau cách biệt về di truyền. Số liệu thu được trong nghiên cứu này cung cấp thông tin tham khảo bước đầu cho các nhà nghiên cứu chọn lọc và cải tiến giống lúa thích ứng biến đổi khí hậu ở Bình Định nói riêng và vùng Duyên hải Nam Trung bộ nói chung.

Từ khóa: *Kháng nảy mầm trước thu hoạch, tỷ lệ nảy mầm, đa dạng di truyền, đặc điểm nông - sinh học.*

**Tác giả liên hệ chính.*
Email: nguyenthanhliem@qnu.edu.vn

QUY NHON UNIVERSITY
JOURNAL OF SCIENCE

Evaluation of pre-harvest germination resistance and initial analysis of genetic diversity of some popular rice varieties grown in Binh Dinh province based on morphological characteristics

Tran Quang Tien, Huynh Ngoc Thai, Nguyen Duc Thang, Vo Minh Thu, Ho Tan, Ngo Hong Duc, Nguyen Thanh Liem*

Faculty of Natural Sciences, Quy Nhon University, Vietnam

Received: 14/02/2023; Accepted: 05/05/2023; Published: 28/06/2023

ABSTRACT

Research on the morphological characteristics, agronomics, pre-harvest germination resistance, and genetic diversity of some popular rice varieties grown in Binh Dinh province is essential in assessing material resources for selecting and developing new rice varieties that can adapt to climate change. The results show that there is one extra short-day variety, five short-day varieties, and three medium-day varieties. Among these three varieties, there is an average pre-harvest germination percentage of over 50%, and three under 15%. The plant height ranged from 94.98 to 110.80 cm, effective tiller number per plant from 5.48 to 8.07, flag leaf length from 25.93 to 32.05 cm, and flag leaf width from 1.17 to 1.51 cm. The panicle length ranged from 26.53 to 31.98 cm, grain length from 5.91 to 8.41 mm, grain width from 2.31 to 3.60 mm, L/W ratio from 2.15 to 3.32, 1000-grain weight from 19.85-24.23 g, number of panicle/m^2 from 279.83 to 351.66, and filled spikelet per panicle from 108.50 to 154.33. The theoretical and actual yield of the varieties ranged from 76.76 - 109.02 and 54.74 - 77.55 quintals/ha, respectively. Based on 13 phenotypic traits, the rice varieties studied were classified into 4 groups of genetic diversity with a coefficient of 0.03. The information obtained from this study is critical for breeding rice varieties that can adapt to climate change in Binh Dinh province in particular and South Central Region in general.

Keywords: *Pre-harvest sprouting, germination percentages, genetic diversity, agronomic characters.*

1. INTRODUCTION

Rice (*Oryza sativa* L.) is an important cereal that feeds more than 50% of the world's population. Therefore, rice has made significant contributions to the global food security strategy. According to the Food and Agriculture Organization of the United Nations (FAO, 2021), there are approximately 144 countries growing rice, distributed across all continents, with a total area of 164.19 million ha, an average yield of 4.61 tons/ha, and a production of 756.74 million tons.[1]

Asia has 140.46 million ha of rice land, accounting for 85.54% of the total global area. Of these, 69.21 million ha (49.27%) are regularly threatened by natural disasters, with 36.72 million ha entirely depending on rainwater (rainfed rice), 19.15 million ha being dry land (upland rice), and 13.34 million ha prone to flooding. As a result, nearly 20% of the area is

*Corresponding author.
Email: nguyenthanhliem@qnu.edu.vn

https://doi.org/10.52111/qnjs.2023.17305

severely flooded. Rice yield in disaster-affected areas is only 0.8 - 1.7 tons/ha, which is 20 - 40% of rice yield in non-disaster-affected areas.[1]

Pre-harvest sprouting (PHS) is a phenomenon in which seeds germinate on the plant directly before harvest. PHS is associated with early hibernation break and usually occurs in conditions of high air humidity or prolonged rainfall, greatly affecting yield and grain quality.[2,3] This is a very common phenomenon in higher plants; PHS has been observed in nearly 100 species of flowering plants (belonging to 40 genera and 23 different families).[4,5] PHS, in particular, is found on many crops and in most parts of the world, including rice.[6]

Many studies on rice have shown that the seed dormancy mechanism is closely related to the water loss process that occurs during the grain's ripening stage, and that the amount of carbohydrate accumulated is proportional to the amount of water lost in seed development. However, because of unseasonal rains or continuous, prolonged rainy weather accompanied by high temperatures near harvest, conditions have been created for stored carbohydrates to "store" water, thereby breaking the process of seed dormancy through changes in hormones (particularly ABA and GA), which causes the embryo to develop inside the seed coat while it is still on the plant.[7]

The study of genetic diversity based on morphological and agronomic traits is a classic method that is still widely used today because it does not require expensive equipment or complex experimental arrangements while still ensuring certain efficiency, allowing researchers to distinguish varieties quickly in the field. Therefore, assessing the agro-biological characteristics and genetic diversity of rice varieties based on phenotype will assist breeders in selecting rice varieties with many desirable traits for use as a source of starting material for the breeding of rice varieties with high resistance to PHS.[8-13]

Rice is the most important food crop in Vietnam, feeding 100% of the population. According to the General Statistics Office, the rice-cultivated area was 7.24 million ha in 2021, with an average yield of 6.06 tons/ha, a production of 43.85 million tons, and an export of 6.2 million tons, which was approximately $3.2 billion. Thus, after more than 30 years of renovation, Vietnam has made significant strides in rice production while also ensuring national food security.[14]

Currently, global climate change is caused by the earth's warming, resulting in hot weather, high temperatures, storms, floods, and droughts occuring on a continuous and increasing basis. The World Meteorological Organization predicts that Asia will be the most affected by climate change over the next 50 years, and Vietnam is one of the five worst-affected countries.[15] Furthermore, because Vietnam is located in the sub-equatorial tropics, with steep terrain and a long coastline, tropical depressions, storms, and floods are common. As a result, rice production and cultivation in Vietnam has faced numerous challenges, including global climate change, sea level rise, saline intrusion, drought, and flooding. Prolonged rainfall and high humidity during the harvest season will cause early germination on pre-harvest flower, seriously affecting rice yield and quality and causing significant economic losses. According to Hu Weimin, the phenomenon of PHS reduces conventional rice yield by 6%, hybrid rice yield by 20%, and causes a loss of billions of US dollars each year.[16]

In recent years, many provinces in Central Vietnam have been directly affected by abnormal and extreme weather phenomena that cause continuous and long-term heavy rains, causing hundreds of ha of rice to fall in flooded fields, which leads to the germination of rice seeds on the spikelet, causing heavy yield and quality losses and reducing the economic value of the rice grain by 20-50%. According to the Commanding Committee for Disaster Prevention and Search and Rescue, in 2019, over 4.000 ha of rice fields

in Quang Binh, over 100 ha in Quang Tri, and over 5.000 ha in Thua Thien – Hue province were submerged and damaged. More than 3.000 ha of rice land in Binh Dinh were completely submerged in water.

Central Vietnam was the region which suffered the heaviest consequences caused by floods and rains in 2020, with more than 49.93 ha of rice and crops being damaged. Recent heavy and prolonged rains in 2021 destroyed nearly 3.000 ha of rice during winter-spring crop in Quang Binh and over 5.000 ha in Ha Tinh, providing clear evidence of unseasonal rainy weather, which has a negative impact on rice production and cultivation. Therefore, the evaluation of "Evaluation of pre-harvest germination resistance and initial analysis of genetic diversity of some popular rice varieties grown in Binh Dinh province based on morphological characteristics" is one of the positive and feasible solutions, which helps breeders to select, improve, and create new rice varieties with good PHS resistance, high yield, and good quality, contributing to reducing potential risks and promoting rice production in the Central provinces in particular, and Vietnam in general in the near future.

2. MATERIALS AND METHODS

2.1. Experimental materials

The experiment was carried out on nine rice varieties that are commonly grown in Binh Dinh province to assess their morphological, agronomic, and PHS resistance (Table 1).

Table 1. The origin of experimental rice varieties.

No.	Variety	Origin
1	OM18	Cuu Long Delta Rice Research Institute's Department of Biotechnology
2	BDR999	Agricultural Science Institute for Southern Coastal Central
3	BDR17	
4	DV108	Originated from China and selected by ThaiBinh Seed Group
5	KD18	
6	Dai thom rang	
7	VNR20	Vietnam National Seed Group
8	Thien uu 8	
9	Dai thom 8	Southern Seed Corporation

2.2. Experimental methods

The experiment was carried out in accordance with National Regulations QCVN 01-55: 2011/BNNPTNT and QCVN 01-65: 2011/ BNNPTNT,[17] with the following modifications:

- The study was conducted in the Winter-Spring crop 2021 - 2022 at My Duc commune, Phu My district, Binh Dinh province.

- The experiment was set up in a randomized complete block design (RCBD) with three replications.

- The area of the experimental plot is 10 m^2 (2 m x 5 m); the distance between experimental plots within the same replicate is 40 cm, and the distance between replicates is 40 cm.

- Planting density: 20 x 10 cm (row spacing: 20 cm, tree spacing: 10 cm), 50 plants/m^2.

- Seasonal and experimental farming methods and techniques are used in accordance with the current rice cultivation process in the area and are overseen by the Departments of Agriculture and Rural Development of Binh Dinh province and Phu My district.

https://doi.org/10.52111/qnjs.2023.17305

2.3. Indicators and measures

Evaluation of PHS resistance: The PHS resistance of nine rice varieties was tested using the method of Nguyen *et al*.,[18] which is based on the seeds germination rate with minor modification. One hundred seeds from each plant harvested at 40 and 50 days after flowering were placed on doubled sheets of WhatmanNo. 1 filter paper in a 9 cm Petri dish; 10 ml of sterile water was added, and dishes were incubated at 30°C in darkness for 7 days. Tests were performed in triplicate. Seeds with coleoptiles that extended more than 2 mm were considered germinated. The germination percentage (%) is calculated as the number of germinated seeds divided by the total number of filled seeds x100 (%).[18]

- Morphological and agronomic characteristics of rice varieties were assessed in accordance with National Regulations QCVN 01-55: 2011/BNNPTNT and QCVN 01-65: 2011/BNNPTNT.

+ Growth time (days): The number of days from sowing to seed maturity (85% of seeds on panicles were ripen);

+ Flag leaf length (cm): Distance from the base to the tip of the leaf;

+ Flag leaf width (mm): Distance of the widest section of the leaf;

+ Panicle length (cm): The average distance from the panicle neck to the panicle tip of the panicles of three replicates;

+ Plant height (cm): Distance from soil surface to tip of the tallest panicle (awns ex-cluded);

+ Rice grain size: For each replicate, the length and width of the kernels of randomly selected 20 grains of rice were measured with a Baker E-02 (Japan), and the average value was used;

+ Grain shape: The ratio of length and width (L/W);

+ Number of panicle/m^2: Determined from three representative square meter regions that were randomly sampled from each plot;

+ Number of filled spikelet/panicle: The total number of filled spikelets/panicle was counted from 10 random clusters for each experimental plot;

+ Filled spikelet ratio (%): The percentage (%) of filled spikelets per panicle;

+ 1000-grain weight (g): 1000 well-developed whole grains of the three replicates were weighed, then the average value was used;

+ Theoretical yield (quintals/ha) = (Number of panicle/m^2) x (Number of filled spikelet/ panicle) x 1000-grain weight x 10^{-4};

+ Actual yield (quintals/ha) = Area harvested should not be less than 5 m^2/plot (at least two border rows should be discarded). Report yield in kg/ha on rough (paddy) rice at 14% moisture.

- Genetic diversity of rice varieties studied based on phenotype: The results of the traits evaluation and actual yield in the field of the studied rice varieties were used to build the similarity matrix. These matrices represent the genetic close relationship between the analyzed samples. The NTSYSpc 2.11a software converts data on genetic correlation between samples in the form of a matrix into a tree graph (also known as an evolutionary tree), and samples with coefficients are classified into a group.

2.4. Methods of data processing

The obtained data were biologically processed using Statistix software version 8.0, and the diversity of rice varieties based on phenotype was analyzed using the UPGMA method in NTSYS pc 2.11a software. Differences in mean values was compared using the LSD test at a significance level of 0.05.

3. RESULTS AND DISCUSSION

3.1. Pre-harvest germination resistance of rice varieties studied

The PHS resistance of rice varieties was assessed using the germination percentages of rice seeds at 45 and 50 days after the flowering. The lower the germination percentages were, the higher PHS

resistance was, and vice versa. Table 2 shows the germination percentages of rice varieties at 45 and 50 days after flowering. After 7 days of experimentation, three varieties that had low pre-harvest germination percentages (< 15%) were Thien uu 8 (11.56%), Dai thom 8 (12.36%), and Dai thom rang (12.79%). These are varieties with high PHS resistance. Three varieties which had average pre-harvest germination percentages (> 50%) were BDR999 (50.81%), KD18 (55.63%), and DV108 (60.43%). The resistance to PHS of these varieties need to be improved. This result is also the same with the recent research findings of Pham Quoc Trung *et al*., (2021), who found that many varieties of rice commonly cultivated in North and Central Vietnam have high pre-harvest germination percentages (> 50%) after 10 days of testing.[19]

Table 2. The percentages of germination of rice varieties at 45 and 50 days after the flowering.

Variety	Germination percentages (%)		
	45 day	50 day	Average
OM18	45.00	48.59	46.80
KD18	48.50	62.76	55.63
BDR999	42.84	58.77	50.81
DV108	58.37	62.48	60.43
BDR17	17.89	21.54	19.72
VNR20	35.43	48.97	42.20
Thien uu 8	10.54	12.55	11.55
Dai thom 8	11.50	13.21	12.36
Dai thom rang	12.58	13.00	12.79

However, after drying the rice varieties at 50°C for 7 days, the germination percentages of most of the varieties were > 90%. The results showed that all varieties, including Thien uu 8 (95.12%), Dai thom 8 (90.49%), and Dai thom rang (90, 25%), had their dormant state broken during heat treatment (Table 3).

Table 3. The percentages of germination of dried rice varieties at 45 and 50 days after the flowering.

Variety	Germination percentages (%)		
	45 days	50 days	Average
OM18	97.32	99.76	98.54
KD18	100	99.64	99.82
BDR999	95.82	99.87	97.85
DV108	97.21	100	98.61
BDR17	92.32	98.13	95.23
VNR20	94.35	99.16	96.76
Thien uu 8	90.24	100	95.12
Dai thom 8	88.27	92.71	90.49
Dai thom rang	82.87	97.63	90.25

3.2. Some morphological and agronomic characteristics of the rice varieties studied

The growing time (GT) of rice varieties is a genetic trait that is affected by environmental factors. Rice varieties are classified as follows by GT according to National Standard TCVN 13381-1:2021/BKHCN: Extra short-day (< 100 days), short-day (100 - 115 days), medium-day (116 - 130 days), and long-term (> 130 days). Table 4 shows the results of grouping rice varieties studied according to GT.

https://doi.org/10.52111/qnjs.2023.17305

Table 4. The groups of rice varieties based on growth time.

Trait group	The number of varieties	Varieties	Ratio (%)*
Extra short-day (< 100 days)	1	BĐR999	11.11
Short-day (100-115 days)	5	OM18, KD18, DV108, BDR17, VNR20	55.56
Medium-day (116-130 days)	3	Thien uu 8, Dai thom 8, Dai thom rang	33.33
Long-term (> 130 days)	0		0

Note*: *Percentage of total 9 varieties*

There is one extra short-term variety (11.11%), five short-term varieties (55.56%), three medium-day varieties (33.33%), and no long-term varieties. Thus, the GT of the studied rice varieties was relatively diverse, with the majority of them falling into the short and midium-day groups. The results of grouping according to GT are similar to the subgroup of commonly grown rice varieties in the Northwest (short and medium-day varieties) in Doan Thi Thuy Linh's previous report, and this is also a valuable trait in selecting and developing new rice varieties.[9]

The plant height, the effective tiller number per plant, the flag leaf length, the flag leaf width, the panicle length, the grain length, the grain width, L/W ratio, 1000-grain weight, the number of panicle/m^2, and other basic characteristics of rice plants are frequently used to evaluate the morphological differences of rice varieties, making it easier to group rice varieties in the field. Table 5 shows the findings of the study on the traits of the aforementioned rice varieties.

Table 5. The morphological characteristics of the rice varieties studied.

Variety	Plant height (cm)	Effective tiller number/ plant	Flag leaf length (cm)	Flag leaf width (cm)	Panicle length (cm)	Grain length (mm)	Grain width (mm)	D/R ratio	1000-grain weight (g)
OM18	100.15^{b}	6.66^{bc}	27.05^{b}	1.23^{a}	28.48^{b}	8.41^{h}	2.69^{d}	3.11^{f}	23.68^{e}
KD18	101.98^{e}	6.33^{b}	25.93^{a}	1.17^{a}	26.53^{a}	5.91^{a}	2.59^{c}	2.28^{c}	19.85^{a}
BDR999	100.66^{c}	8.05^{d}	27.03^{b}	1.38^{b}	30.51^{cd}	6.90^{b}	3.20^{f}	2.15^{a}	25.15^{f}
DV108	94.98^{a}	6.83^{bc}	29.93^{e}	1.25^{a}	31.98^{g}	7.46^{c}	2.60^{c}	2.87^{f}	20.34^{b}
BDR17	110.01^{f}	5.48^{a}	27.53^{c}	1.27^{a}	28.46^{b}	7.80^{e}	3.35^{g}	2.33^{d}	22.45^{d}
VNR20	101.16^{d}	6.50^{bc}	29.15^{d}	1.41^{bc}	30.56^{cd}	8.07^{g}	3.60^{h}	2.24^{b}	23.89^{e}
Thien uu 8	110.80^{g}	8.07^{d}	32.05^{h}	1.46^{bc}	31.26^{f}	7.92^{f}	2.97^{e}	2.66^{e}	20.68^{c}
Dai thom 8	100.33^{b}	6.33^{b}	31.05^{f}	1.38^{b}	30.91^{ef}	7.70^{d}	2.31^{a}	3.32^{g}	25.23^{f}
Dai thom rang	101.30^{d}	7.33^{bc}	31.55^{g}	1.51^{c}	30.33^{c}	7.49^{c}	2.40^{b}	3.11^{f}	23.66^{e}
CV(%)	***4.63***	***14.85***	***7.04***	***10.59***	***5.58***	***9.31***	***14.81***	***15.82***	***7.56***
LSD 0.05	***0.29***	***0.84***	***0.21***	***0.35***	***0.44***	***0.03***	***0.01***	***0.02***	***0.25***

Note: a,b,c… indicates a statistically significant difference at the 0.05 level; CV: Coefficient variance; LSD: Least significant difference.

The plant height of rice varieties ranged from 94.98 cm (DV108) to 110.80 cm (Thien uu 8), with the effective tiller number per plant ranged from 5.48 to 8.07. The results show that, there was one variety (DV108, accounting for 11.11%) of the semi-dwarf type with a plant height of less than 100 cm, and eight varieties (88.89%) of the medium typewith a plant height ranged between 100 and 120 cm, indicating that the varieties have good lodging resistance. The evaluation of the number of effective tiller/plant of the varieties revealed that there were seven varieties (77.78%) of medium panicle level and two varieties (Thien uu 8 and BDR999) of high panicle level (Table 6).

Table 6. The groups of rice varieties based on the plant height and the effective tiller number/plant.

Trait group	The number of varieties	Ratio (%)*
Plant height (cm)		
< 100 cm (semi-dwarf)	1 (DV108)	11.11
100-120 cm (medium)	8	88.89
> 120 cm (height)	0	0
Effective tiller number/plant		
< 5 tiller (less)	0	0
5-8 tiller (medium)	7	77.78
> 8 tiller (much)	2	22.22

Note*: *Percentage of total 9 varieties*

The flag leaf length of the varieties ranged from 25.93 cm (KD18) to 32.05 cm (Thien uu 8) and flag leaf width from 1.17 - 1.51 cm. None of the varieties had narrow leaves (flag leaf width < 0.8 cm) (Table 5). Panicle length is an important factor because it is a genetic trait that determines variety. Scientists frequently seek ways to increase panicle length in breeding because this is the primary economic indicator of rice. The panicle length of the varieties ranged from 26.53 cm (KD18) to 31.98 cm (DV108). There are six varieties (66.67%) with medium panicles (26 - 30 cm) and three (33.33%) with long panicles (> 30 cm).

Table 7. The groups of rice varieties based on the grain size and shape.

Trait group	The number of varieties	Ratio (%)*
Grain length (mm)		
Extra short (< 4.50 mm)	0	0
Short (4.51 - 5.50 mm)	0	0
Medium (5.51 - 6.50 mm)	1	11.11
Long (6.51 - 7.50 mm)	3	33.33
Extra long (> 7.50 mm)	5	55.56
Grain width (mm)		
Narrow (< 2.5 mm)	2	22.22
Medium (2.5 - 3.0 mm)	4	44.45
Width (> 3.0 mm)	3	33.33
Grain shape (L/W)		
Round (< 1,5)	0	0
Semi-round (1.5 - 1.99)	0	0
Semi-slender (2 - 2.49)	4	44.45
Slender (2.5 - 2.99)	2	22.22
Long slender (≥ 3,0)	3	33.33

https://doi.org/10.52111/qnjs.2023.17305

1000-grain weight (g)		
Extra low (< 20 g)	1	11.11
Low (20 - 24 g)	6	66.67
Medium (25 - 29 g)	2	22.22
High (30 - 35 g)	0	0
Extra high (> 35g)	0	0

Note*: *Percentage of total 9 varieties*

The grain size and grain weight are typical parameters of rice varieties that are controlled by genes and less affected by environmental factors. As a result, they are important characteristics used to group varieties. The classification of grain size and weight characteristics according to the IRRI (2002) (Tables 5 and 7) shows that, in terms of rice grain length, there are five varieties of extra long grain (55.56%), three varieties of long grains (33.33%), and only one variety of medium grain (11.11%). In terms of 1000-grain weight, there is one variety with a extra low 1000-grain weight (11.11%), six varieties with a low 1000-grain weight (66.67%) and two varieties with a medium 1000-grain weight (22.22%).

The number of panicle/m^2 and the number of filled spikelet/panicle are critical factors in determining rice yield. In this study, the number of panicle/m^2 of the rice varieties ranged from 279.83 (VNR20) to 351.66 (Thien uu 8), and the number of filled spikelet/panicle ranged from 108.50 (BDR17) to 154.33 (KD18) (Table 8).

3.3. The yield and yield components of the rice varieties studied

Yield is a synthetic factor of a variety; it is the result of rice plants' growth, development, accumulation, and synthesis of organic matter. Table 8 shows the yield and yield components of the rice varieties.

Table 8. Yield components of rice varieties.

Variety	No. Panicle/ m^2	No. Filled spikelet/ panicle	Filled spikelet ratio (%)	1000-grain weight (g)	Theoretical yield (quintals/ ha)	Actual yield (quintals/ ha)
OM18	305.16^{d}	121.17^{b}	14.81^{f}	23.68^{e}	87.56^{c}	59.38^{c}
KD18	310.00^{e}	133.50^{d}	17.07^{h}	19.85^{a}	82.15^{b}	56.98^{b}
BDR999	288.33^{b}	132.00^{d}	13.92^{e}	25.15^{f}	91.92^{d}	65.83^{e}
DV108	291.83^{c}	154.33^{g}	15.46^{g}	20.34^{b}	91.61^{c}	63.22^{d}
BDR17	315.16^{f}	108.50^{a}	17.52^{i}	22.45^{d}	76.76^{a}	54.74^{a}
VNR20	279.83^{a}	152.66^{g}	10.27^{b}	23.89^{e}	102.07^{f}	72.83^{f}
Thien uu 8	351.66^{h}	128.83^{c}	9.48^{a}	20.68^{c}	93.69^{e}	74.63^{g}
Dai thom 8	310.50^{e}	144.33^{f}	10.56^{c}	25.23^{f}	108.60^{g}	76.90^{h}
Dai thom rang	329.50^{g}	139.83^{e}	12.83^{d}	23.66^{e}	109.02^{h}	77.55^{i}
CV(%)	***6.77***	***10.45***	***19.74***	***7.56***	***10.97***	***12.58***
$LSD_{0.05}$	***1.38***	***1.87***	***1.25***	***0.25***	***0.03***	***0.27***

Note: *a,b,c… indicates a statistically significant difference at the 0.05 level; CV: Coefficient variance; LSD: Least significant difference.*

Table 8 shows that the theoretical yield and actual yield of the varieties ranged from 76.76 - 109.02 and 54.74 - 77.55 quintals/ha, respectively. The variety with the highest theoretical yield and actual yield was Dai thom rang (109.02 and 77.55 quintals/ha), followed by Dai thom 8 (108.60 and 76.90 quintals/ha), and the variety with the lowest theoretical yield and actual yield was BDR17 (76.76 and 54.74 quintals/ha).

3.4. Evaluation of genetic diversity of the rice varieties through phenotype

Genetic diversity can be assessed using either phenotype (morphological traits) or genotype (using molecular markers), in which the phenotype is expressed as a result of the interaction between genotype and environment. The study of genetic diversity based on morphological and agronomic traits is a classic method that is still widely used today because it does not require expensive equipment, the experimental setup is not complicated, and certain efficiency is guaranteed. The analysis of rice variety diversity was based on 13 traits: the average pre-harvest germination percentages, GT, the plant height, the effective tiller number/plant, the length and width of flag leaves, the panicle length, the grain length and grain width, the grain shape (L/W), the number of panicles/m^2, 1000-grain weight, and the actual yields. The data were analyzed using the UPGMA method in NTSYS pc 2.11a software and modeled as a tree diagram, as shown in Figure 1.

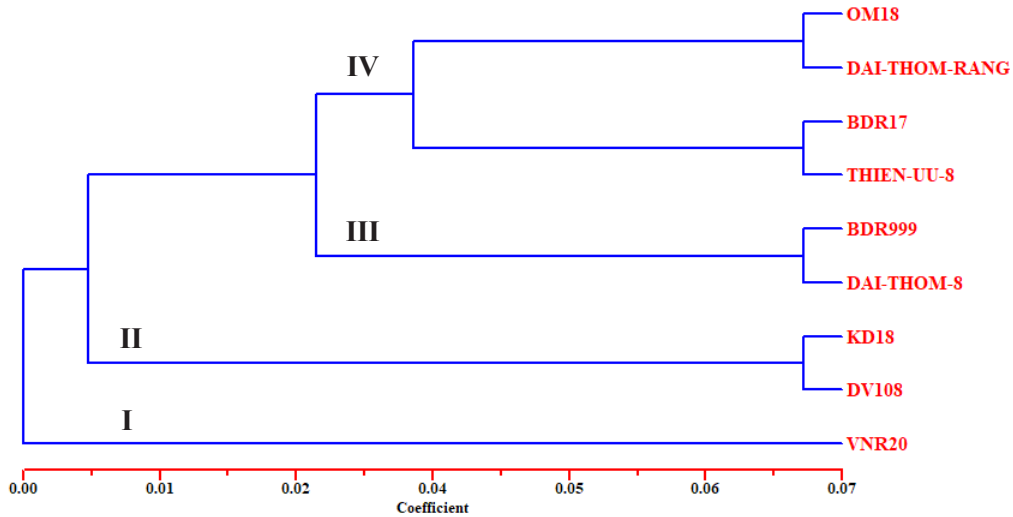

Figure 1. The genetic correlation of the rice varieties studied is depicted as a tree diagram.

The genetic grouping results of nine rice varieties studied revealed that if the coefficient is 0.03, they are classified into four genetic groups (Figure 1), which is then combined with three PHS groups (Tables 1) and four GT groups (Table 4). The results show that Group I contains only one variety (VNR20), which has a distant relation with the other varieties, and GT belongs to the short-day group with moderate resistance to PHS; Group II contains KD18 and DV108, both of which have short-day GT and low resistance to PHS; Group III contains Dai thom 8 (with medium-day GT and high resistance to PHS) and BDR999 (with extra short-day GT and low resistance to PHS); Group IV includes OM18, BDR17 (with short-day GT and moderate resistance to PHS) and Thien uu 8, Dai thom rang (with medium-day GT and high resistance to PHS). As a result, aromatic rice varieties frequently have longer GT and are highly resistant to PHS. This result also serves as the foundation for the research team to conduct additional studies on the relationship between aromaticity, GT, and PHS.

https://doi.org/10.52111/qnjs.2023.17305

4. CONCLUSION

The preliminary assessment of pre-harvest germination percentages revealed that there are three varieties with average pre-harvest germination percentages > 50% and three varieties with mean pre-harvest germination percentages < 15%.

The evaluation of some agro-biological characteristics shows that there are one extra short-day variety, five short-day varieties and three medium-day varieties; one variety is semi-dwarf and eight varieties have medium height; seven varieties with medium number of panicles and two varieties with high number of panicles; most varieties have medium length and width of flag leaves; six varieties with medium panicles and three varieties with long panicles; five varieties with extra long grains, three varieties with long grains and one with medium grains.

In terms of yield and yield components of the rice varieties, the number of panicle/m^2 ranged from 279.83 - 351.66, the number of filled spikelet/panicle from 108.50 - 154.33, and the 1000-grain weight from 19.85 - 24.23 g; the theoretical yield and the actual yield of the varieties were from 76.76 - 109.02 and 54.74 - 77.55 quintals/ha, respectively.

The rice varieties studied are classified into four genetic groups based on the coefficient of 0.03. Combined with three PHS groups and four GT groups, it is revealed that Group I contains only one variety with short-day GT and moderate resistance to PHS; Group II contains two varieties with short-day GT and low resistance to PHS; Group III contains one variety with medium-day GT and high resistance to PHS and one with extra short-day GT and low resistance to PHS; and Group IV contains two varieties with short-day GT and moderate resistance to PHS and two varieties with medium-day GT and high resistance to PHS.

REFERENCES

1. FAOSTAT. International agricultural statistics, [DB/OL],<http://faostat.fao.org/default.aspx.>, accessed on 12 May 2022.

2. H. Nonogaki J. M. Barrero, C. Li. Editorial: Seed dormancy, germination, and pre-harvest sprouting, *Frontiers in Plant Science*, **2018**, *9,* 1783.

3. M. V. Rodrıguez, J. M. Barrero, F. Corbineau, F. Gubler, R. L. Benech-Arnold. Dormancy in cereals (not too much, not so little): about the mechanisms behind this trait, *Seed Science Research*, **2015**, *25*(2), 99-119.

4. M. Q. Yao, W. W. Chen, J. H. Kong, X. L. Zhang, N. N. Shi, S. L. Zhong, P. Ma, P. Gallusci, S. Jackson, Y. L. Liu, Y. G. Hong. Methyltransferase1 and ripening modulate vivipary during tomato fruit development, *Plant Physiol*, **2020**, *183*, 1883-1897.

5. A. Ali, J. Cao, H. Jiang, C. Chang, H-P. Zhang, S. W. Sheikh, L. Shah, C. Ma. Unraveling molecular and genetic studies of wheat (*Triticum aestivum* L.) resistance against factors causing pre-harvest sprouting, *Agronomy*, **2019**, *9*(3), 117.

6. S. Nakamura. Grain dormancy genes responsible for preventing pre-harvest sprouting in barley and wheat, *Breeding Science*, **2018**, *68*, 295-304.

7. S. K. Nelson, T. Ariizumi and C. M. Steber. Biology in the dry seed: Transcriptome changes associated with dry seed dormancy and dormancy loss in the Arabidopsis GA-insensitive sleepy1-2 mutant, *Frontiers in Plant Science*, **2017***, 8*, 2158.

8. V. T. T. Hien. Genetic variation of rice (*Oryza sativa* L.) Accessions based on morphological characteristics, *Journal of Science and Development*, **2012**, *10*(16), 844-852.

9. D. T. T. Linh, N. V. Khoa. *Genetic diversity of native rice (Oryza sativa L.) in northwest basedon morphological characteristics,* The 5th National Scientific Conference on Ecology and Biological Resources, 2013.

10. P. T. T. Ha, D. T. Khang, P. T. Tuyen, L. T. Minh, T. N. Minh, N. T. Lang, B. C. Buu. T. D. X. Minh. Correlation among agro-morphological variation and genetic diversity of rice (*Oryza sativa* L.) under drought stress, *International Letters of Natural Sciences,* **2016**, *58*, 42-53.

11. T. T. H. Hai, D. T. Thuy, D. T. Long, H. H. Tran, N. M. Tuan. Genetic diversity based on morphological characteristics of Ngoc Linh Ginseng (Panax Vietnamensis Ha Et Grushv.) at Nam Tra My, Quang Nam*, Hue University Journal of Science: Natural Science*, **2018**, *127*(1), 203-210.

12. N. V. Tam, N. T. Nga, T. V. Vuong, P. T. Hien, T. N. Thanh, N. T. Huong, V. D. Hoa. Evaluating the genetic diversity and phenotypic correlationof giant crinum lily lines (*Crinum asiaticum* L.), *Vietnam Science & Technology*, **2019**, *61*(12), 36-40.

13. N. T. Q. Trang, D. T. Long, H. T. K. Hong. *Genetic diversity based on morphological characteristics of Lotus (Nelumbo Nucifera Gaernt.) Thua Thien Hue province*, The National Biotechnology Conference, 2021.

14. GSO. General Statistics Office of Vietnam, <https://www.gso.gov.vn/so-lieu-thong-ke/>, accessed on 19 October 2022.

15. WMO. World Meteorological Organization, <https://public.wmo.int/en>, accessed on 6 August 2022.

16. W. M. Hu, C. X. He & H. Ma. Genetic effects of pre-harvest sprouting in hybrid rice *(Oryza sativa* L.*)*, *Chinese Journal of Rice Science*, **2003**, *3*, 76–79 (In Chinese with English abstract).

17. Ministry of Agriculture and Rural Development. *National technical regulation on testing for value of cultivation and use of rice* (National Regulations QCVN 01-55 and 01-65: 2011/ BNNPTNT), 2011.

18. T. L. N. Nguyen, C. L. Zhou, T. Y. Zhang, J. F. Yu, R. Miao, Y. S. Huang, X. J. Zhu, W. H. Song, X. Liu, C. L. Mou, J. Lan, S. J. Liu, Y. L. Tian, Z. G. Zhao, L. Jiang and J. M. Wan. Identification of QTL for seed dormancy from weedy rice and its application to elite rice cultivar 'Ninggeng 4', *Molecular Breeding*, **2019**, *39*, 123.

19. N. Q. Trung, H. M. Chinh, C. D. Ha, N. T. Hong, D. T. Thuy, L. T. Hien, V. M. Thiet. Vietnam may conduct research on early germination resistance in rice in response to climate change, *Vietnam Journal of Science, Technology and Engineering*, **2021**, *3*, 4-7.

https://doi.org/10.52111/qnjs.2023.17305

TẠP CHÍ KHOA HỌC
TRƯỜNG ĐẠI HỌC QUY NHƠN

Tối ưu hóa quá trình tổng hợp biodiesel từ dầu ăn thải trên nền xúc tác tái tạo từ quá trình nhiệt phân vỏ trứng: Một nghiên cứu dựa trên phần mềm Minitab

Đặng Nguyên Thoại[1,2,*], Ngô Thị Thanh Hiền[2], Huỳnh Văn Nam[2]

[1]Trung tâm Tư vấn tuyển sinh và Quan hệ doanh nghiệp, Trường Đại học Quy Nhơn, Việt Nam
[2]Khoa Khoa học Tự nhiên, Trường Đại học Quy Nhơn, Việt Nam

Ngày nhận bài: 29/03/2023; Ngày nhận đăng: 05/05/2023; Ngày xuất bản: 28/06/2023

TÓM TẮT

Sản xuất biodiesel đã thu hút được sự chú ý đáng kể như một phương án thay thế cho các loại nhiên liệu hóa thạch truyền thống. Một lĩnh vực nghiên cứu triển vọng liên quan đến việc sử dụng các chất xúc tác tái tạo. Trong nghiên cứu này, chúng tôi đã tổng hợp chất xúc tác bazơ dị thể được lấy từ vỏ trứng bằng cách nung vỏ trứng thô ở nhiệt độ khoảng 800°C trong 6 giờ. Các đặc trưng của vật liệu được xác định dựa trên phổ XRD, ảnh SEM và phổ EDX. Phương pháp bề mặt phản ứng (RSM) được sử dụng để thiết kế thực nghiệm và tối ưu kết quả thực nghiệm dựa trên phần mềm Minitab (phiên bản 18). Dựa trên phương pháp bề mặt phản ứng, phương trình hồi quy được thiết lập để mô tả mối quan hệ giữa điều kiện thực nghiệm và hàm lượng ester trong biodiesel, với hệ số tương quan cao (R^2 = 0.956). Kết quả nghiên cứu này chứng tỏ rằng chất xúc tác từ vỏ trứng là một loại xúc tác tái tạo, thân thiện với môi trường và hoàn toàn thay thế được cho các chất xúc tác truyền thống. Phương pháp RSM dựa trên phần mềm Minitab có thể giúp tăng cường trong việc thiết kế thực nghiệm và tối ưu kết quả thực nghiệm.

Từ khóa: *Diesel sinh học, dầu ăn thải, vỏ trứng, phản ứng trao đổi ester, RSM.*

*****Tác giả liên hệ chính.*
Email: dangnguyenthoai@qnu.edu.vn

QUY NHON UNIVERSITY
JOURNAL OF SCIENCE

Optimization of the biodiesel synthesis of used cooking oil using calcined eggshell as a renewable catalyst: A study using Minitab software

Dang Nguyen Thoai[1,2,*], Ngo Thi Thanh Hien[2], Huynh Van Nam[2]

[1]Center of Admissions Consulting and Enterprise Relations, Quy Nhon University, Vietnam
[2]Faculty of Natural Sciences, Quy Nhon University, Vietnam

Received: 29/03/2023; Accepted: 05/05/2023; Published: 28/06/2023

ABSTRACT

The production of biodiesel has attracted significant attention as an alternative to traditional fossil fuels. One promising research area is related to the use of renewable catalysts. In this study, we synthesized eggshell-based heterogeneous base catalysts by calcining raw eggshells at approximately 800°C for 6 hours. The characteristics of the material were determined based on XRD spectra, SEM images, and EDX spectra. The response surface methodology (RSM) was used to design experiments and optimize experimental results using Minitab software (version 18). Based on the response surface methodology, a regression equation was established to describe the relationship between experimental conditions and the amount of ester in biodiesel, with a high correlation coefficient (R^2 = 0.956). The results of this study demonstrate that eggshell-based catalysts are renewable, environmentally friendly catalysts that can fully replace traditional catalysts. The RSM method based on Minitab software can enhance experimental design and optimize experimental results.

Keywords: *Biodiesel, Used cooking oil, eggshell, transesterification, RSM.*

1. INTRODUCTION

Biodiesel is generally defined as fatty acid alkyl esters produced from alternative resources through esterification, transesterification, or two-step reactions. It can be used directly or blended with petroleum diesel due to its acceptable properties. Traditionally, cooking oils have been the main resources for biodiesel production due to their low FFA content. However, relying on edible vegetable oils is a major disadvantage for commercial purposes due to their high price and potential impact on food security. As a result, non-edible oils such as waste cooking oil, Jatropha oil, and used cooking oils (UCO) have become increasingly attractive as renewable resources for biodiesel production at a lower cost.[1,2]

In this study, methyl ester was produced through the transesterification of UCO using calcined eggshell as a heterogeneous base catalyst. The objectives of this study were to: (a) investigate the production of a renewable catalyst through eggshell calcination; (b) assess the effect of MeOH/UCO molar ratio, catalyst/UCO catalyst content, and reaction temperature on the ester content in biodiesel; and (c) use response surface methodology (RSM) to design, analyze, and optimize experimental conditions.

**Corresponding author.*
Email: dangnguyenthoai@qnu.edu.vn

https://doi.org/10.52111/qnjs.2023.17306

2. MATERIALS AND METHODS

2.1. Materials

The study collected used cooking oil (UCO) and chicken/duck eggshells from various restaurants located in Quy Nhon City, Vietnam. The necessary chemicals, such as methanol (MeOH, purity > 99 wt.%), ethanol (EtOH, purity > 96 wt.%), and sulfuric acid (H_2SO_4, purity > 98 wt.%) provided by Binh Dinh Chemical and Scientific Equipment Co. Ltd. in Vietnam, are commonly used in this work.

2.2. Catalyst preparation

To prepare the eggshells for use, they were carefully separated from their membranes and thoroughly cleaned by rinsing with tap water three times. The cleaned eggshells were then dried in a hot air oven at 60 ^oC for 12 hours.[3]

Once dry, they were ground into a fine powder using a blender and then sieved to ensure a consistent size of 0.045 mm using a burger sieve. The resulting eggshell powder was then calcined in a muffle furnace at 800 ^oC for 6 hours to create the desired catalyst. The calcined eggshells were then stored in a desiccator to prevent any reaction with moisture or CO_2 in the air, which could be harmful to the catalyst's active site.[3,4] This careful storage was necessary to ensure the calcined eggshells remained free of unwanted particles and ready for use.

2.3. Characterization results of the catalysts

The calcined catalysts were characterized using XRD, SEM and EDX. XRD characterization was used for the phase identification; it was operated using Copper K-alpha (Cu Kα) radiation with 2θ in the range between 20^o and 80^o at a scan rate of 2^o /min.[4] SEM characterization was carried out at 10,000 times magnification under 5 kV electrical potential; it was utilized for the morphological studies.[5] EDX analysis is used in conjunction with SEM to characterize the elemental composition of the analyzed volume. SEM and EDX analyses were conducted at Institute of Materials Science, Vietnamese Academy of Science and Technology, Vietnam, while XRD analysis was performed at University of Science and Technology, The University of Danang, Vietnam.

2.4. Transesterification reaction procedure and phase separation

In order to produce biodiesel from used cooking oil (UCO), a transesterification reaction was conducted using methanol and a heterogeneous catalyst made from calcined eggshells. The reaction took place in a 0.5 L three-necked flask with magnetic stirring at a speed of 600 rpm, under atmospheric pressure and with water reflux at 20 ^oC to condense the methanol vapor.[6]

Prior to carrying out the transesterification reaction, UCO was decanted to remove impurities and dried at 110 ^oC within 2 hours. And then, the feedstock oil was preheated to the desired temperature and then the methanol-catalyst mixture was added. The start time for the reaction was recorded once all the methanol and catalyst had entered the reactor. After the reaction was complete, the product was transferred to a separatory funnel and allowed to settle for 60 minutes to separate into two phases: methyl ester and glycerol. The glycerol phase was removed, and the methyl ester phase was washed three times with hot water at 70 ^oC without stirring and three times with stirring. The washed methyl esters were then dried for 90 minutes at 110 ^oC. Finally, the resulting biodiesel was weighed to determine the methyl ester content.[6,7]

All experimental runs were conducted three times to minimize errors. The reaction time was set up at 40 min for all runs.[6] Some different reaction conditions were tested, such as methanol/WCO molar ratio (4.0 – 8.0), catalyst content (0.5 - 1.5 wt.%), and reaction temperature (45 - 65 ^oC).

Table 1. Experimental parameters used in transesterification of UCO.

Factors			Range and coded level		
Name of factor	Symbol	Dimension	-1	0	+1
MeOH/UCO molar ratio	X_1	mol/mol	4	6	8
Catalyst content	X_2	wt.%	0.5	1.0	1.5
Reaction temperature	X_3	^oC	45	55	65

2.5. Approximate analysis of ester content

To determine the ester content of biodiesel, the Thailand Patty Patent No. 5060 was used. This method involves using microwave radiation to determine total glycerides content in biodiesel through transesterification. Residue glycerides react with methanol and potassium methoxide to produce methyl esters and glycerol. The glycerol amount can be determined using a correlation curve, and the total glycerides content can be converted into ester content by subtracting it from 100 wt.%.[8]

2.6. Experiment designs

Response surface methodology (RSM) is a statistical technique that is commonly used to study the behavior of a response variable.[6,7] In this study, the Minitab software (version 18) was used to design and optimize the experiment results.

To determine the best conditions for the ester formation, the Box-Behnken design (BBD) was applied. This design combines three levels (-1, 0, +1) for each parameter, as shown in Table 1. Fisher's test (F-value), probability (P-value), correlation coefficient (R), and coefficient of determination (R^2) were used to predict the response of the transesterification process. Diagnostic plots, such as standardized residual and run number plots, expected normal value and residual plots, studentized residuals and predicted values plots, and predicted values and real values plots were also used to evaluate the model.

The second order polynomial regression model equation is typically expressed as Eq. (3).

$$Y = \beta_o + \sum_{i=1}^{3} \beta_i X_i + \sum_{i=1}^{2} \sum_{j=i+1}^{3} \beta_{ij} X_i X_j + \sum_{i=1}^{3} \beta_{ii} X_i^2 \quad (3)$$

Herein, Y is the predicted response (ester content); β_o, β_i, β_{ii}, β_{ij} are the regression coefficients (β_o is the constant term, β_i is a linear term, β_{ii} is a quadratic term and β_{ij} is an interaction term); X_i, X_j are coded independent factors.

Table 2. The coded independent factors, experimental results and predicted values from RSM.

Run	Independent Factors			Ester content (%)			Run	Independent Factors			Ester content (%)		
	X_1	X_2	X_3	Experiment	Predict	Residual		X_1	X_2	X_3	Experiment	Predict	Residual
1	4	1	65	89.4	90.64	-1.24	9	8	1.5	55	96.13	96.22	-0.09
2	8	0.5	55	91.58	92.69	-1.11	10	4	0.5	55	86.22	86.13	0.09
3	8	1	45	96.49	95.25	1.24	11	8	1	65	92.94	92.98	-0.04
4	6	0.5	65	92.4	91.25	1.15	12	4	1.5	55	94.58	93.47	1.11
5	4	1	45	88.32	88.28	0.04	13	6	1	55	84.85	84.75	0.10
6	6	0.5	45	91.58	91.71	-0.13	14	6	1	55	85.04	84.75	0.29
7	6	1.5	65	97.31	97.18	0.13	15	6	1	55	82.95	84.75	-1.80
8	6	1.5	45	95.49	96.64	-1.15	16	6	1	55	86.17	84.75	1.42

https://doi.org/10.52111/qnjs.2023.17306

Table 3. ANOVA results for the adjusted regression model.

Source/Term	Degree of freedom (DF)	Coefficient	Sum of squares (SS)	Mean squares (MS)	F-value	P-value*	Remarks
Model	9		314.83	34.98	15.45	0.0017	Significant
β_o		229.75				0.00019	Significant
Linear	3						
X_1	1	-2.152				0.522	Insignificant
X_2	1	-30.73				0.03394	Significant
X_3	1	-4.707				0.00167	Significant
Square	3						
X_1^2	1	0.621				0.01638	Significant
X_2^2	1	19.57				0.000631	Significant
X_3^2	1	0.04551				0.000924	Significant
Interaction	3						
X_1X_2	1	-0.952				0.252	Insignificant
X_1X_3	1	-0.05788				0.175	Insignificant
X_2X_3	1	0.05000				0.751	Insignificant
Residual	6		13.59	2.264			
Lack of fit (LOF)	3		8.235	2.745	1.5391	0.366	Insignificant
Pure error	3		5.350	1.783			
Total	15		328.42				
R^2: 0.959; adjusted R^2: 0.897; R^2 for prediction: 0.570							

**P-value < 0.05: statistically significant at the confident level of 95%*

3. RESULTS AND DISCUSSION

3.1. Conversion of eggshell into potential catalyst

3.1.1. XRD pattern of calcined eggshell

In order to identify the components and crystallinity of calcined eggshell, XRD analysis was conducted. As depicted in Figure 1, a peak at 2θ values around 34° for calcium oxide only appeared after the eggshells were calcined at 800 °C for 6 hours in a muffle furnace. This was likely due to the high thermal transition that occurred in the eggshells, causing complete decomposition of the calcium carbonate into calcium oxide at 800 °C. This result can be seen in a work by MD. Putra et al.[8] Additionally, a small peak for calcium hydroxide was observed, which can be explained by the hygroscopic nature of calcium oxide. It is noteworthy that both CaO and $Ca(OH)_2$ are alkaline and have the potential to be used as catalysts for biodiesel synthesis.

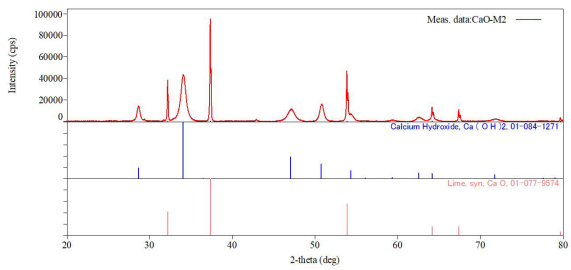

Figure 1. XRD pattern of calcined eggshell in a muffle furnace under 800 °C for 6 hours.

3.1.2. SEM characterization of calcined eggshell

The SEM image of the CaO catalyst obtained from the calcination-hydration-dehydration treatment of eggshells is presented in Figure 2. The image reveals a honeycomb-like porous surface and a regular micro morphology of

rod-like particles with a size of about 50 - 100 µm. This finding is consistent with a similar study conducted by S. Niju et al.[9]

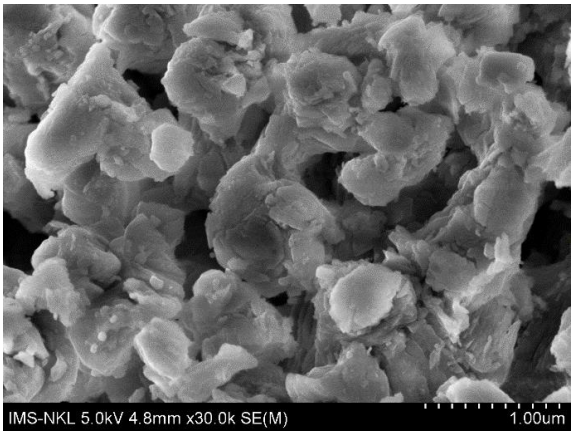

Figure 2. SEM image of calcined eggshell in a muffle furnace under 800 °C for 6 hours.

3.1.3. EDX characterization of calcined eggshell

The EDX pattern of the CaO catalyst obtained from the calcination of eggshells is shown in Figure 3. The results indicate that the EDX analysis conformed the presence of Ca, Mg and O in the sample of calcined eggshell. The main atomic components of calcined eggshells are Ca, and O, which are well-suited for serving as a potential heterogeneous base catalyst in the biodiesel synthesis process (Table 4).

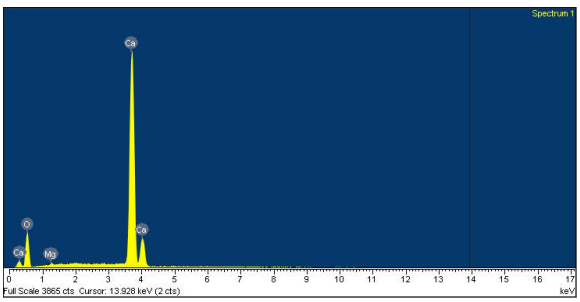

Figure 3. EDX pattern of calcined eggshell in a muffle furnace under 800 °C for 6 hours.

Table 4. The main atomic components of calcined eggshell.

Element	Weight, wt%	Atomic, %
O	53.93	74.48
Mg	0.35	0.32
Ca	45.71	25.20

3.2. Regression model and statistical analysis for the ester content in biodiesel

Table 2 presents both the experimental and predicted results for the methyl ester content in biodiesel. To analyze the obtained data, the full factorial BBD approach of RSM was utilized, and the resulting data was fitted to Eq. (3). The best-fit model was determined to be described by Eq. (4):

$$Ester\ content\ (\%) = 229.75 - 30.73X_2 - 4.707X_3 + 0.621X_1^2 + 19.57X_2^2 + 0.04551X_3^2 \quad (4)$$

In which, X_2 and X_3 are coded independent factors of catalyst content and reaction temperature, respectively; X_1^2, X_2^2, X_3^2 are code square factors of MeOH/UCO molar ratio, catalyst content and reaction temperature, respectively.

The results of the ANOVA for the adapted regression model are presented in Table 3. The adequacy of the designed model was assessed based on the F-value, P-value, R^2, and lack of fit (LOF). The F-value and P-value at 95% confidence level were 15.45 and 0.0017, respectively. The correlation coefficient (R^2) indicated that 95.9% of the variation in ester content was explained by the independent variables listed in Table 1, with only 4.1% attributed to random errors. Furthermore, the LOF was not significant (0.366 > 0.05), suggesting that the model was adequate for predicting the ester content in biodiesel.

Additionally, Table 4 shows that each term in the regression model was evaluated to determine its significance and its interrelation to the ester content in biodiesel. A P-value less than 0.05 indicated that the term was significant. After removing insignificant terms, the linear term of catalyst content (X_2) and reaction temperature (X_3), as well as the square terms of MeOH/UCO molar ratio (X_1^2), catalyst content (X_2^2), and reaction temperature (X_3^2) were found to be significant in Eq. (4).

https://doi.org/10.52111/qnjs.2023.17306

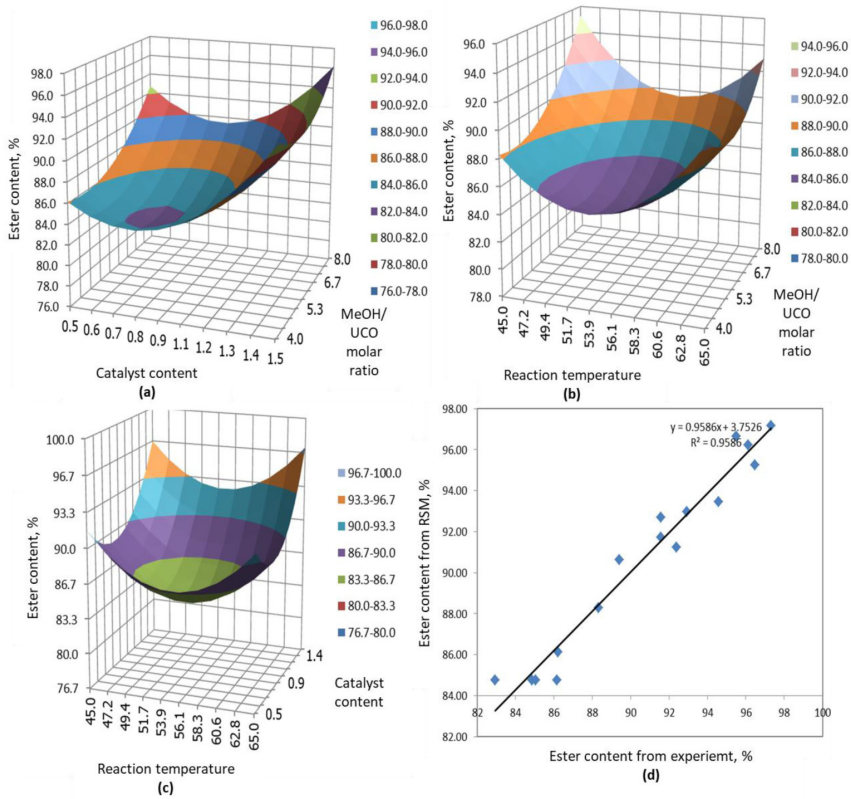

Figure 4. Interaction effects of the factors on ester content in biodiesel: (a) molar ratio and catalyst content, (b) molar ratio and reaction temperature; (c) catalyst content and reaction temperature; (d) predicted values and actual values plot.

3.3. Interaction effects of the factors on the ester content in biodiesel

The influence of interaction factors on the ester content in biodiesel was depicted in Figures 4a-4c. The contour slope indicated the degree of interaction's effect on the ester content in biodiesel, with a higher slope indicating a greater effect. The contour slope for catalyst content was higher than that for molar ratio (Figure 4a), indicating the significant effect of catalyst content in the range of 0.7 - 1.5 wt.%. The slopes of the catalyst content were higher than those of the molar ratio (Figure 4a) and reaction temperature (Figure 4c). These findings demonstrate the significance of calcined eggshell as a renewable catalyst in the transesterification reaction. The catalyst plays a crucial role in methyl ester formation, as shown in the coefficients of Eq. (4). Therefore, increasing the catalyst content accelerates the conversion of UCO to methyl esters (biodiesel). These results are consistent with previous studies.[6,10]

The predicted values were compared against real benefits and shown in Figure 4d, exhibiting linear behavior and being close to the diagonal line. As a result, the obtained model is suitable for predicting the ester content via transesterification reaction.

3.4. Optimization of variables for the ester content in biodiesel

The main objective of this study was to maximize the production of methyl ester in biodiesel. The experimental results showed that the ester content in biodiesel varied between 82% and 97%. To achieve a target ester content of 97%, the optimization was carried out using RSM. The optimal parameters were determined to be a MeOH/UCO molar ratio of 8 mol/mol, catalyst/UCO catalyst content of 1.5 wt.%, and a reaction temperature of 52 ^{o}C. This ester content of 97% ensured that the reaction takes place completely as per the standard EN 14214.[12]

4. CONCLUSIONS

In this study, the synthesis of biodiesel using calcined eggshell as a heterogeneous base catalyst was investigated. The following conclusions were drawn:

- The eggshell pyrolysis process was successful in producing the synthesized catalysts, which were characterized using XRD, SEM, and EDX spectra.

- A model was proposed to predict the influence of variables on the ester content in biodiesel, which showed good agreement with a high correlation coefficient ($R^2 = 0.956$).

- Ester content of 97% was obtained in the experimental conditions including: MeOH/UCO molar ratio of 8 mol/mol, catalyst/UCO catalyst content of 1.5 wt.%, and a reaction temperature of 52 ^oC.

- The effects of experimental variables on acid-catalyzed esterification were explored and optimized using RSM, including the MeOH/UCO molar ratio, catalyst content, temperature, and reaction time. The results showed that catalyst content was the most significant factor in the predicted model.

Acknowledgements

This study is conducted within the framework of science and technology projects at institutional level of Quy Nhon University under project code T2022.749.05.

REFERENCES

1. D. N. Thoai, C. Tongurai, K. Prasertsit, A. Kumar. Review on biodiesel production by two-step catalytic conversion, *Biocatalysis and Agricultural Biotechnology*, **2019**, *18*, 101023.
2. S. H. Venkataramana, K. Shivalingaiah, M. B. Davanageri, C. P. Selvan, A. Lakshmikanthan, M. P. G. Chandrashekarappa, A. Razak, P. B. Anand and E. Linul. Niger seed oil-based biodiesel production using transesterification process: Experimental investigation and optimization for higher biodiesel yield using box–behnken design and artificial intelligence tools, *Applied Sciences,* **2022**, *12*, 5987.
3. Y. C. Wong, R. X. Ang. Study of calcined eggshell as potential catalyst for biodiesel formation using used cooking oil, *Open Chemistry,* **2018**, *16*(1), 1166–1175.
4. Z. Wei, C. Xu, B. Li. Application of waste eggshell as low-cost solid catalyst for biodiesel production, *Bioresource Technology,* **2009**, *100*, 2883–2885.
5. A. R. Gupta, V. K. Rathod. Waste cooking oil and waste chicken eggshells derived solid base catalyst for the biodiesel production: Optimization and kinetics, *Waste Management*, **2018**, *79*, 169–178.
6. D. N. Thoai, C. Tongurai, K. Prasertsit, A. Kumar. A novel two-step transesterification process catalyzed by homogeneous base catalyst in the first step and heterogeneous acid catalyst in the second step, *Fuel Processing Technology* **2017**, *168*, 97–104.
7. P. T. T. Phuong, V. V. Tien, N. V. Quang, L. T. T. Ngan, D. N. Thoai. Central composite design-based optimization for conversion of free fatty acids in oil extracted from coffee grounds into biodiesel, *Quy Nhon University Journal of Science*, **2021**, *15*(3), 77-85.
8. S. Photaworn. *Process development of two-step esterification on waste vegetable oil with very high free fatty acid*, PhD thesis, Prince of Songkla University, 2017.
9. M. D. Putra, C. Irawan, Udiantoro, Y. Ristianingsih and I. F. Nata. A cleaner process for biodiesel production from waste cooking oil using waste materials as a heterogeneous catalyst and its kinetic study, *Journal of Cleaner Production,* **2018**, *195*, 1249–1258.
10. S. Niju, K. M. Meera, S. Begum, N. Anantharaman. Modification of egg shell and its application in biodiesel production, *Journal of Saudi Chemical Society,* **2014**, *18*, 702–706.
11. N. Tshizanga, E. F. Aransiola, O. Oyekola. Optimisation of biodiesel production from waste vegetable oil and eggshell ash, *South African Journal of Chemical Engineering,* **2017**, *23*, 145–156.
12. J. C. J. Bart, N. Palmeri, S. Cavallaro. Analytical methods and standards for quality assurance in biodiesel production, *Biodiesel Science and Technology, From Soil to Oil, Woodhead Publishing Series in Energy,* **2010**, 514–570.

TẠP CHÍ KHOA HỌC
TRƯỜNG ĐẠI HỌC QUY NHƠN

Thiết kế anten PIFA băng tần kép nhỏ gọn cho hệ thống thông tin 5G

Huỳnh Nguyễn Bảo Phương*, Đặng Thị Từ Mỹ

Khoa Kỹ thuật & Công nghệ, Trường Đại học Quy Nhơn, Việt Nam

Ngày nhận bài: 26/04/2023; Ngày nhận đăng: 08/06/2023; Ngày xuất bản: 28/06/2023

TÓM TẮT

Bài báo này đề xuất một anten PIFA băng tần kép hoạt động ở tần số 28/38 GHz cho hệ thống thông tin 5G. Anten PIFA gồm 2 lớp điện môi với một lớp không khí ở giữa. Cả hai lớp điện môi đều là Roger RT có hệ số điện môi tương đối là 2,2 và độ dày là 0,127 mm. Tấm bức xạ của anten là một miếng vá hình chữ nhật được khoét một khe xoắn ốc trên bề mặt để tạo ra băng tần kép tại 28 GHz và 38 GHz. Ban đầu, anten đề xuất được thiết kế dựa trên tính toán lý thuyết và sau đó được tối ưu kết quả bằng mô phỏng số sử dụng Phương pháp phần tử hữu hạn (FEM). Chiều dài tổng của tấm bức xạ xấp xỉ 0.25λg tại tần số 28 GHz. Kết quả mô phỏng số cho thấy anten PIFA đề xuất có thể hoạt động ở băng tần kép với dải phối hợp trở kháng đạt 5,7% (27 - 28,6 GHz) với $|S11| \leq -10$ dB và hệ số tăng ích thực đạt 6,81 dBi tại tần số cộng hưởng thứ nhất 28 GHz và dải phối hợp trở kháng đạt 14,5% (35,7 - 41,2 GHz) với $|S11| \leq -10$ dB và hệ số tăng ích thực đạt 6,81 dBi tại tần số cộng hưởng thứ nhất 28 GHz.

Từ khóa: *Anten PIFA, băng tần kép, hệ thống thông tin 5G.*

**Tác giả liên hệ chính.*
Email: huynhnguyenbaophuong@qnu.edu.vn

QUY NHON UNIVERSITY
JOURNAL OF SCIENCE

Design of Compact Dual-band PIFA Antenna for 5G Communication Systems

Huynh Nguyen Bao Phuong*, Dang Thi Tu My

Faculty of Engineering and Technology, Quy Nhon University, Vietnam

Received: 26/04/2023; Accepted: 08/06/2023; Published: 28/06/2023

ABSTRACT

This paper proposes a dual-band PIFA antenna operated at 28/38 GHz for 5G communication systems. The PIFA antenna consists of two dielectric layers and an air gap is inserted between these two layers. Both substrates, namely Roger RT dielectric, have a relative dielectric constant of 2.2 and a thickness of 0.127 mm. The radiator of the antenna is a rectangular patch in which a spiral slot is etched on its surface to create dual-band frequencies of 28 GHz and 38 GHz. Firstly, the proposed antenna is designed based on the theoretical calculations and then the numerical simulation using Finite Element Method (FEM) is used to optimize results. The total length of the radiator is approximately 0.25λg at the frequency of 28 GHz. The numerical results indicated the proposed PIFA antenna can be operated in a dual-band frequency with an impedance matching of 5.7 % (27 - 28.6 GHz) for |S11 |≤ –10 dB and a realized gain up to 6.81 dBi for the first resonant frequency at 28 GHz and an impedance matching of 14.5% (35.7 - 41.2 GHz) for |S11| < –10 dB and a realized gain up to 7.92 dBi for the second resonant one.

Keywords: *Dual-band, PIFA antenna, 5G communication systems.*

1. INTRODUCTION

Developing the compact antenna for 5G communication system has become an emerging interest among researchers due to the requirement of millimeter wave (mmW) systems in high-speed data and integration ability in a mobile device.[1] Up to now, the lower frequencies (below 6 GHz) have been used widely for 5G technology, while the higher one for mmW applications are still being researched and developed.[2] Given the advantages on wide band and the ability to provide high data rate, the upcoming use of the mmW band, i.e, 5G systems at 28 and 38 GHz frequencies increasingly attracts the interest of many researchers, especially the antenna for 5G systems.[3-6]

The PIFA antennas with the frequency bands of sub-6 GHz is popularly used in cell phones and other RF devices. Due to the unique characteristic in electrically small size of a quarter wavelength antenna, the PIFA antennas can be applied to integrate into 5G systems when the frequency bands reach 28 and 38 GHz. Thus, the wireless systems can transmit in different bands by using one antenna. The application of one antenna in wireless systems can minimize the communication systems.[7-13]

A dual-band PIFA antenna was investigated in the previous study of Hashem et al.[14] In this study, the antenna included a metallic patch connected to the ground plane by shorted pin with an air substrate. The system was operated

*Corresponding author.
Email: huynhnguyenbaophuong@qnu.edu.vn

https://doi.org/10.52111/qnjs.2023.17307

at 28 GHz and 38 GHz with a form factor of (1.3 mm x 1.83 mm). As a result, a quite high gain of 5 dBi and 5.5 dBi at the frequency of 28 GHz and 38 GHz, respectively was observed.[14] However, this antenna still has some disadvantages related to bandwidths. The narrow bandwidths of 700 MHz and 300 MHz were measured at 28 GHz and 38 GHz, respectively. After few years, a wide dual-band PIFA antenna with a small form factor had been proposed.[1] However, this antenna did not reach good performances at 28 GHz and 38 GHz. For instance, peak gain was only 3.75 dBi and 5.06 dBi.

This study aims to propose and investigate a dual-band PIFA antenna on double substrates with a small overall size. To increase the impedance bandwidths, an air layer was inserted into the two dielectric layers. As a result, the proposed PIFA yields a wide bandwidth and a high realized gain at both frequencies.

2. SINGLE-BAND PIFA ANTENNA DESIGN

There are three parts in this section. Firstly, the model of the single band PIFA antenna is proposed. After that, all the dimensions of the proposed PIFA are theoretically calculated based on the desired resonant frequency. Finally, the ANSYS Academic Research HF is used to simulate and optimize the initial dimensions for getting the final design.

2.1. Antenna geometry

The proposed PIFA antenna consists of two Roger RT dielectric layers with the same relative dielectric constant (ε_r) of 2.2 and a thickness (H_s) of 0.127 mm. A rectangular radiator metal plate (W x L) (mm2) is placed on the first dielectric layer. This plate is connected to a metallic ground plane by a metallic via. The second dielectric layer is put on the ground plane. An air layer with a thickness (H_air) of 0.344 mm is inserted between the two dielectric layers. The antenna is fed by a coaxial with an impedance of 50 Ω. The proposed PIFA antenna's configuration is depicted in Figure 1.

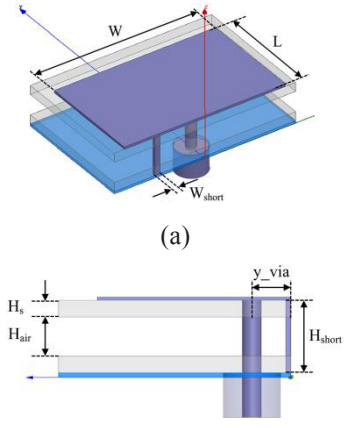

Figure 1. Configuration of the proposed single PIFA antenna: (a) Perspective view, (b) Side view.

2.2. Theoretical calculation

Based on microstrip antenna theory, the PIFA resonances at the frequency corresponding to the antenna's length is equal to ¼ wavelength at its resonant frequency.[15]

$$(L + W - W_{short})\sqrt{\varepsilon_{eff}} \approx \frac{\lambda}{4} \quad (1)$$

$$f = \frac{c}{4(L + W - W_{short})\sqrt{\varepsilon_{eff}}} \quad (2)$$

where, $$\varepsilon_{eff} = \frac{\varepsilon_r . \varepsilon_{air}(H_s + H_{air})}{\varepsilon_r . H_{air} + \varepsilon_{air} . H_s} \quad (3)$$

The effective dielectric constant (ε_{eff}) is calculated:

$$\varepsilon_{eff} = \frac{2{,}2 \times 1(0{,}127 + 0{,}354)}{2{,}2 \times 0{,}354 + 1 \times 0{,}127} \approx 1.17$$

The radiator size of the antenna at 28 GHz is calculated as Eq. (2). Thus, the initial dimensions of the antenna are chosen as follows: L = 1,1 mm, W = 1,32 mm và W_{sho} = 0,05 mm. The calculated results of the proposed antenna are provided in Table 1.

Table 1. Theoretical calculation dimensions of the proposed PIFA antenna (unit: mm).

Parameter	Value	Parameter	Value
W	1.32	L	1.1
W_g	1.52	L_g	1.3
W_{short}	0.05	H_{short}	0.55

2.3. Simulation and optimization

Return loss simulated result of the PIFA with the intial dimensions is depicted in Figure 2. It can be seen that the proposed single band PIFA yields a center frequency of 29.2 GHz. This simulated frequency is quite close to the one of theoretical calculation and it will be optimized to obtain the desired frequency of 28 GHz by investigating the dimensions of the antenna.

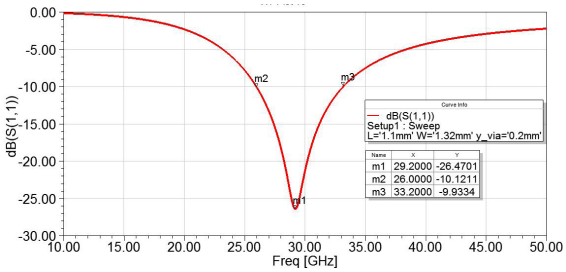

Figure 2. Simulated S11 of the PIFA with its theoretical calculation dimensions.

In order to determine the optimal dimensions corresponding to the desired resonant frequency at 28 GHz, the length (L) and the width (W) of the PIFA are selected for investigation. One parameter will be changed for investigating while another one will be fixed. Firstly, the width of the rectangular patch is considered when the length is fixed at 1mm. The simulation reflection coefficient of the PIFA with various values of W is shown in Figure 3. It is observed that the resonant frequency of the antenna decreases as the width of its radiator increases or the total electrical length of the proposed antenna increases. This observation is consistent with the theory when the frequency of the antenna its electrical length is inversely proportional each other, as shown in Eq. (2).

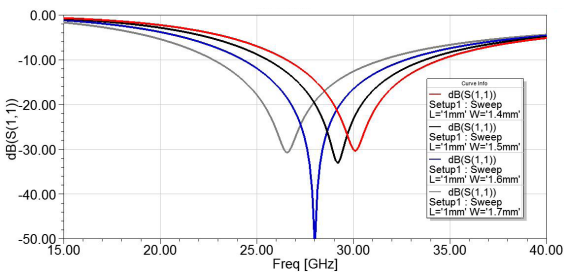

Figure 3. Simulated S11 of the single band antenna versus various values of W.

Next, the length of the patch (L) is investigated when the width W is set at 1.4 mm. Numerical S11 results of the antenna with various values of L are shown in Figure 4. Similarly, increasing the patch length leads to decrease the resonant frequency. These results could be explained that when the length of the patch changes, the electrical length of the antenna changes, which leads to the change in the resonant frequency.

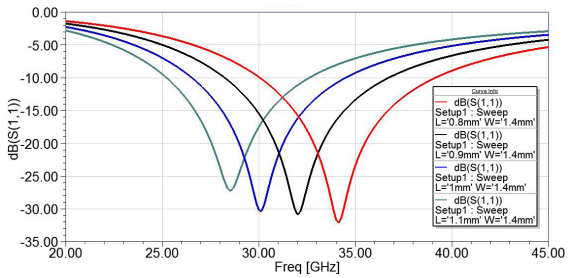

Figure 4. Simulation results of S11 of the single band PIFA with the various values of L.

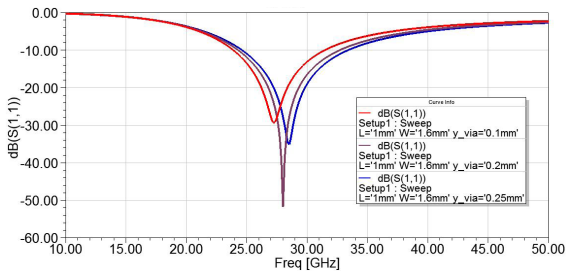

Figure 5. Simulation results of S11 of the single antenna versus to different values of y_via.

After adjusting W and L to optimize the center frequency of the PIFA at 30 GHz, the position of feeding will be considered for optimizing the impedance matching. This optimization is utilized by changing the value of y_via. The reflection coefficient simulated of the antenna with different values of the antenna's feeding positions (y_via) is presented in Figure 5. This observation shows that the impedance matching's antenna changes as the y-via value changes. In particular, when the value of y-via changed from 0.1 to 0.25 mm the antenna exhibits the best impedance matching as y_via is equal to 0.2 mm. The impedance of the rectangular patch antenna will be maximum at its edge and be zero at its center. Thus, the change in feeding leads to

https://doi.org/10.52111/qnjs.2023.17307

the change in antenna impedance. The optimal dimensions of the proposed single antenna at 28 GHz are presented in Table 2.

Table 2. Optimal dimensions of the single band PIFA (unit: mm).

Parameter	Value	Parameter	Value
W	1.6	L	1.1
W_g	1.8	L_g	1.3
W_{short}	0.05	H_{short}	0.598
x_via	0	y_via	0.2

The simulation result of S11 at the final single antenna are depicted in Figure 6. As can be observed, the final PIFA yields a center frequency of 28 GHz with -10 dB bandwidth spreading from 24.26 to 32.66 GHz. In particular, the proposed antenna exhibits a very good impedance matching of -51.8 dB.

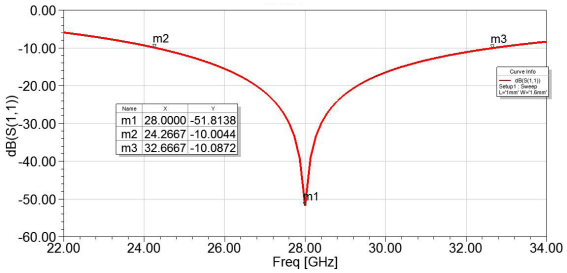

Figure 6. Simulated S11 of the final single antenna.

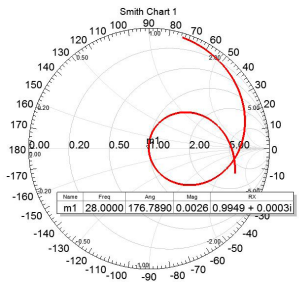

Figure 7. Simulated input impedance of the final antenna at 28 GHz.

To validate the impedance matching ability between 50 Ω feeder and the antenna, the impedance simulation is realized in the Smith chart, as shown in Figure 7. It can be seen at 28 GHz (the point of m1) that the antenna has a normalized input impedance of 0.9949 at the real part and approximately 0 at the imaginary part. The actual impedance of the antenna is approximately 50 Ω (0,9949×50). Thus, the above results demonstrated that the final antenna yields a perfect impedance matching.

The simulated radiation pattern of the final antenna at 28 GHz is exhibited in Figure 8. It is clear that the antenna exhibits a directional in the E-plane (Solid line) with a peak gain of 6.9 dBi.

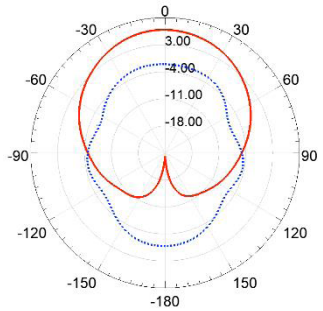

Figure 8. Simulated radiation pattern of the single antenna at 28 GHz.

The current distribution of the antenna at 28 GHz is shown in Figure 9. The current is almost focused on the edges of the rectangular patch.

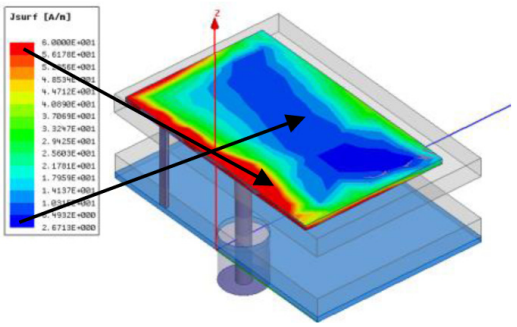

Figure 9. Current distribution on antenna surface at 28 GHz.

3. DUAL-BAND PIFA ANTENNA DESIGN

In this section, the dual-band PIFA was designed based on the proposed single one. A spiral slot is cut on the rectangular patch of the single antenna to produce the second resonant mode.

3.1. Antenna geometry

The dual-band PIFA antenna is built based on the design of the single-band antenna in Section 2 with a spiral etched slot on the surface of the patch. This method aims to create the second resonance at 38 GHz. The configuration of the dual-band PIFA is shown in Figure 10. The spiral slot consists of five straight slots and its total length is the sum of the length of five straight slots.

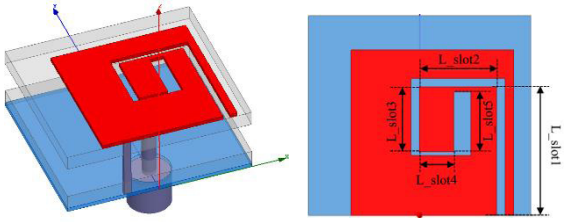

(a) (b)

Figure 10. Geometry of the proposed dual-band PIFA: (a) Perspective view, (b) Top view.

3.2. Theoretical calculation

The spiral slot length *(L_slot)* corresponding to the resonance of 38 GHz is calculated as follows[15]:

$$f = \frac{c}{4L\_slot\sqrt{\varepsilon_{eff}}} \quad (4)$$

$$L\_slot = \frac{c}{4f\sqrt{\varepsilon_{eff}}} = \frac{3.10^8}{4.38.10^9\sqrt{1{,}17}} = 1{,}82\ mm$$

Where,

$$L\_slot = L\_slot1 + L\_slot2 + L\_slot3 + L\_slot4 + L\_slot5$$

From the value of *L_slot*, the initial length of the straight slots was easily chosen: *L_slot*1 = 0,75 mm; *L_slot*2 = 0,45 mm; *L_slot*3 = 0,38 mm; *L_slot*4 = 0,2 mm, and *L_slot*2 = 0,1 mm.

3.3. Simulation and optimization

Figure 11 depicts the simulated reflection coefficient of the dual-band PIFA as its theoretical calculated dimensions. As can be observed from this figure, the PIFA antenna yields a dual-band performance with the lower frequency at 29.45 GHz and the higher frequency at 41.05 GHz. From these calculated frequencies, the dimensions of the initial dual-band PIFA was optimized to reach the final design of the dual-band antenna operated at the frequency of 28 and 38 GHz.

The dimensions of the dual-band antenna were justified to verify with the center frequencies of both bands. From that, the length and the width of the rectangular patch and the slot were investigated with different values. This method aims to find out the optimal values in which the PIFA antenna was operated at two center frequencies of 28 and 38 GHz.

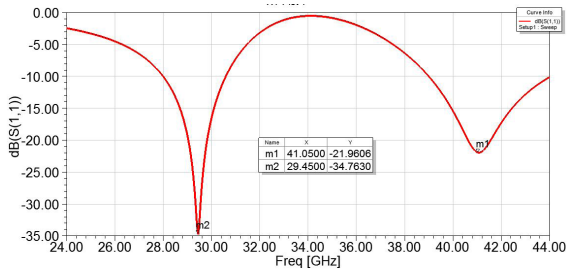

Figure 11. Simulated S11 of the dual-band PIFA as the theoretical calculation.

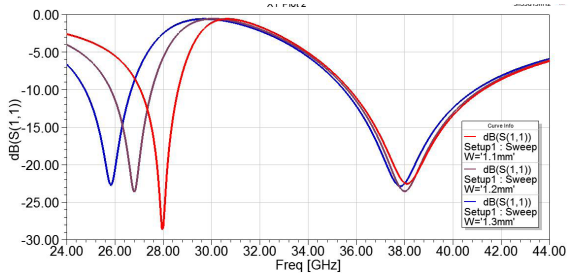

Figure 12. Simulated S11 of the dual-band antenna versus various values of W.

Figure 12 depicts the simulated S11 results with various values of the patch width while the other dimensions are fixed. As can be observed in Figure 12, increasing the patch width led to decreasing the lower frequency. Meanwhile, the higher one is not hardly change. It is noted that when the width *(W)* of rectangular patch increased, the total length of the antenna also increased. Therefore, the lower resonance was decreased since it is conversely proportional to the antenna's total length.

Return loss simulated versus various values of patch length *(L)* is shown in Figure 13. Two frequencies decreased as the patch length increased. This result is well consistent with the theory since the resonant frequency of the antenna is conversely proportional to its length.

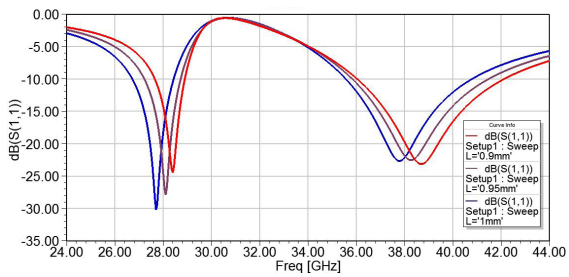

Figure 13. Simulated S11 versus different values of L.

https://doi.org/10.52111/qnjs.2023.17307

The length (L_slot5) and the width (H_slot5) of the fifth slot were used for optimizing the desired frequencies. Figure 14 shows the reflection coefficient simulated results of the dual-band antenna with different values of L_slot5. The width and the length of the patch are fixed at 1.1 mm and 0.95 mm, respectively. The simulated S11 of the antenna versus various values of H_slot5 is indicated in Figure 15. The value of L_slot5 was set at 0.35 mm, and the values of W and L were also fixed as mentioned in the simulation scenario in Figure 14. The simulated results presented in Figure 14 and 15 show that the two centre frequencies decrease while the two values decrease.

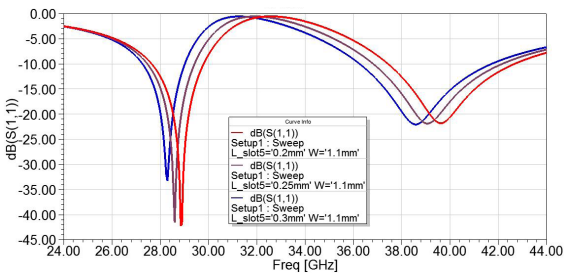

Figure 14. Simulated S11 of the antenna versus different values of L_slot5.

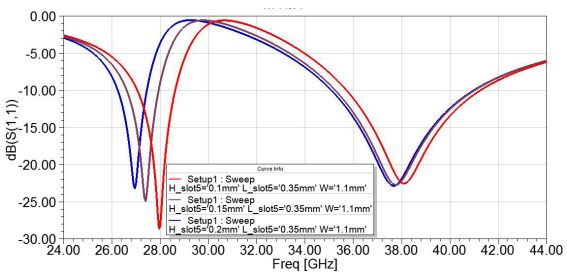

Figure 15. Simulated S11 of the antenna versus different values of H_slot5.

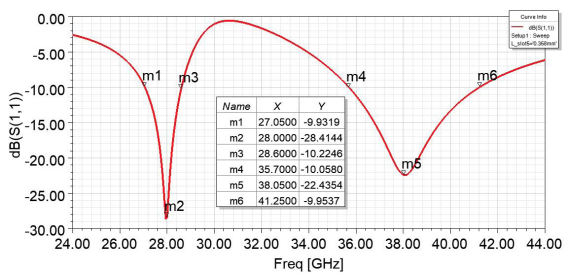

Figure 16. Simulated S11 of final dual-band PIFA at 28 GHz and 38 GHz.

Table 3. Optimal dimensions of the dual-band PIFA (unit: mm).

Parameter	Value	Parameter	Value
W	1,1	L_slot2	0,45
L	0,965	L_slot3	0,38
W_g	1,8	L_slot4	0,2
L_g	1,3	L_slot5	0,35
W_{short}	0,05	H_slot1	0,05
H_{short}	0,598	H_slot2	0,05
x_via	0	H_slot3	0,06
y_via	0,2	H_slot4	0,02
L_slot1	0,75	H_slot5	0,1

The simulated S11 of the dual-band antenna at the final design is exhibited in Figure 16. The final PIFA yields dual-band resonances operated at the centre frequencies of 28 and 38 GHz corresponding to the -10 dB bandwidth of 1.53 and 5.53 GHz. The optimal dimensions corresponding to the final design are illustrated in Table 3.

In order to verify the effect of the slot to the radiation of the proposed dual-band PIFA, the current distribution in the numerical simulation is shown in Figure 17. The current distribution at 28 and 38 GHz was different. The current distribution at 28 GHz concentrated at the outside edges of the slot whereas that at 38 GHz focused on the inside edges of the slot.

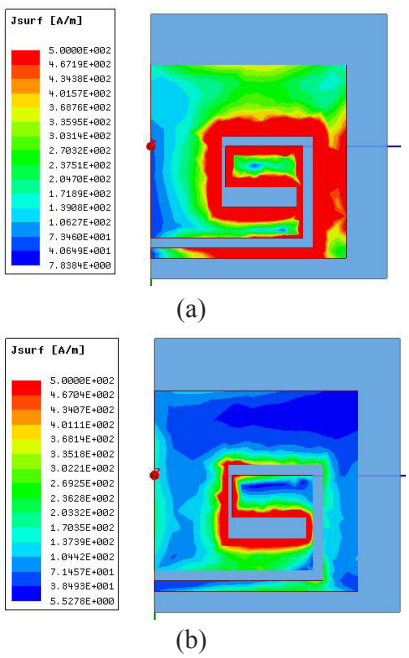

Figure 17. Current distribution on the dual-band PIFA antenna at: (a) 28 GHz, (b) 38 GHz.

Figure 18 shows the simulation result of the radiation pattern of the final dual-band antenna at 28 and 38 GHz. The solid curve is represented for E plane while the dash one is represented for H plane. From this figure, the antenna exhibits a directional pattern in xz plane with the realized gain at 28 GHz and 38 GHz is 6.81 dBi and 7.92 dBi, respectively.

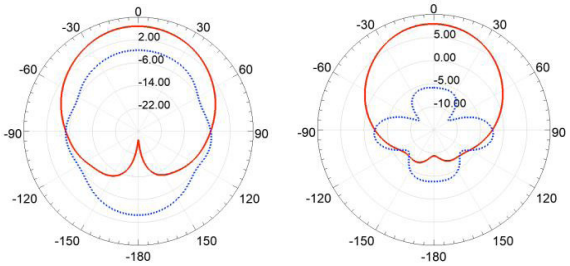

(a) (b)

Figure 18. Simulated radiation pattern of the final dual-band antenna at: 28 GHz, (b) 38 GHz.

Table 4 presents the comparison between the proposed PIFA and the other PIFA antennas reported in literature.[1,12,14] The proposed dual-band PIFA in this study exhibits good radiation characteristics in terms of -10 dB bandwidth and realized gain as well as the smallest form factor in comparison to the listed studies.

Table 4. Comparison between the proposed dual-band PIFA with the reported PIFA in literature.

Ref.	Overal size (mm×mm×mm)	Bandwidth (GHz)		Gain (dBi)	
		28 GHz	38 GHz	28 GHz	38 GHz
1	3×7×1.2	3.34	1.39	3.75	5.06
12	3.8×5.5×0.381	0.7	0.3	5	5.5
16	4×5.5×0.2	0.89	0.99	6.22	6.33
This work	1.3×1.8×0.598	1.53	5.53	6.81	7.92

4. CONCLUSION

A dual-band PIFA antenna for 5G communication systems has been designed, simulated and optimized in this study. The proposed PIFA consists of two dielectric layers and an air layer inserted between these two layers. Based on the PIFA antenna operated at 28 GHz, a spiral slot is etched on the patch radiator to create the second resonance at 38 GHz. Based on the initial results obtained by the theoretical calculation, the proposed PIFA antenna is optimized to achieve a dual-band resonances centred at the frequency of 28 GHz and 38 GHz. The antenna exhibits good performances with wide -10 dB bandwidth of 1.53 GHz and 5.53 GHz and the realized gain of 6.81 dBi and 7.92 dBi corresponding to 28 GHz and 38 GHz. The proposed antenna can be applied for 5G communication systems.

REFERENCES

1. W. Ahmad and W. T. Khan. Small form factor dual-band (28/38 GHz) PIFA antenna for 5G applications, Proceedings of the IEEE MTT-S International Conference on Microwaves for Intelligent Mobility (ICMIM), 2017.

2. C. Han, Y. Bi, S. Duan, and G. Lu. Rain rate retrieval test from 25-ghz, 28-ghz, and 38-ghz millimeter-wave link measurement in Beijing, *IEEE Journal of Selected Topics in Applied Earth Observations and Remote Sensing*, **2019**, *12*(8), 2835-2847.

3. H. M. Marzouk, I. A. Mohamed, and H. A. S. Abdel. Novel dual-band 28/38 GHz MIMO antennas for 5G mobile applications, *Progress In Electromagnetics Research C*, **2019**, *93*, 103-117.

4. N. Ashraf, O. Haraz, M. A. Ashraf, and S. Alshebeili. *28/38-GHz dual-band millimeter wave SIW array antenna with EBG structures for 5G applications,* Proceedings of the International Conference on Information and Communication Technology Research (ICTRC), 2015.

5. T. Deckmyn, M. Cauwe, D. V. Ginste, H. Rogier, and S. Agneessens. Dual-Band (28,38) GHz coupled quarter-mode substrate-integrated waveguide antenna array for next-generation wireless systems, *IEEE Transactions on Antennas and Propagation*, **2019**, *67*(4), 2405-2412.

6. P. Liu, X. Zhu, Y. Zhang, X. Wang, C. Yang, and Z. H. Jiang. Patch antenna loaded with paired shorting pins and h-shaped slot for 28/38 GHz

dual-band mimo applications, *IEEE Access*, **2020**, *8*, 23705-23712.

7. R. K. Meena, M. K. Dabhade, K. Srivastava, and B. K. Kanaujia. *Antenna design for fifth generation (5g) applications,* Proceedings of the 2019 URSI Asia-Pacific Radio Science Conference (AP-RASC), 2019.

8. W. Ahmad, A. Ali, and W. T. Khan. *Small form factor PIFA antenna design at 28 GHz for 5G applications,* Proceedings of the 2016 IEEE International Symposium on Antennas and Propagation (APSURSI), 2016.

9. F. N. M. Redzwan, M. T. Ali, M. M. Tan, and N. F. Miswadi. *Design of tri-band planar inverted F antenna (PIFA) with parasitic elements for UMTS2100, LTE and WiMAX mobile applications,* Proceedings of the 2015 International Conference on Computer, Communications, and Control Technology (I4CT), 2015.

10. M. K. Ishfaq, T. A. Rahman, H. T. Chattha and M. U. Rehman. Multiband split-ring resonator based planar inverted-F antenna for 5G applications, *International Journal of Antennas and Propagation,* **2017**, 5148083.

11. A. Iftikhar, M. N. Rafiq, M. M. Masud, B. Ijaz, S. Roy and B. D. Braaten. *A dual-band balanced planar inverted F antenna (PIFA) for mobile applications,* Proceedings of the 2013 IEEE Antennas and Propagation Society International Symposium (APSURSI), 2013.

12. M. Anouar and S. Larbi. *A new PIFA antenna for future mobile and wireless communication,* E3S Web of Conferences, **2022**, *351*, 01085.

13. S. M. A. Ali. An on-chip planar inverted-F antenna at 38 GHz for 5G communication applications, *International Journal of Antennas and Propagation,* **2022**, 1017816.

14. Y. A. Hashem, O. M. Haraz, and E. D. M. El-Sayed. *6-Element 28/38 GHz dual-band MIMO PIFA for future 5G cellular systems,* Proceedings of the 2016 IEEE International Symposium on Antennas and Propagation (APSURSI), 2016.

15. T. A. Milligan. Modern antenna design (2nd ed.), John Wiley & Sons Inc, New York, 2005.

16. M. E. Halaoui, L. Canale, A. Asselman, and G. Zissis. *Dual-Band 28/38 GHz Inverted-F Array Antenna for Fifth Generation Mobile Applications,* Multidisciplinary Digital Publishing Institute Proceedings, 2020.

TẠP CHÍ KHOA HỌC
TRƯỜNG ĐẠI HỌC QUY NHƠN
TẬP 17, SỐ 3, THÁNG 6 - 2023
ISSN: 1859-0357 E-ISSN: 2815-6242

MỤC LỤC